Thermal Evolution of the Ultrahigh-Temperature Metamorphic Rocks in the Archaean Napier Complex, East Antarctica

Tomokazu HOKADA

A Thesis submitted to The Graduate University for Advanced Studies
(Department of Polar Science, School of Mathematical and Physical Science)

for the Degree of Doctor of Philosophy (Science)

1999

CONTENTS

Abstract

The Napier Complex in Enderby Land, East Antarctica is composed of ultrahigh-temperature (UHT) metamorphic rocks. Geological survey was conducted in the Mt. Riiser-Larsen area and Tonagh Island, both of which are located on the high-grade portion of the complex, and the detailed petrological study on the UHT metamorphic rocks has been carried out.

Equilibrium temperatures of >1100°C for the thermal peak are estimated from re-integrated mineral compositions of perthitic, mesoperthitic and antiperthitic feldspars in orthopyroxene or garnet-bearing felsic gneisses, garnet-sillimanite gneiss, garnet-orthopyroxene-bearing quartzo-feldspathic or siliceous gneisses, sapphirine-bearing aluminous gneisses from Mt. Riiser-Larsen area and sapphirine-bearing aluminous gneisses from Tonagh Island.

Mineral parageneses involving sapphirine, orthopyroxene, garnet, osumilite and quartz and the reaction textures after sapphirine + quartz are investigated by means of the phase relations. Mineral parageneses of sapphirine + orthopyroxene + quartz, sapphirine + garnet + quartz and garnet + osumilite, and the reaction textures of cordierite and/or garnet formed after sapphirine + quartz constrain the pressure conditions at thermal peak of 0.6~0.8 GPa (>1040°C) for the central area of the Mt. Riiser-Larsen. Mineral parageneses involving sapphirine + orthopyroxene + quartz and osumilite, and the reaction textures of orthopyroxene + sillimanite formed after sapphirine + quartz indicate the pressure conditions at thermal peak of 0.8~0.9 GPa (>1030°C) for the western area of the Mt. Riiser-Larsen. These two areas within Mt. Riiser-Larsen, representing different structural level at the peak metamorphism, are divided by a shear zone composed of mylonite and pseudotachylite dipping nearly vertically. Thus, the two aeas are considered to have been juxtaposed due to the movement of the shear zone. The westward increase in of pressure estimated here is oblique to the proposed regional pressure gradient of increasing southward within the Napier Complex, but is not inconsistent with the proposed uplift process of south-west part of the Napier Complex in relation to the transpressional tectonic event of the Proterozoic Rayner Complex.

Garnet-orthopyroxene geobarometry for sapphirine-bearing aluminous gneisses from northern part of Tonagh Island yields 0.8~1.1 GPa for pressure conditions at the thermal peak, suggeesting that the present exposed level of the northern part of Tonagh Island is similar or possibly deeper structural level than that of the Mt. Riiser-Larsen area.

These P-T estimates suggest a coherent crustal sequence of mid to lower continental crust, about 20 ~ 35 km depth, has been heated to >1100°C. The areal extent of 1100°C should be at least 50 x 10 km, involving Mt. Riiser-Larsen and Tonagh Island, and maximum 200 x 50 km which is deduced from the areal distribution of sapphirine+quartz. To assess the possible heat source for the UHT metamorphism up to 1100°C, thermal modeling using a finite difference method is applied to the models of crustal thickening, intrusion of magma and removal (delamination or detachment) of lithospheric thermal boundary layer. As the results, the UHT conditions cannot be achieved solely by usual crustal thickening process, and intrusion of high temperature magma or possibly heating from hot asthenospheric mantle accompanied by the removal of the lithospheric thermal boundary layer could be the heat source of the UHT metamorphism. In addition to the heat source, dehydration process prior to the heating to UHT conditions is considered to be an essential factor for the UHT metamorphism to achieve such extremely high temperature conditions without complete melting of quartzo-feldspathic rocks.

Electron microprobe analyses of U, Th and Pb contents in monazite and zircon together with their petrographical observation support an interpretation that the UHT metamorphism of the Napier Complex occurred at 2.5 Ga rather than ~2.8 Ga which is previously proposed. 2.9-2.8 Ga obtained by SHRIMP and other methods may be the age of the tectonic process to dehydrate the precursors of the UHT gneisses or that of the formation of the protolith.

Chapter 1 Introduction

1.1. On ultrahigh-temperature metamorphism

As the advance of metamorphic petrological study, the recognition of pressure and temperature limits of metamorphism has been drastically changed, and has recently been expanded to both higher-pressures and temperatures than ever. The higher-pressures one is characterized by the discovery of metamorphic coesite and of metamorphic diamond, and has been classified as ultrahigh-pressure (UHP) metamorphism, which is considered to be formed by subduction of crustal material followed by the thickening of continental crust at continental collision zone (e.g., Coleman and Wang, 1995). On the other hand, the higher-temperatures one is recognized as ultrahigh-temperature (UHT) metamorphism (e.g., Spear, 1993; Harley, 1998), which is characterized by the key indicators described below. However, its heat source and evolution process are not always understood. The Napier Complex, where is known as a UHT metamorphic terrane, is the best field to reveal such issues.

Harley (1998) summarizes the occurrence and characterization of UHT metamorphism as follows. (1) *Definition of UHT metamorphism*: It can be considered as a subdivision of the granulite facies, and is defined as crustal metamorphism that has occurred at peak conditions of greater than 900°C and at mid- to deep-crustal levels. The effective field involves temperatures of 900-1100°C and pressures in the range of 0.7-1.3 GPa. (2) *Occurrence and distribution*: The Napier Complex of Antarctica, Wilson Lake in Labrador, the Eastern Ghats of India, the In Ouzzal Complex of Algeria, the Labwor Hills of Uganda and the Sutam Block of the Aldan Shield in Siberia are the regional UHT terranes. A greater number of relatively isolated UHT localities are also known (Table 1.1). (3) *Key indicators*: Petrogenetic grids involving mineral equilibria in the FeO-MgO-Al_2O_3-SiO_2 (FMAS) and the K_2O-FeO-MgO-Al_2O_3-SiO_2-H_2O (KFMASH) systems indicate that sapphirine+quartz, orthopyroxene+sillimanite+quartz and osumilite-bearing parageneses are restricted to high-temperature conditions. In addition, high-Al orthopyroxene, inverted metamorphic pigeonite and high-Ca scapolite+wollastonite-bearing paragenesis can be UHT indicators. (4) *P-T paths*: The post-peak P-T paths of UHT terranes are classified into isobaric cooling (IBC) and isothermal decompression (ITD), and their combinations. The Napier Complex is the best example for the former, and the latter is inferred for the In Ouzzal terrane.

Locality/Area		P-T trajectory
Regional UHT terranes		
Napier Complex	Antarctica	IBC
Labwor Hills	Uganda	IBC
Wilson Lake	Canda	IBC
Eastern Ghats (north)	India	IBC&ITD
Eastern Ghats (south)	India	ITD
In Ouzzal	Algeria	ITD
Aldan Shield	Siberia	ITD
Relatively isolated UHT localities		
Sipiwesk Lake	Canda	IBC
Lace Xenoliths	South Africa	IBC
Rayner Complex (Forefinger Point, Long Point)	Antarctica	ITD
Lützow-Holm Complex (Rundvagshetta)	Antarctica	ITD
St. Maurice	Canada	ITD
Sri Lanka (Munwatte, Hakurutale)	Sri Lanka	ITD
Gruf Complex	Alps	ITD
Limpopo Belt	South Africa	ITD
Anabar Massif	Siberia	ITD
Bamble	Norway	ITD
*Lewisian Complex	Scotland	*

Table 1.1 Localities or areas that have experienced UHT metamorphism summarized by Harley (1998). See references therein in detail. IBC: isobaric cooling, ITD: isothermal decompression. *Lewisian Complex is from Baba (1998).

Harley (1998) also implies that convective thinning or detachment of lithospheric thermal boundary layer during or after crustal thickening may play a major role in the formation of UHT metamorphic belts and hence the evolution of the deep continental crust. However, the general process of the formation and evolution of UHT terranes has not been elucidated yet, and further petrological and experimental data are needed.

1.2. Previous work on the Napier Complex (Historical review)

According to Sheraton *et al.* (1987), the first report of the rocks in the Napier Complex was made by Tilley in 1937 based on the geological survey at Proclamation Island located on the northernmost part of the complex, where Mawson's British, Australian and New Zealand Antarctic Research Expedition (BANZARE) landed in 1930. During the 1950s and 1960s, geologists of Australian National Antarctic Research Expeditions (ANARE) visited several localities throughout Enderby Land including the Napier Complex, and Dallwitz (1968) reported the first known occurrence of coexisting sapphirine and quartz, which indicates exceptionally high metamorphic temperatures, from Dallwitz Nunatak. In 1960s, geologists of Soviet Antarctic Expedition (SAE) undertook 1:1000000-scale mapping of Enderby Land, and distinguished two metamorphic complexes, the Napier Complex and the Rayner Complex. They interpreted that both complexes were of Archaean age and that the Napier Complex is older and slightly higher-grade than the Rayner Complex (Ravich and Kamenev, 1975).

Geologists of ANARE performed systematic geological survey of Enderby Land from 1974 to 1980, and the studies of the Napier Complex including geochemistry, geochronology, geophysics, metamorphic petrology and structural geology were rapidly advanced, and are summarized in Sheraton *et al.* (1987). Base on these studies, distinction of the Napier Complex and the Rayner Complex is retained with some modifications; the occurrence of unmetamorphosed dolerite dykes at 1.2 Ga restricts the Napier Complex as an Archaean terrane, whereas the Rayner Complex with metamorphosed 1.2 Ga dolerite dykes is a Proterozoic terrane. Based on metamorphic and structural studies, they indicate three major tectonic events, D1~D2 of UHT conditions and D3 of granulites ~ lower amphibolite facies. Combined with the recent geochronological works, initial felsic igneous activities forming the protolith of the complex started at 3.8 Ga and D1~D2 is interpreted to have occurred at 3.0 ~ 2.8 Ga and D3 at 2.5 Ga (Harley and Black, 1997).

Age (Ga)	Event (Harley and Black, 1997)	Age (Ga)	Event (alternative interpretation)
3.8-	Crystallization of igneous precursors (Tula Mts.)		
	Deposition of supracrustal		
3.0	Crystallization of charnockite (Proclamation Island)		
	D1 deformation and metamorphism		
	Granulite facies metamorphism (Napier Mts. and other areas)		
2.9-2.8	**UHT metamorphism (D1-D2)** (Tula and Scott Mts.)	3.0-2.8	? igneous activity or metamorphism
	Emplacement of granitoids (Napier Mts.)		
	Near isobaric cooling		
2.5-2.4	Lower-granulite ~ upper-amphibolite facies metamorphism (D3)	2.5	**UHT metamorphism** (Grew and Manton, 1979; De Paolo *et al.*, 1982; Asami *et al* ., 1997)
	(1.00-0.95 Ga: Metamorphism of the Rayner Complex)		
	(0.55-0.52 Ga: Metamorphism of the Lützow-Holm Complex)		

Table 1.2 Summary and comparison of the proposed history of the Napier Complex.

Since 1982, geologists of Japanese Antarctic Research Expedition (JARE) visited several outcrops of the Napier Complex, and reported some geological and petrological aspects (Motoyoshi and Matsueda, 1984; Makimoto *et al.*, 1989; Motoyoshi and Hensen, 1989; Motoyoshi *et al.*, 1990; Hensen and Motoyoshi, 1992; Ishizuka *et al.*, 1998). Geochronological works have been also conducted (Owada *et al.*, 1994; Tainosho *et al.*, 1994; Tainosho *et al.*, 1997; Shiraishi *et al.*, 1997; Asami *et al.*, 1998; Takigami *et al.*, 1998), and suggest 2.5 Ga for the timing of UHT metamorphism, which is contrary to the above interpretation, i.e., ~2.8 Ga for the UHT conditions.

There is no direct evidence for the tectonic process and the heat source of the UHT metamorphism in the Napier Complex. Anorthosite intrusion, which is occasionally present in the complex, is proposed for the heat source of the UHT metamorphism (Sheraton *et al.*, 1980; Grew, 1980). In contrast, it is interpreted that the Napier Complex is the lower plate of doubly thickened crust after the analogy of common granulite terranes (Ellis, 1987; Harley, 1989; Harley, 1991). Motoyoshi and Hensen (1989) and Hensen and Motoyoshi (1992) discussed polymetamorphic events with compressional counterclockwise P-T path based on the textural evidence, and proposed a regional scale intrusion of pluton above the present level of exposure of the complex for the heat source of the second event.

1.3. Statement of problem

The Antarctic Continent is isolated from the other continents and, hence, a limited number of geological survey has been conducted. A few geological outline or structural map of the outcrops in the Napier Complex has been published, i.e., Fyfe Hills, McIntyre island, Zircon Point (Sandiford and Wilson, 1986), Mt. Sones (Harley, 1986), Eastern Tonagh Island (Harley, 1987), Fields Islands, Beaver Island, Bowl Island, northeast face of Mt. Mclennan (Sheraton *et al.*, 1987). One of the main purposes of the geological survey performed by JARE geologists including the author is to provide detailed outcrop-scale geological map of the Napier Complex. For this purpose, the detailed geological survey of the Mt. Riiser-Larsen area, the largest outcrop in the complex, and of Tonagh Island, where the well-layered sequences of ultrahigh-temperature gneisses are exposed. Based on our survey, detailed geological map of these two areas are published (Ishizuka *et al.*, 1998; Osanai *et al.*, 1999).

Ultrahigh-temperature metamorphism in the Napier Complex is characterized by the occurrence of the mineral parageneses including sapphirine + quartz (Dallwitz, 1968; Ellis *et al.*, 1980; Grew, 1980; 1982; Motoyoshi and Matsueda, 1984; Motoyoshi and Hensen, 1989), spinel + quartz (Motoyoshi *et al.*, 1990), osumilite (Ellis *et al.*, 1980; Grew, 1982; Motoyoshi and Matsueda, 1984; Hensen and Motoyoshi, 1992), and inverted metamorphic pigeonite (Sandiford and Powell, 1986; 1988; Harley, 1987). However, the occurrence of sapphirine, either coexisting with quartz or not, is restricted to magnesian or aluminous rocks, and is not common in the Napier Complex. Several papers reported the occurrence of sapphirine-bearing gneisses from the Napier Complex, which include the petrological study with textural and electron microprobe analysis (Ellis *et al.*, 1980; Grew, 1980; 1982; Motoyoshi and Matsueda, 1984; Harley, 1985; 1986; Sheraton *et al.*, 1987; Motoyoshi and Hensen, 1989; Hensen and Motoyoshi, 1992) and the description of the mineral assemblages only (Dallwitz, 1968; Sheraton *et al.*, 1980; Sandiford, 1985; Makimoto *et al.*, 1989; Ishizuka *et al.*, 1998). The protolith of these sapphirine-bearing gneisses are generally regarded as pelitic precursor, but little description was made to the field occurrences of these distinctive rocks, especially to the geological relationship to the surrounding rocks. The modes of occurrences and petrography of sapphirine, spinel and osumilite from the Mt. Riiser-Larsen area and those from Tonagh Island are described in Chapters 3 and 4.

As mentioned in the previous section, thermal history of the Napier Complex have been proposed (Sheraton *et al.*, 1987; Harley and Hensen, 1990; Harley and Black, 1997, and are summarized in Table 1.2). However, the heat source or the tectonic process to achieve the ultrahigh-temperature conditions, which is the fundamental problem for the thermal evolution of the Napier Complex, is still in dispute. It can be confirmed or constrained by

1) precise P-T estimations of the thermal climax,
2) thermal and baric gradients within the Napier Complex,
3) P-T path of the prograde and the retrograde metamorphism.

1) P-T conditions of the thermal climax is precisely re-investigated in this thesis based on phase relations (Chapter 3), garnet-orthopyroxene equilibria (Chapter 4) and chemical compositions of feldspar (Chapter 5). 2) Field thermal and baric gradients are also discussed in these chapters. 3) Prograde P-T path is important and is directly related with the tectonic process. Both clockwise and counterclockwise P-T paths have been proposed for the

prograde history of the Napier Complex, and are still in argument. This thesis could not present the direct evidence for the prograde process. However, if a quartzo-feldspathic rock contains significant amount of H_2O, it will be completely molten to generate magma before reaching to the UHT conditions. Therefore, dehydration prior to the UHT metamorphism is required as an additional constraint for the pre-peak evolution of the complex. In this context, significance of the quartzo-feldspathic rocks without hydrous minerals is noted. Few processes can generate the almost anhydrous quartzo-feldspathic rocks observed in the Napier Complex, i.e., 1) dehydration melting with complete melt segregation, 2) dehydration without partial melting at low-pressure condition (pyroxene-hornfels facies metamorphism) or 3) dehydration accompanied by influx of CO_2-rich fluid (charnockitization). Dehydration melting should be most common process for decomposition of hydrous phases. However, this process hardly generates anhydrous quartzo-feldspathic rock but generally separates the rock into hydrous quartzo-feldspathic melt and anhydrous relatively mafic or aluminous restite. The process to dehydrate the gneisses from the Napier Complex will be discussed in Chapter 7.

The age of the ultrahigh-temperature metamorphism in the Napier Complex is in argument. A wide variety of ages, 3.8 Ga ~ 1.2 Ga, are obtained from the rocks in the Napier Complex. 2.8-2.9 Ga and 2.4-2.5 Ga are widespread and either of them are considered to be the age of the ultrahigh-temperature metamorphism. This thesis estimates monazite and zircon ages based on the electron microprobe analyses of U, Th and Pb in monazite and zircon in situ of the thin section (CHIME method), and discusses the timing of the UHT metamorphism (Chapter 6).

Based on the results of the preceding chapters and of the previous studies, heat source and tectonic model proposed for UHT metamorphism of the Napier Complex, i.e., heating accompanied by (a) crustal thickening, (2) intrusion of plutonic rocks, or (3) detachment of lithospheric thermal boundary layer, are assessed by the thermal modeling using finite difference method in Chapter 7. And in conclusion, the possible process for the thermal evolution of the Napier Complex is proposed.

Chapter 2 Geology

2.1. Regional geology

East Antarctic shield is mostly covered by an ice sheet. Basement rocks occur as mountains or small peaks individually isolated in the ice sheet or as islands separated by sea, and are exposed within 200 km from the coast. Enderby Land is the coastal area between longitudes 45°E and 55°E in East Antarctica, and it is bounded to the east by Kemp Land and to the west by Dronning Maud Land. The Archaean Napier Complex (NC) and the Proterozoic Rayner Complex (RC) constitute the Enderby Land and the western Kemp Land, and the NC is bounded its southern margin by the RC (Fig. 2.1). To the west of RC, Early Palaeozoic Lützow-Holm Complex is distributed. The Napier Complex consists of high-temperature granulite facies metamorphic rocks, and is characterized by the major metamorphic ages of older than 2.5 Ga and the presence of unmetamorphosed 1.2 Ga dolerite dykes. On the other hand, the Rayner complex is composed of upper amphibolite to granulite facies metamorphic rocks. It is considered to have suffered main metamorphism at 1.0 Ga and the dolerite dykes also metamorphosed at the same age (Sheraton *et al.*, 1987). A part of the Rayner Complex is considered to be reworked area of the Napier Complex. The Lützow-Holm Complex experienced amphibolite to granulite facies metamorphism at 520-540 Ma (Shiraishi *et al.*, 1994).

2.2. Geology of the Napier Complex

The Napier Complex is distributed 400 km x 200 km in the coastal area from longitude 46°E to 57°E and from latitude 66°S to 68°S in East Antarctica, and is mostly covered by an ice sheet. It is composed of granulite facies with partly UHT conditions metamorphic rocks, which is characterized by almost anhydrous and high temperature mineral assemblages. A scarce extent of unmetamorphosed discordant or subconcordant granitic intrusions, dolerite dykes and pegmatites is also present. Pseudotachylite- and mylonite-bearing shear zones are locally developed.

According to Sheraton *et al.* (1987), orthopyroxene-quartz-feldspar (felsic) gneiss with minor mafic granulite is predominant over much of the complex. It is interpreted as igneous precursor, and is classified into two, granitic

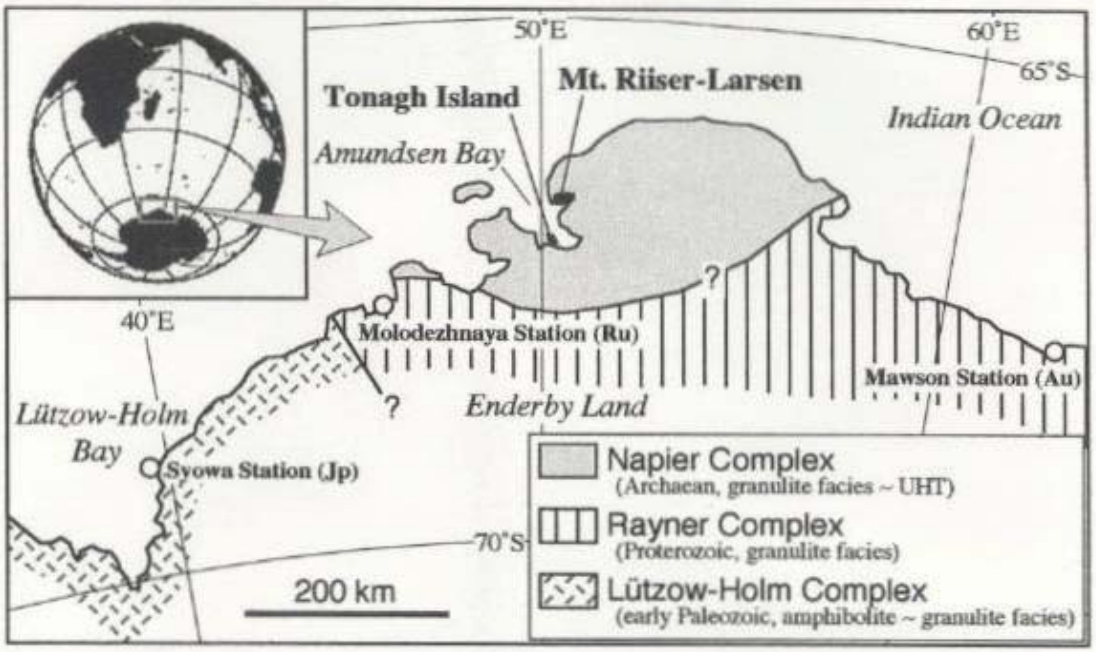

Fig. 2.1 Geological outline of Enderby Land, East Antarctica, and neighboring area. The estimated boundary between the Napier Complex and the Rayner Complex is after Sheraton *et al.* (1987).

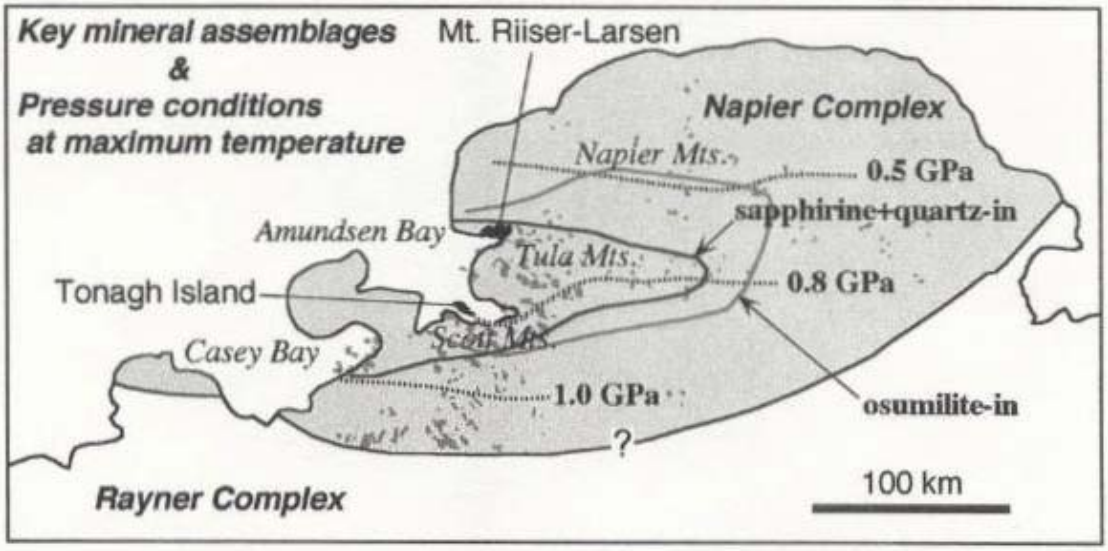

Fig. 2.2 Distributions of outcrops in the Napier Complex. Isograds of 'sapphirine+quartz-in' and 'osumilite-in' and pressure conditions at maximum temperature of the Napier Complex are after Harley and Hensen (1990).

(charnockitic) one composed of mesoperthite and tonalitic (enderbitic) one with plagioclase. Layered garnet-quartz-feldspar (felsic) gneiss with subordinate pelitic, psammitic and ferruginous (magnetite-quartz) metasediments is particularly abundant in the northern Scott, Tula, and western Napier Mountains. It is considered to be derived from both sedimentary (arkose or greywacke) and igneous origins. Aluminous pelitic and psammitic metasediments are also interlayered with garnet-quartz-feldspar gneiss, and contain sapphirine, spinel and osumilite-bearing mineral assemblages.

The deficient amount of exposed outcrops due to covered by ice sheet and, hence, the lack of mutual relationship among outcrops makes it difficult to reconstruct the comprehensive geological outline of the complex. However, field thermal and baric gradients inside of the Napier Complex are suggested by the occurrence of key minerals, i.e., sapphirine + quartz, orthopyroxene + sillimanite + quartz, osumilite and cordierite, and by geothermobarometries (Fig. 2.2). The highest-grade region of the Napier Complex is considered to be areas including Amundsen Bay - northern Scott Mountains - Casey Bay area and the baric gradient is oblique to the thermal one that pressure condition increases monotonously southward (Harley and Hensen, 1990).

Sheraton *et al.* (1987) also summarized the major deformation stages of the Napier Complex from D1 to D3 and the localized deformation stage including the intrusion of pegmatites from D4 to D5. D1 is the earliest recognizable deformation stage and is responsible for the main foliation parallel to the compositional layering including isoclinal and intrafolial fold and is considered to be synchronous with the peak metamorphism. D2 is characterized by tight to isoclinal and asymmetric fold of amplitudes up to several hundred meters and is still granulite facies conditions. Both D1 and D2 are considered to be formed in response to a single prolonged period of deformation. The regional strike in most of the Napier Complex is largely the result of D3, which is considered to occurred during waning stages of the high-grade metamorphism. D4 and D5 are characterized by relatively narrow shear zones and by sub-vertical mylonite zones locally with pseudotachylite veins, respectively. Dolerite dykes (Amundsen Dykes) of 1.2 Ga cut the D1 ~ D3 structures, but not D4 and D5, suggesting D1 ~ D3 before 1.2 Ga and D4 ~ D5 after 1.2 Ga. D4 is considered to be related to the metamorphism of the Rayner Complex at 1.0 Ga.

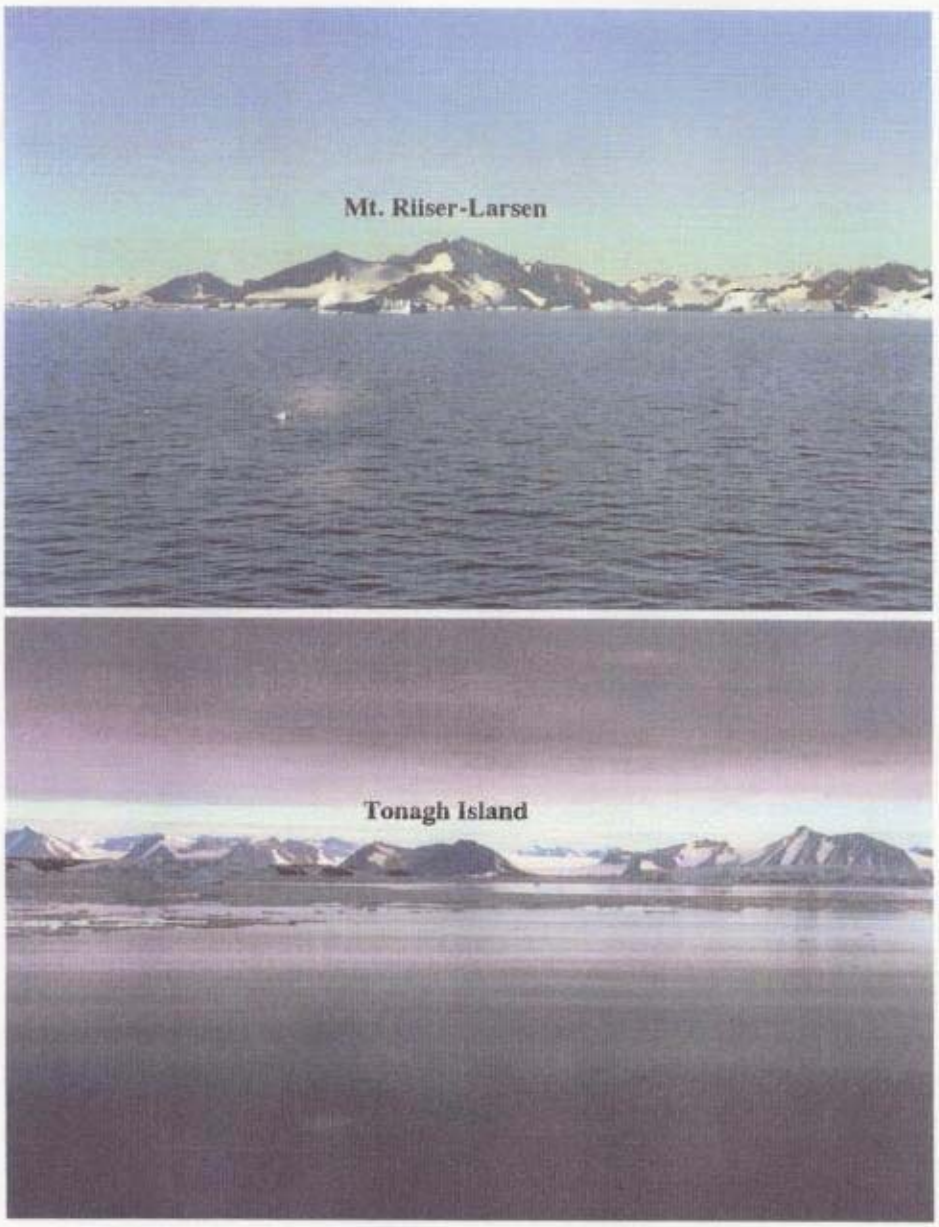

Fig. 2.3 Far-distance view of the Napier Complex involving the study areas. (a) Mt. Riiser-Larsen. View from southwest. (b) Tonagh Island. View from north.

2.2.1. Mt. Riiser-Larsen area

The Mt. Riiser-Larsen area is the largest outcrop in the Napier Complex covering approximately 13 x 6 km in extent (Fig. 2.2). It is situated on the northern margin of Amundsen Bay which represents the high-grade region of the complex. Several geological surveys have been performed in the Mt. Riiser-Larsen area (Motoyoshi and Matsueda, 1984; Makimoto *et al.*, 1989; Ishizuka *et al.*, 1998). It consists mainly of orthopyroxene felsic gneiss, garnet felsic gneiss, garnet gneiss and mafic granulite with minor amount of garnet-sillimanite gneiss, magnetite-quartz gneiss, aluminous gneiss, siliceous gneiss, quartzo-feldspathic gneiss containing sapphirine and osumilite and ultramafic rocks (Figs. 2.4 and 2.5). They contain little hydrous minerals such as biotite and amphibole, excluding retrograde products. Unmetamorphosed dolerite dyke cut the gneisses throughout the area. Pseudotachylite-mylonite zone of ca. 200 m wide, which runs along the west of Richardson Lake, divides the area into two, the central and the western areas. It has north-south strike and almost vertical dip, and subvertical lineation is observed in some portions. Detailed geological outline of the Mt. Riiser-Larsen area is described in Ishizuka *et al.* (1998).

In the central area, lithological boundaries are generally striking east-west to northeast-southwest and dipping south to southeast. Orthopyroxene felsic gneiss, garnet felsic gneiss, two-pyroxene mafic granulite and garnet gneiss are the main constituents in the central area, and they show well-layered structures of several 10 centimeters to over 10 m thick of each layer. The upper structural level is dominated by relatively massive and thick orthopyroxene felsic gneiss layer of over 100 m thick.

In the western area, dip and strike are not monotonous. Northeast-southwest strike with southeast dip is dominant in the northern part, whereas northwest-southeast to northeast-southwest strike with north dip is distinguished in the southern part of the area. Rock types are similar to those in the central area. However, thick and massive orthopyroxene felsic gneiss does not occur in the area.

Felsic gneisses are the most voluminous component in whole of the studied area and are composed of quartz, feldspar (mesoperthite or plagioclase), orthopyroxene or garnet with accessory rutile, ilmenite, apatite, monazite and zircon. They are relatively massive or weakly foliated, but sometimes elongated quartz crystals are aligned in parallel. Massive mafic granulite layers are intercalated with felsic gneisses. It is composed of orthopyroxene, clinopyroxene, plagioclase and minor quartz. Garnet gneiss is also one of the

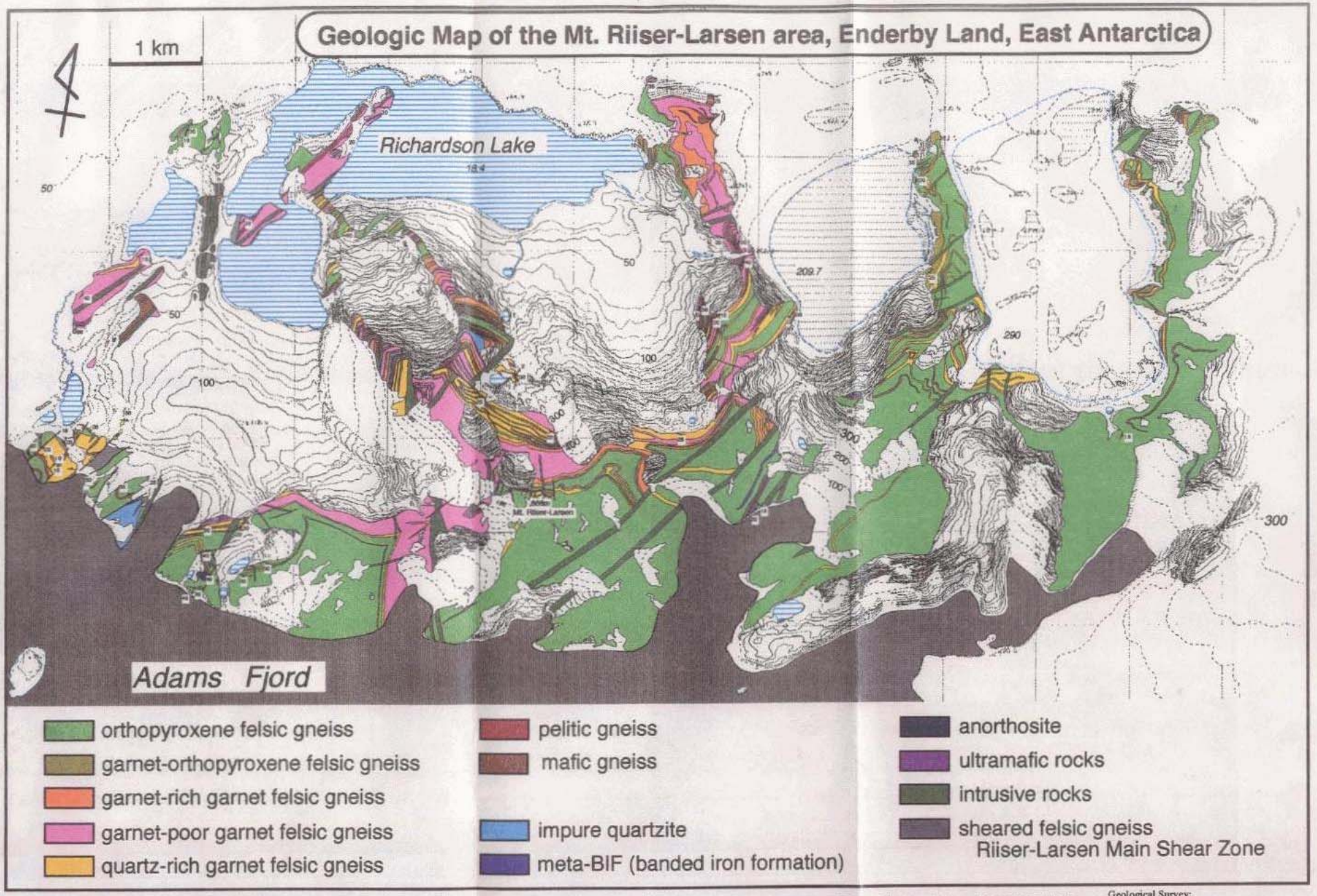

Fig. 2.4 Geological map of the Mt. Riiser-Larsen area, which was already published as Ishizuka *et al*. (1998).

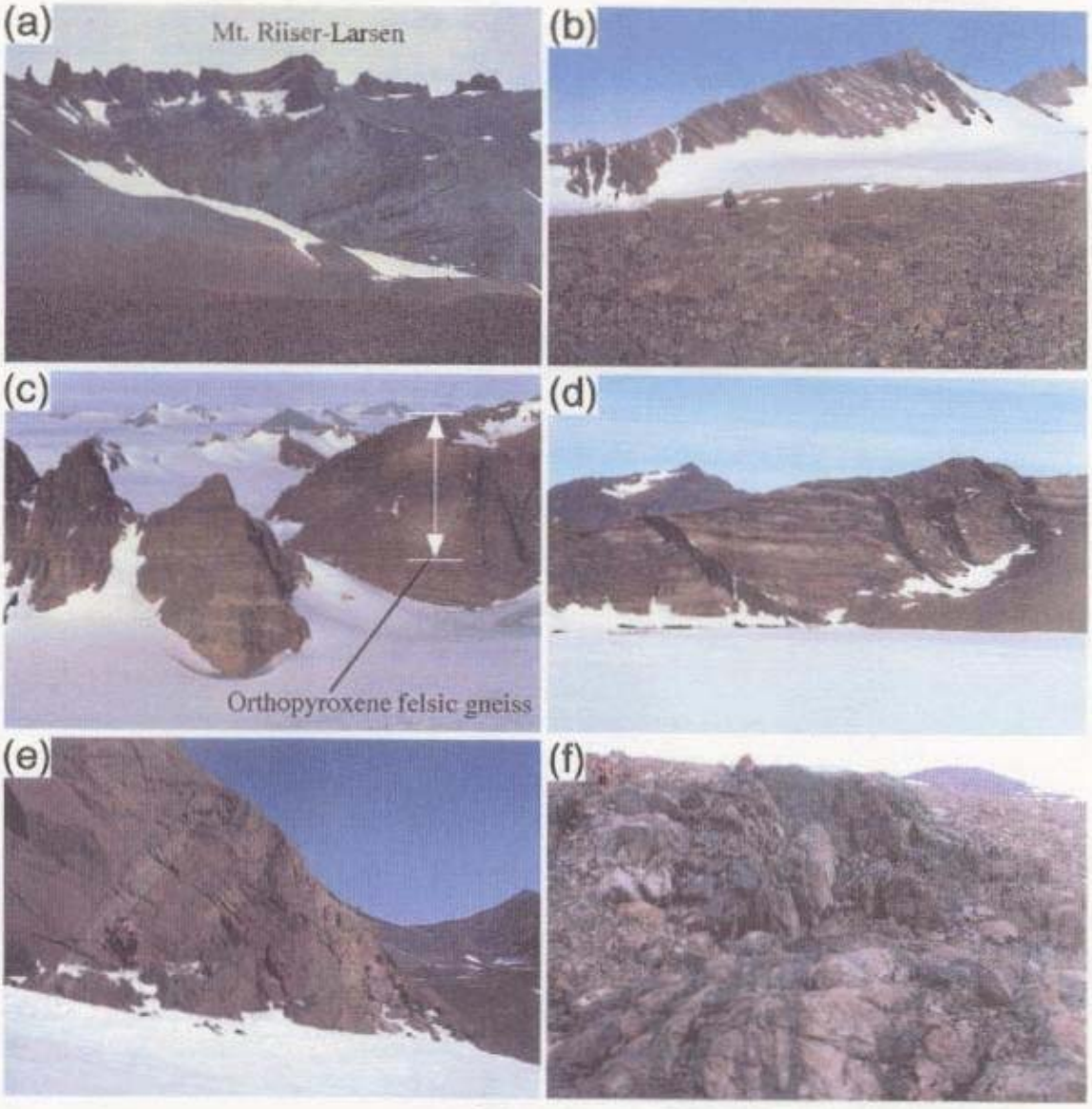

Fig. 2.5 (a) Mt. Riiser-Larsen (the highest peak) viewed from the northeast. A ridge with brown color is composed of orthopyroxene felsic gneiss. (b) Well-layered structure composed mainly of garnet felsic gneiss (white~gray), orthopyroxene felsic gneiss (pale brown), garnet gneiss (orange) and mafic granulite (dark brown). Amundsen dyke (dolerite) intrudes into the gneisses. (c) Thick and massive orthopyroxene felsic gneiss (upper half) and well-layered sequences composed mainly of orthopyroxene felsic gneiss (lower half). (d) Amundsen dyke (black) cut the alternation mainly composed of orthopyroxene felsic gneiss. (e) Layered sequences mainly composed of garnet felsic gneiss. (f) Riiser-Larsen Main Shera Zone, composed of mylonite and pseudotachilite, deviding the area into the central and the western parts.

major constituent rock types in the area, and have the same mineral assemblage as garnet felsic gneiss, i.e., quartz + mesoperthite + garnet. Modal proportion of garnet in garnet gneiss is much larger than that in garnet felsic gneiss. Garnet gneiss is commonly accompanied with garnet-sillimanite gneiss which is comparable with pelitic metasediment, suggesting the garnet gneiss as psammitic metasediment. Other than the above, a variety of rock types are present as block, thin layer or lens as follows: magnetite-pyroxene-quartz gneiss, spinel- and/or sapphirine-bearing impure quartzite, garnet-orthopyroxene gneiss, sapphirine- and/or osumilite-bearing quartzo-feldspathic or aluminous gneisses, and ultramafic rocks including peridotites and pyroxenites.

2.2.2. *Tonagh Island*

Tonagh Island is also located in the Amundsen Bay region, the high-grade part of the Napier Complex (Fig. 2.2). Mylonite and pseudotachylite-bearing shear zones divide the island into five units (Figs. 2.6 and 2.7). The central (Units II and III) and the southern (Units IV and V) parts of the island are composed mainly of the alternation (several meters order) of orthopyroxene felsic gneiss and mafic granulite, and that of orthopyroxene felsic gneiss and garnet felsic gneiss, respectively. Whereas in the northernmost part (Unit I), centimeter to meter order alternation of orthopyroxene felsic gneiss, garnet felsic gneiss, two-pyroxene mafic granulite, garnet gneiss, garnet-sillimanite gneiss, sapphirine-bearing aluminous gneisses, magnetite-quartz gneiss, pyroxenite and ultramafic rock is observed. Foliation defined by lithological boundary are E-W ~ NE-SW strike and steeply N or S dip with forming small-scale synform and antiform in the Unit I, and gently north dip in the Units II ~ V. Detailed geological outline of Tonagh Island is described in Osanai *et al.* (1999). The aluminous gneisses occur as a block or a pod in felsic (or quartzo-feldspathic) gneisses or mafic granulite, or as a thin layer around ultramafic rocks.

Geological Map of Tonagh Island in the Napier Complex, East Antarctica

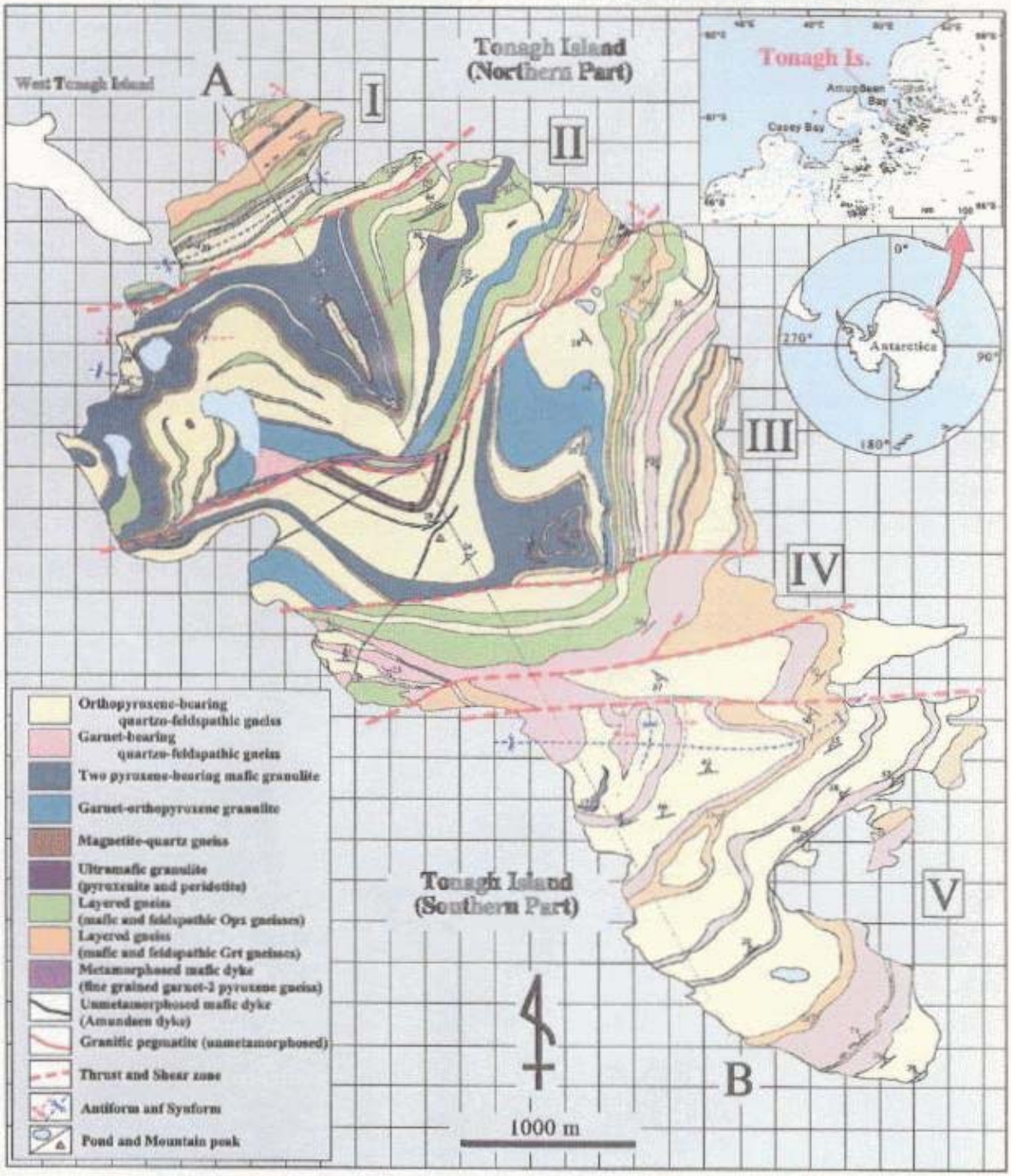

Produced by JARE-39

Geological Survey:
Y. Osanai (Okayama Univ.)
T. Toyoshima (Niigata Univ.)
M. Owada (Yamaguchi Univ.)
T. Tsunogae (Shimane Univ.)
T. Hokada (Grad. Univ. Advanced Studies)
W.A. Crowe (Univ. Western Australia)

Fig. 2.6(a)

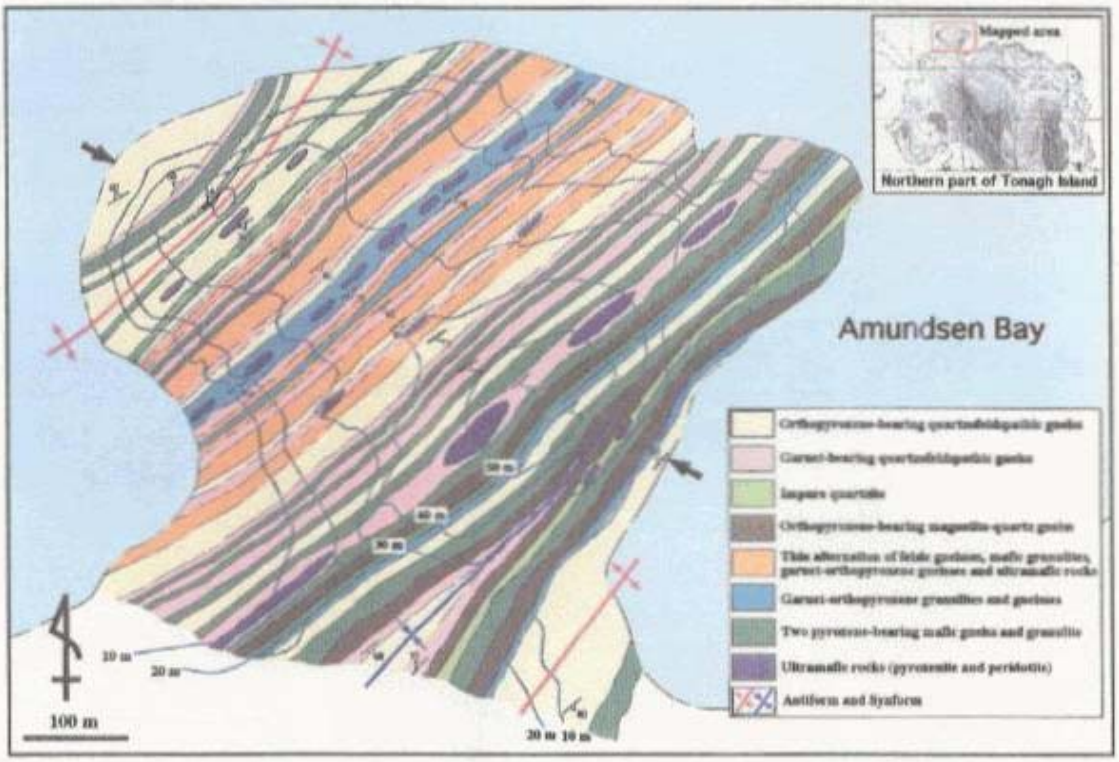

Fig. 2.6 (b)

Fig. 2.6 Geological map of Tonagh Island, which was already published as Osanai *et al.*, (1999). (a) Generalized geological map and cross section of the Tonagh Island. (b) Detailed geological map of the northern peninsular area of the island.

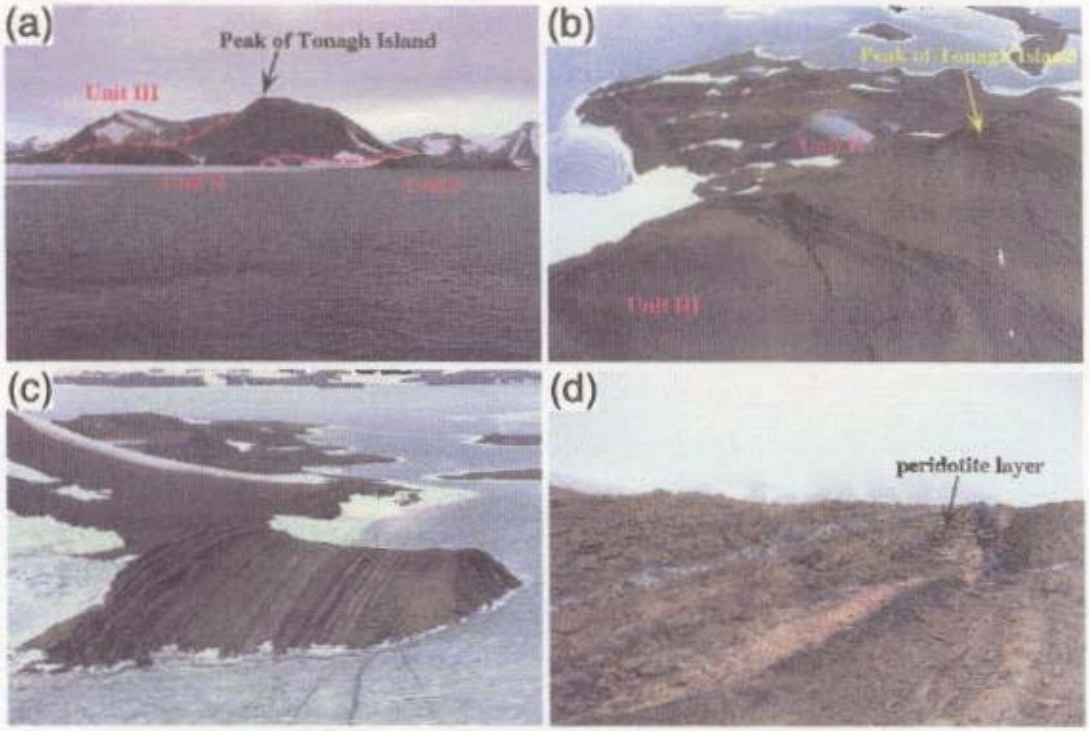

Fig. 2.7 (a) Tonagh Island (northern part) view from north. Orthopyroxene felsic gneiss and mafic granulite constitute the main body (Units II and III) of the Island. (b) Shear zone dividing the Units II and III. (c) Well-layered structure of meters to centimeters order alternation of felsic gneisses, mafic granulite, garnet gneiss, garnet-orthopyroxene gneiss and ultramafic rocks in northern peninsular area of Tonagh Island, as shown in Fig. 2.6b. (d) Close up view of northern peninsular area. Orthopyroxene felsic gneiss (pale greenish brown), garnet-bearing leucocratic quartzo-feldspathic (felsic) gneiss (grey), garnet gneiss (orange), peridotite (pale green) and pyroxenite (black) constitute the layered sequences.

Ishizuka *et al* ., (1998) **Fig. 2.4** - Mt. Riiser-Larsen	Osanai *et al* ., (1999) **Fig. 2.6** - Tonagh Island	This study (used in the text)
orthopyroxene felsic gneiss	orthopyroxene-bearing quartzo-feldspathic gneiss	orthopyroxene felsic gneiss
garnet-poor garnet felsic gneiss	garnet-bearing quartzo-feldspathic gneiss	garnet felsic gneiss
basic-intermediate gneiss including leuco-gabbro to -norite	two pyroxene-bearing mafic granulite	two-pyroxene mafic granulite
garnet-rich garnet felsic gneiss		garnet gneiss
quartz-rich garnet felsic gneiss		quartzo-feldspathic gneiss
garnet-orthopyroxene felsic gneiss		quartzo-feldspathic gneiss or garnet-orthopyroxene gneiss
	garnet-orthopyroxene granulite	garnet-orthopyroxene gneiss
pelitic gneiss		garnet-sillimanite gneiss
meta-BIF	magnetite-quartz gneiss	magnetite-quartz gneiss
dike rocks	unmetamorphosed mafic dyke	mafic dike

Table 2.1 Comparison of rock names used in geological map of the Mt. Riiser-Larsen area (Ishizuka *et al.*, 1998), that of Tonagh Island (Osanai *et al.*, 1999) and in the text of this thesis.

Chapter 3 Petrology and Metamorphism of Sapphirine and Osumilite-bearing Gneisses from the Mt. Riiser-Larsen

Abstract: The Mt. Riiser-Larsen area is divided into two parts, the central and the western areas, which are bounded by the shear zone composed of mylonite and pseudotachylite with dipping nearly vertically. Mg-rich aluminous, siliceous and quartzo-feldspathic gneisses contain sapphirine + quartz and osumilite , which are diagnostic of ultrahigh-temperature (UHT) metamorphism. Mineral parageneses of sapphirine + orthopyroxene + quartz, sapphirine + garnet + quartz and garnet + osumilite, and reaction textures after sapphirine + quartz producing cordierite and/or garnet observed in the gneisses from the central area constrain the peak P-T conditions as > 1040°C and 0.6 ~ 0.8 GPa. Whereas, the peak P-T conditions of the western area is constrained by sapphirine + orthopyroxene + quartz paragenesis and the occurrence of osumilite, and by the reaction texture after sapphirine + quartz producing orthopyroxene + sillimanite, as > 1030°C and 0.8 ~ 0.9 GPa. Consequently, the western part of the Mt. Riiser-Larsen area represents a deeper structural level than the central part, and they have juxtaposed due to the movement along the shear zone after isobaric cooling. Westward increasing pressure estimated here is oblique to the regional pressure gradient of the pressure increasing southward within the Napier Complex, which is interpreted by Harley and Hensen (1990). However, it is not inconsistent with the exhumation process of the Napier Complex in relation with the compressional tectonic event of the Rayner Complex westward in the coastal region of the Napier Complex.

3.1. Introduction

In this chapter, the modes of occurrences and petrography of sapphirine, spinel and osumilite-bearing gneisses from the Mt. Riiser-Larsen area are described, and the metamorphic conditions are discussed with respect to the phase relations. Sapphirine and osumilite are generally contained in relatively Mg-rich quartzo-feldspathic, siliceous or aluminous gneisses, and are occasionally contained in garnet gneiss, garnet-sillimanite gneiss or garnet-orthopyroxene gneiss, which might be derived from pelitic or psammitic precursors. The mode of occurrences and mineral assemblages of these gneisses are various. Based on the modal proportions of quartz and feldspar, they are classified into following rock types: (a) quartzo-feldspathic gneiss, rich in quartz and feldspar, (b) siliceous gneiss, rich in quartz and poor in (or lack of) feldspar, (c) quartz-bearing aluminous gneiss, containing minor quartz, (d)

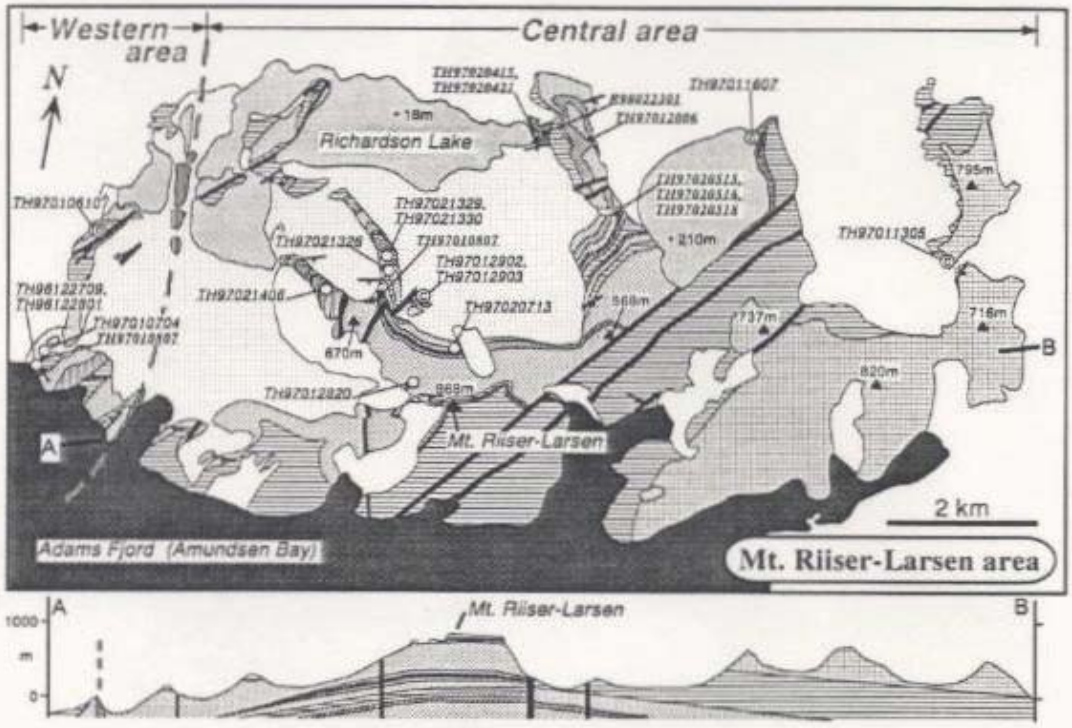

Archaean UHT rocks

- Opx felsic gneiss
- Layered gneiss composed mainly of
  - Opx felsic gneiss
  - Grt felsic gneiss
  - Grt gneiss, Grt-Sil gneiss
  - Mafic granulite
  - Quartzo-feldspathic gneiss (Spr-bearing)
  - Grt-Opx quartzo-feldspathic gneiss
  - Impure quartzite

Proterozoic and Cenozoic

- Mafic dike
- Riiser-Larsen Main Shear Zone
- Quaternary (moraine)
- Sea
- Lake, Pond
- Ice sheat, Snow cover
- Peak of Mt. Riiser-Larsen

TH97010704 **Sample locality of sapphirine+quartz**

- ○ **Direct contact of sapphirine + quartz**
- ◎ **Cordierite and/or garnet after sapphirine + quartz**
- ◉ **Orthopyroxene + sillimanite after sapphirine + quartz**

TH97010907 **Sample locality of analyzed feldspar (chapter 5)**

Fig. 3.1 Simplified geological map and geological cross section of the Mt. Riiser-Larsen area. The sample localities of sapphirine + quartz and those of feldspar analyses (chapter 5) are also shown.

Sample No.	Area	Type	Qtz	Pl	Akfs	Opx	Grt	Spr	Os	Spl	Sil	Crd	Bt	*Spr+Qtz*
Central area of the Mt. Riiser-Larsen														
TH97020713	C	QF	O	O		O		O			L		L	direct
TH97012820	C	QF	O	O		O		O			L		L	direct
TH97011607	C	S	OO			O		O	O			R	L	Crd
TH97012903	C	S	OO		L	O	L/R	O	O	L	L	R	L	Crd,Grt
TH97021326	C	S	OO		L	O		O	O		L			direct
TH97021406	C	S	OO			O		O	O					direct
TH97021329	C	IQ	OO		L			L		L			L	direct
TH97021330	C	IQ	OO		L			L		L			L	direct
TH97011305	C	QA	O	L		O		O	O		L	R	L	Crd
TH97011707	C	QA	O		L	O	L	O	O	L	L	R	L	
TH97011709	C	QA	O		L		O	L	O		R			
TH97012013	C	QA	L		L	O	L	O	O					
TH97012803	C	QA	O		O		O		O		L			
TH97012902	C	QA	O		L	O	L/R	O				R	L	Crd,Grt
TH97020414	C	QA	O			O		O	O		L		L	
TH97020415	C	QA	O	O	O	O		O	O		L	R	L	
R98022301D	C	QA												
TH97010820	C	A		O		L		O					O	
TH97020421	C	A			O	O		O		L		R	L	
TH97020427	C	A			O	O		O	O			R		
TH97010516	C	G	O	O			O			L	L		L	
TH97020416	C	G	L		O		O	L		L				
TH97020518	C	G	O		O		O		S		O			
TH97021321	C	GS	O	O			O			L	O			
Western area of the Mt. Riiser-Larsen														
TH96122709	W	QF	O	O		O		O			L			direct
TH96122801	W	QF	O	O		O		O	O		L			direct
TH97010610	W	QF	O	O		O/R		O		L	L/R		L	Opx+Sil
TH97010615	W	QF	O	O		O	L	O		L	L		L	
TH97010705	W	QF	O	O		O		O	S		L		L	direct
TH97021105	W	A			O	O		O		O			L	

Table 3.1 Constituent minerals of sapphirine, spinel or osumilite-bearing gneisses from the Mt. Riiser-Larsen area. QF: quartzo-feldspathic gneiss. S: silicous gneiss. IQ: impure quartzite. QA: quartz-bearing aluminous gneiss. A: silica-undersaturated aluminous gneiss. G: garnet gneiss. GS: garnet-sillimanite gneiss. O:present, OO:large amount, L:local, R:retrograde, S:symplectite. Mineral abbreviations essentially follow Kretz (1983): Qtz: quartz, Pl: plagioclase, Akfs: alkali feldspar, Opx: orthopyroxene, Grt: garnet, Sil: sillimanite, Spr: sapphirine, Os: osumilite, Spl: spinel, Crd: cordierite, Bt: biotite~phlogopite.

silica-undersaturated aluminous gneiss, lack of quartz and (e) garnet, garnet-sillimanite, garnet-orthopyroxene-nearing gneisses.

Metamorphic P-T conditions of the Napier Complex are estimated as >1000°C for rocks of sapphirine + quartz association based on the results of synthetic experiments (Hensen and Green, 1971; Hensen and Green, 1972; Hensen and Green, 1973; Bertrand *et al.*, 1991). Experimentally determined stability field of osumilite (Motoyoshi *et al.*, 1993; Audibert *et al.*, 1995; Carrington and Harley, 1995a; 1995b) and calculations using geobarometers (Harley, 1983; Harley, 1985; Ellis and Green, 1985; Sandiford, 1985) constrain the pressure conditions of the Napier Complex less than 1.0 ~ 1.1 GPa.

A variety of reaction textures during cooling stage after UHT conditions are reported from the metamorphic rocks in the Napier Complex (Harley, 1985; Harley and Hensen, 1990; Harley, 1998). Harley (1998) suggests that the reaction textures of sapphirine + quartz rimmed by coronas involving combination of cordierite, sillimanite and garnet in the northern areas represent lower pressures during cooling stage than those of sapphirine + quartz rimmed by orthopyroxene + sillimanite in the areas south of the Amundsen Bay region. However, both of these two types of reaction textures are found from the Mt. Riiser-Larsen area, which could provide significant information on the pressure conditions of the Mt. Riiser-Larsen and regional pressure gradient within the Napier Complex.

3.2. Field occurrence and petrography

The field occurrence and petrography of sapphirine and osumilite-bearing gneisses from the Mt. Riiser-Larsen area are described. Sample localities and constituent minerals are summarized in Fig. 3.1 and Table 3.1.

(a) Sapphirine and osumilite-bearing quartzo-feldspathic gneiss (Fig. 3.2)

Quartzo-feldspathic gneisses containing sapphirine with or without osumilite show characteristic white-colored appearance in the field (Fig. 3.2a). It occurs as up to 20 m in thickness. Well layered compositional banding of quartzo-feldspathic whitish portion and sapphirine-bearing bluish layers is developed (Fig. 3.2b). Major constituent minerals are quartz, plagioclase and orthopyroxene. Sapphirine is restricted in thin layers and is always associated with quartz (Figs. 3.2c and d). Sillimanite and occasionally osumilite are contained as minor phases.

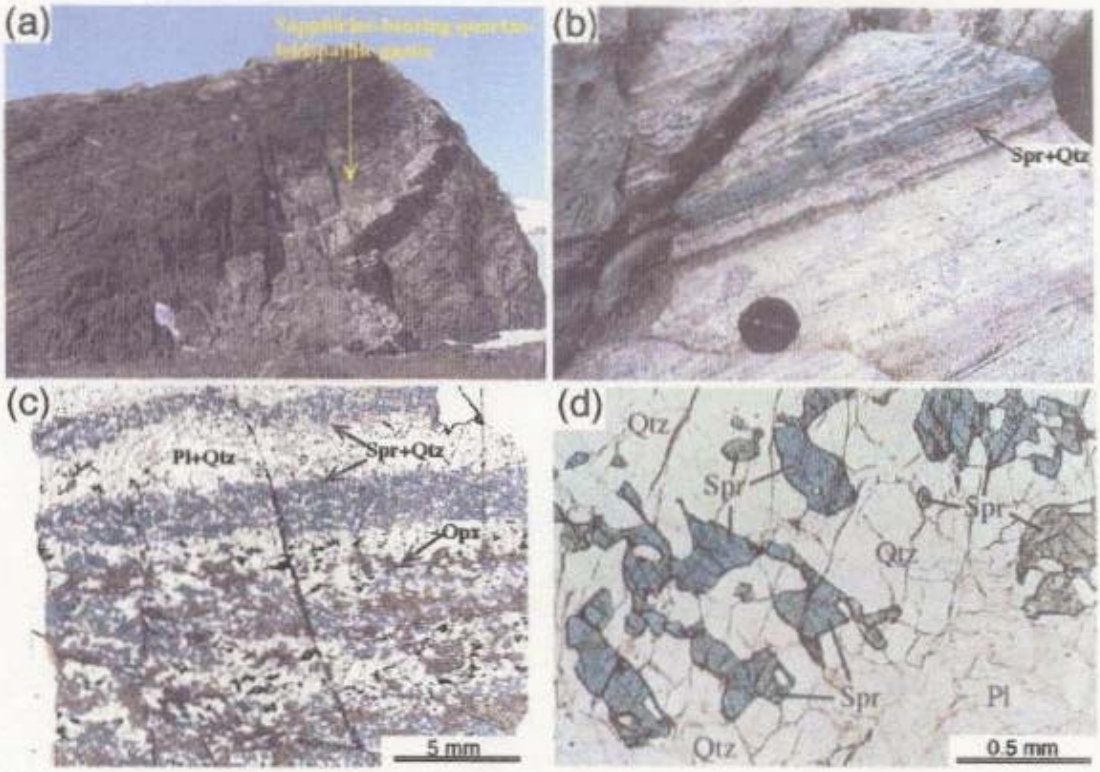

Fig. 3.2 Quartzo-feldspathic gneiss containing sapphirine. (a) Sapphirine-bearing quartzo-feldspathic gneiss layer of 20 m thick (white). Upper structural layer is orthopyroxene-bearing quartzo-feldspathic gneiss (brown) and lower structural layers are mafic granulite (dark brown) and garnet-orthopyroxene-bearing quartzo-feldspathic gneiss (pale brown). (b) Close up view of sapphirine-bearing quartzo-feldspathic gneiss. (c) Photomicrograph of the sapphirine-bearing quartzo-feldspathic gneiss. Sapphirine occurs in a thin layer intergrowth with quartz and/or orthopyroxene. Plane-polarized light. (d) Photomicrograph of sapphirine in direct contact with quartz (TH96122709). Plane-polarized light.

(b) Sapphirine, osumilite and spinel-bearing siliceous gneiss (Fig. 3.3)

It occurs as white to pale blue-colored rock. Quartz is the most dominant phase in the gneiss. The lithology is heterogeneous and in some cases varies gradually from quartz-rich siliceous gneiss to quartz-poor aluminous gneiss. In some localities, sapphirine, which is intergrowth with quartz, occurs as a patch discordant to the foliation defined by the alignment of orthopyroxene (Fig. 3.3a). Major constituents are quartz, orthopyroxene, sapphirine. Osumilite, sillimanite, garnet and alkali feldspar are occasionally contained in the gneiss. Sapphirine is generally surrounded by quartz, and sometimes by osumilite (Fig. 3.3c). Spinel is contained in some rock types of siliceous gneiss, and is also in direct contact with quartz (Fig. 3.3d).

(c) Sapphirine and osumilite in quartz-bearing aluminous gneiss (Fig. 3.4)

Sapphirine and osumilite are commonly contained in heterogeneous aluminous gneisses composed of the combinations of following minerals: quartz, alkali feldspar, plagioclase, orthopyroxene, garnet, sillimanite, sapphirine and osumilite. They show quite heterogeneous modes of occurrences (Fig. 3.4a). Both sapphirine and quartz are contained in the gneisses, but they usually do not directly contact with each other. Sapphirine is generally surrounded by alkali feldspar, osumilite or garnet (Fig. 3.4d).

(d) Sapphirine, spinel and osumilite in silica-undersaturated aluminous gneiss (Fig. 3.5)

Sapphirine is a common constituent in the silica-undersaturated aluminous gneisses, which occurs as a lens or a block in quartzo-feldspathic gneisses or as a quartz-free-portion of aluminous gneisses. Sapphirine in silica-undersaturated aluminous gneisses is commonly idiomorphic porphyroblast (Figs. 3.5a, b and c) and is always associated with either alkali feldspar or phlogopite. Other main constituents are orthopyroxene, spinel, garnet or osumilite.

(e) Sapphirine and spinel in garnet and garnet-sillimanite gneisses (Fig. 3.6)

Brown or brownish green spinel is a common constituent in garnet and garnet-sillimanite gneisses. It is in many cases enclosed within or surrounded by garnet or sillimanite (Fig. 3.6d). Sapphirine is occasionally contained and is also surrounded by garnet or sillimanite (Fig. 3.6c). Other constituents are plagioclase, alkali feldspar and quartz.

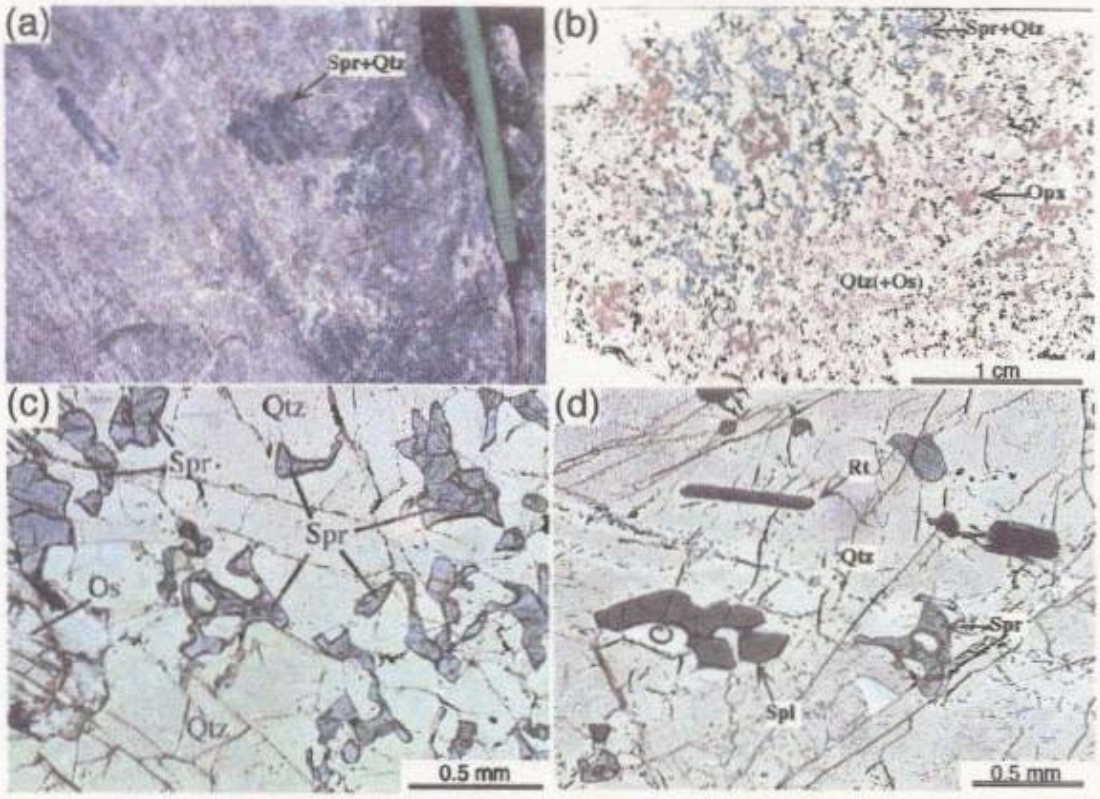

Fig. 3.3 Siliceous gneiss containing sapphirine. (a) Sapphirine occurs as pod in siliceous gneiss composed of quartz, orthopyroxene and osumilite. (b) Photomicrograph of sapphirine-bearing siliceous gneiss (TH97021326). Plane-polarized light. (c) Sapphirine in direct contact with quartz (TH97021326). Plane-polarized light. (d) Spinel in direct contact with quartz is occasionally observed in siliceous gneiss (TH97012903). Plane-polarized light.

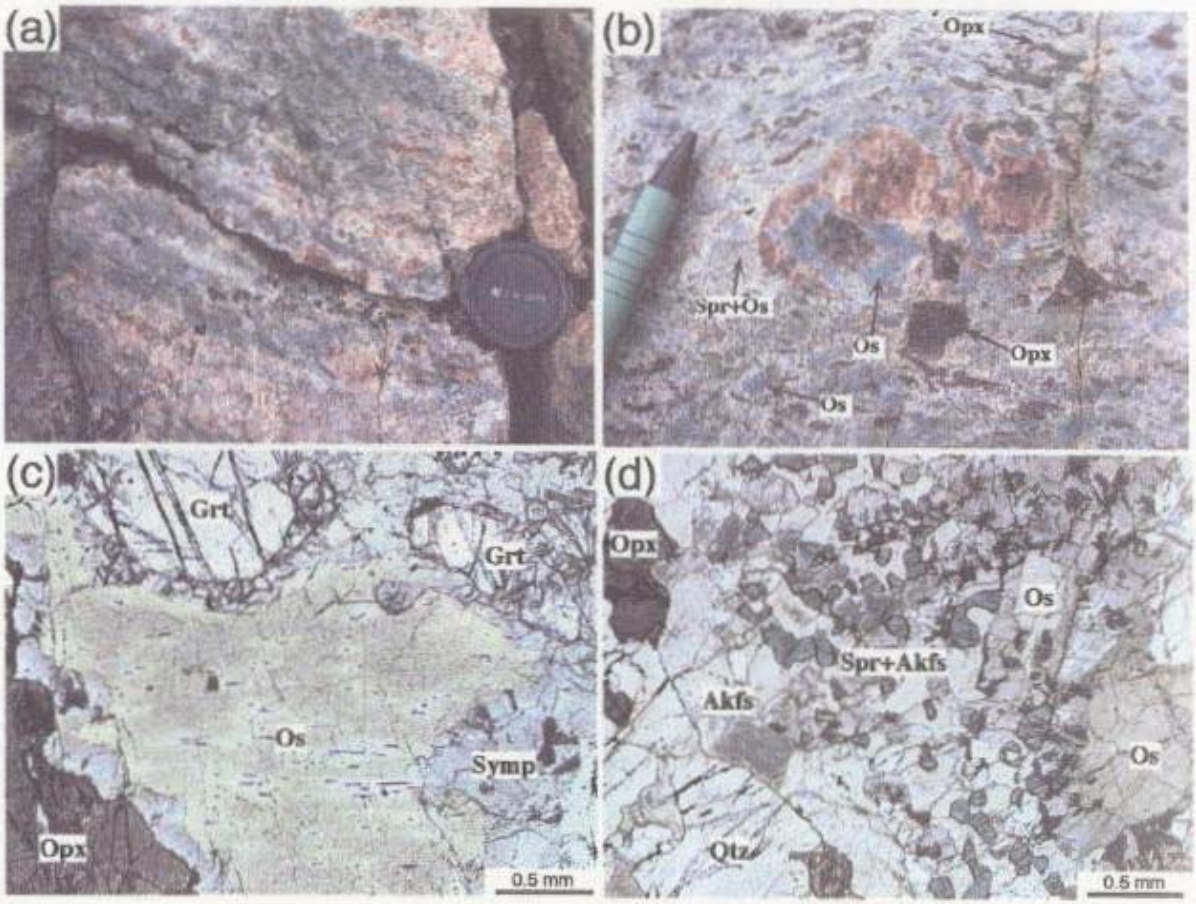

Fig. 3.4 Quartz-bearing aluminous gneiss containing sapphirine. (a) Heterogeneous aluminous gneiss, composed of sapphirine, orthopyroxene, garnet, osumilite and quartz. (b) Sapphirine-orthopyroxene-osumilite-quartz gneiss containing occasionally garnet. (c) Photomicrograph of aluminous gneiss containing garnet, osumilite, orthopyroxene and quartz. Osumilite is commonly surrounded by fine-grained symplectite of cordierite-K-feldspar-quartz-orthopyroxene (Symp). Plane-polarized light. (d) Photomicrograph of aluminous gneiss composed of sapphirine, orthopyroxene, osumilite, plagioclase, alkali feldspar and quartz. Sapphirine is generally surrounded by alkali feldspar or osumilite, and does not directly contact with quartz (TH97020415). Plane-polarized light.

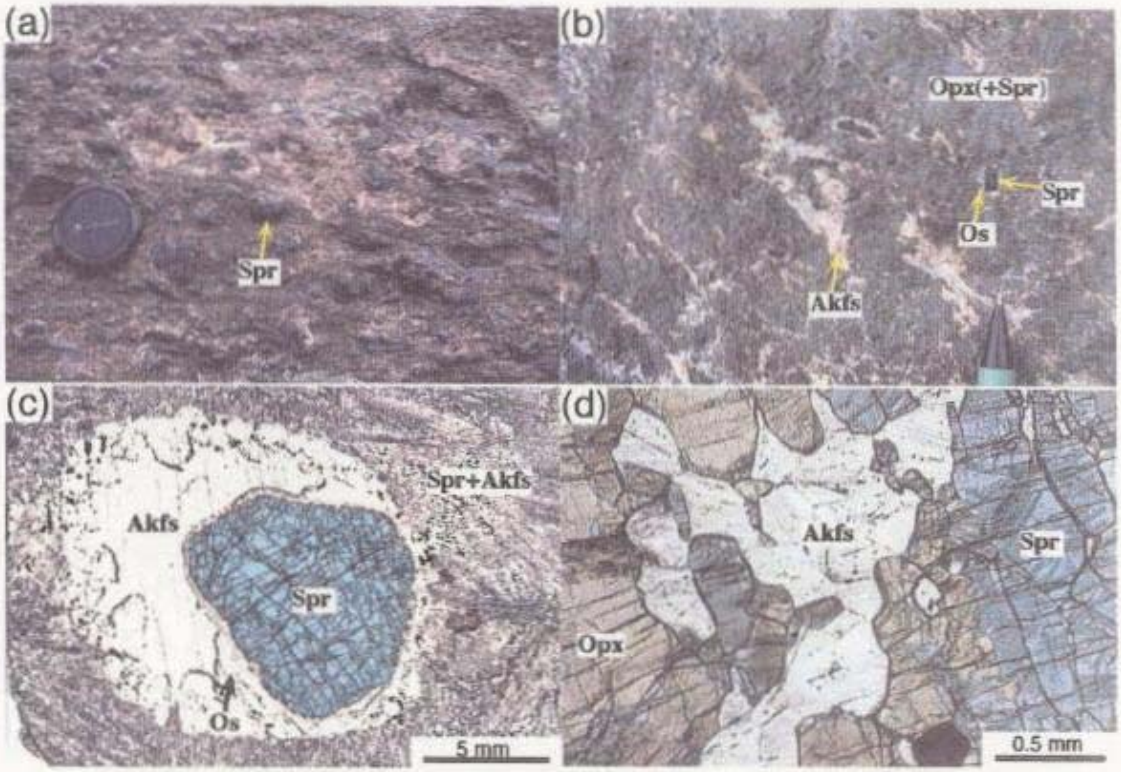

Fig. 3.5 Silica-undersaturated aluminous gneiss containing sapphirine. (a) Sapphirine and phlogopite-bearing silica-undersaturated aluminous gneiss. Coarse-grained garnet occasionally occurs and includes idiomorphic sapphirine. (b) Silica-undersaturated aluminous gneiss composed of sapphirine, orthopyroxene, alkali feldspar and osumilite. Idiomorphic sapphirine is surrounded by veinlike alkali feldspar, and osumilite occurs around sapphirine. (c) Photomicrograph of TH97020427. Idiomorphic sapphirine is surrounded by alkali feldspar. Osumilite also occurs around alkali feldspar. Fine-grained symplectite of sapphirine and alkali feldspar constitite the matrix. Plane-polarized light. (d) Photomicrograph of TH97020421. It is composed of sapphirine, orthopyroxene and alkali feldspar. Plane-polarized light.

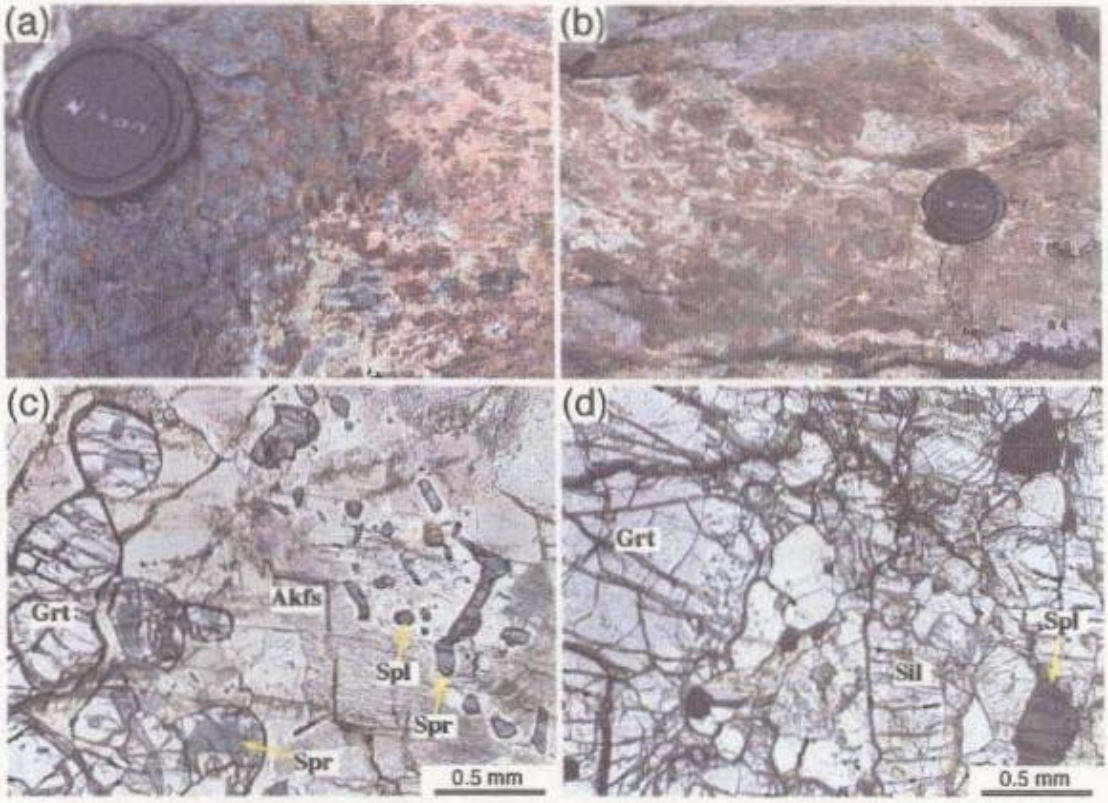

Fig. 3.6 Garnet gneiss and garnet-sillimanite gneiss containing sapphirine or spinel. (a) Garnet gneiss containing sapphirine and spinel. (b) Garnet-sillimanite gneiss containing spinel. (c) Photomicrograph of garnet gneiss (TH97020416). Plane polarized light. (d) Photomicrograph of garnet-sillimanite gneiss (TH97021321). Plane polarized light.

3.3. Petrography and mineral textures of sapphirine + quartz

In this section, petrography and mineral textures of sapphirine and quartz in direct contact with each other, and the reaction textures after sapphirine + quartz are described.

3.3.1. Central area of the Mt. Riiser-Larsen

A variety of sapphirine-quartz-bearing gneisses occur as thin layers or lenses in quartzo-feldspathic gneisses in the central part of the Mt. Riiser-Larsen area, but a few of them display direct contact of sapphirine and quartz. Direct contact of sapphirine and quartz is observed at 7 localities (TH97011305, TH97011607, TH97012902-03, TH97020713, TH97012820, TH97021326, TH97021406 in Fig. 3.1), among which thin cordierite and/or garnet film occur between sapphirine and quartz as retrograde product at 3 localities (TH97011305, TH97011607, TH97012902-03). Constituent minerals and textural features are summarized in Table 3.1.

(a) Mode of occurrence of sapphirine in direct contact with quartz (TH97020713, TH97012820, TH97021326, TH97021406)

Sapphirine is generally xenomorphic and less than 1 mm in diameter. It occurs interstitially against the quartz grain with rounded convex shape, or is surrounded by coarse-grained quartz (Fig. 3.3c). No reaction texture is observed between sapphirine and quartz. Quartz is granoblastic with partly rounded shape and ranges in grain size from several hundreds of micrometers to a centimeter. The sapphirine-quartz aggregate occurs as heterogeneous clots locally in the rock. Orthopyroxene and plagioclase (TH97020713, TH97012820), or osumilite (TH97021326, TH97021406) are the other coexisting minerals with sapphirine and quartz. Orthopyroxene and plagioclase are also granoblastic, but osumilite is xenomorphic and occurs interstitially against the quartz grain. Osumilite is frequently replaced by fine-grained (less than 1 μm) symplectite of cordierite-K-feldspar-quartz-orthopyroxene. Idiomorphic sillimanite is present locally and is commonly enclosed within quartz. Osumilite occasionally includes sapphirine and sillimanite. Rutile, monazite and zircon are minor constituents. Retrograde biotite rarely occurs.

(b) Reaction textures of cordierite and/or garnet after sapphirine + quartz (TH97011305, TH97011607, TH97012902-03)

Mode of occurrence of sapphirine and other constituents is similar to that in the sapphirine + quartz-baring gneisses described above, except thin cordierite and/or garnet films occur around sapphirine (Fig. 3.7). In some cases fine-grained sapphirine grains form symplectite-like aggregate with quartz (Fig. 3.7c), and is different from the mode of occurrence described above. Fine-grained spinel occurs in the sample TH97012903, and is included in sapphirine, quartz, garnet, osumilite or orthopyroxene. The reaction textures after sapphirine + quartz are classified into the following types:

(1) Cordierite film occurs between sapphirine and quartz (TH97011305, TH97011607, TH97012902, TH97012903)

(2) Cordierite film occurs among sapphirine, quartz and orthopyroxene (TH97011305, TH97012902)

(3) Garnet film occurs between sapphirine and quartz (TH97012903)

(4) Cordierite and garnet films occur among sapphirine, quartz and orthopyroxene (TH97012902)

The degree of development of reaction textures vary in the gneisses. In the sample TH97012903, both reaction texture developed and free portions are observed in one sample. Whereas, few direct contact of sapphirine and quartz are remained in the samples TH97011305 and TH97012902, or cordierite perfectly replaces the grain boundary between sapphirine and quartz and no direct contact of sapphirine and quartz is observed in the sample TH97011607.

(c) Mode of occurrence of sapphirine and quartz without direct contact with each other

Gneisses including sapphirine and quartz without directly contact with each other are observed at several localities in the central area. Mode of occurrence and mineral assemblage are various. Sapphirine is commonly surrounded by alkali feldspar (Fig. 3.4d) or osumilite, and sometimes by orthopyroxene or plagioclase. It also occurs as inclusion of garnet and sillimanite in garnet gneiss or garnet-sillimanite gneiss. Sapphirine is generally xenomorphic and less than 1 mm in diameter. Quartz is generally granoblastic with partly rounded shape and ranges in grain size from several hundreds of micrometers to several millimeters. It sometimes occurs as elongated porphyroblast up to a centimeter in length. Osumilite surrounding sapphirine is largely replaced by fine-grained (less than 1 μm) symplectite of cordierite-K-feldspar-quartz-orthopyroxene. Sapphirine and quartz are now

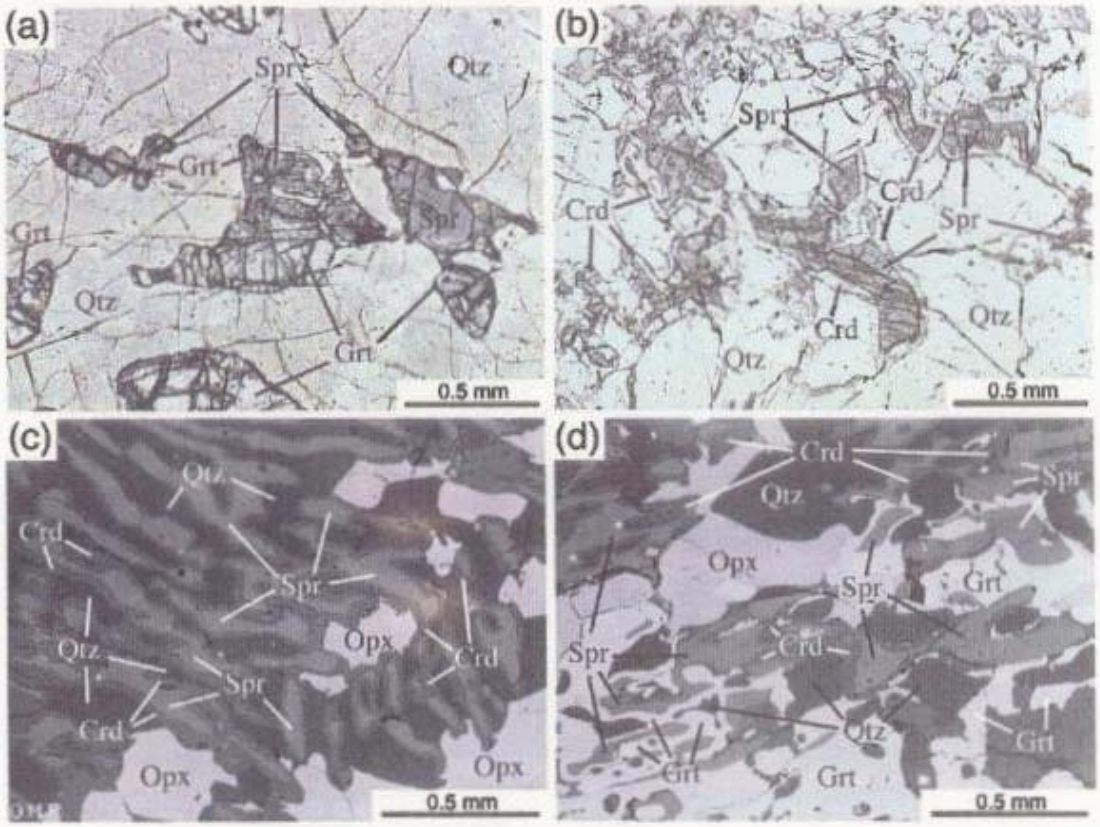

Fig. 3.7 Reaction textures after sapphirine + quartz in the central area of the Mt. Riiser-Larsen. (a) Photomicrograph of the reaction texture that garnet is formed between sapphirine and quartz in siliceous gneiss (TH97012903). Plane-polarized light. (b) Photomicrograph of the reaction texture that cordierite replaces sapphirine + quartz (TH97011607). Plane-polarized light. (c) Backscattered electron image of the reaction texture that cordierite is formed from sapphirine + quartz (+ orthopyroxene) (TH97012902). (d) Backscattered electron image of the reaction texture that cordierite and/or garnet replaces sapphirine + quartz + orthopyroxene (TH97012902).

separated by other minerals, but may have coexististed with each other at the peak metamorphism.

3.3.2. *Western area of the Mt. Riiser-Larsen*

Unique sapphirine-orthopyroxene-bearing quartzo-feldspathic gneiss is the only sapphirine-quartz-bearing gneiss in the area, and are observed at 3 localities (TH96122709-TH96122801, TH97010705 and TH97010610 in Fig. 3.1).

(a) Mode of occurrence of sapphirine in direct contact with quartz (TH96122709-TH96122801, TH97010705)

Main constituents are sapphirine, orthopyroxene, quartz and plagioclase, and osumilite and sillimanite are also present locally. Granoblastic quartz and plagioclase are main constituents of the rock. Sapphirine and orthopyroxene occur forming a layer of the gneiss. Sapphirine is xenomorphic and less than 1 mm in diameter. No reaction texture between sapphirine and quartz is developed (Fig. 3.2d). Orthopyroxene and plagioclase are generally millimeter order in diameter. Quartz is also equidimensional but some grains are up to centimeter order. Sillimanite is idiomorphic up to 5 mm in length. It occurs separately from sapphirine and is always associated with quartz. Osumilite is largely replaced by fine-grained (less than 1 mm) cordierite-K-feldspar-orthopyroxene-quartz symplectite. Other minor constituents are rutile, zircon and monazite. Biotite is scarcely present as retrograde product.

(b) Reaction texture of orthopyroxene + sillimanite after sapphirine + quartz (TH97010610)

Mode of occurrence of sapphirine and other constituents is similar to that in the sapphirine + quartz-baring gneisses described above, except thin orthopyroxene + sillimanite film occurring between sapphirine and quartz (Fig. 3.8). Sillimanite is formed at sapphirine side and orthopyroxene is at quartz side. Chemical compositions of orthopyroxene film are significantly lower Al_2O_3 content than those in the matrix.

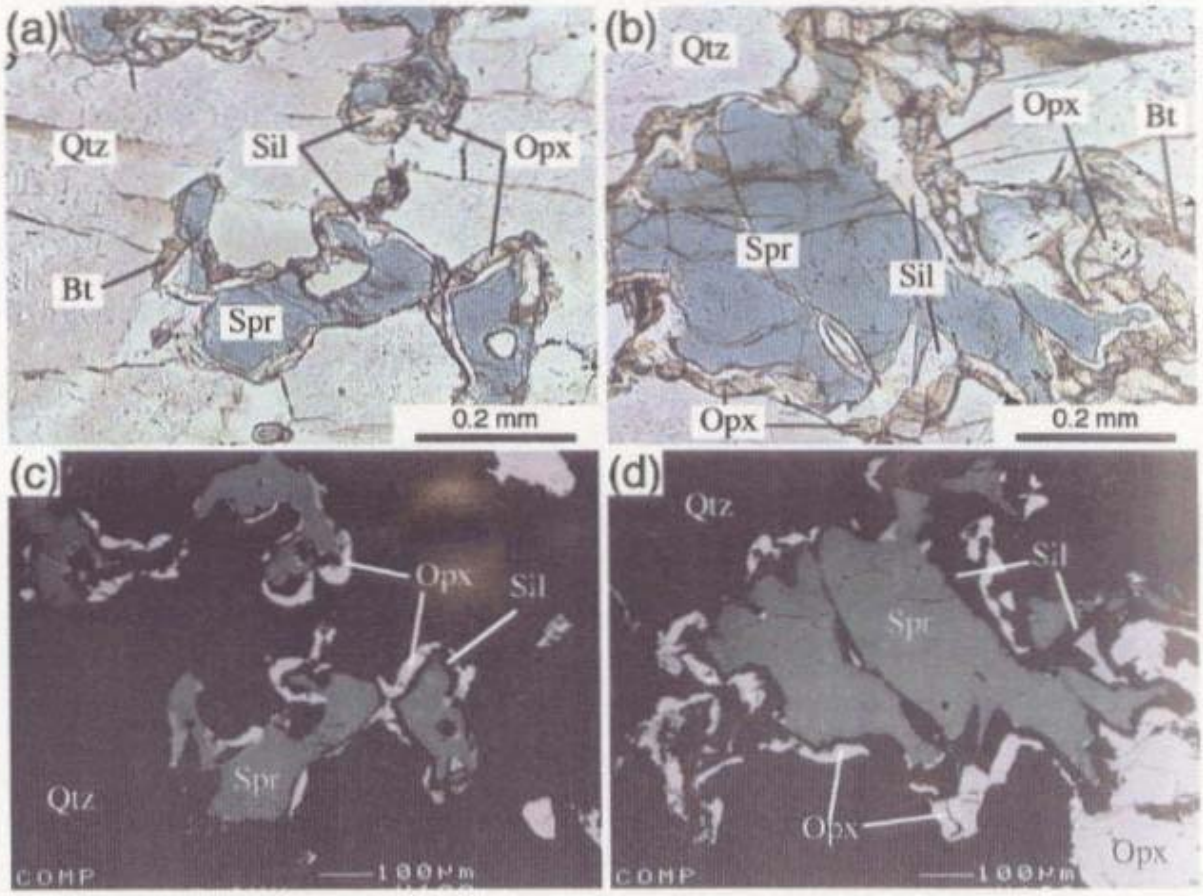

Fig. 3.8 Reaction textures after sapphirine + quartz in the western area of the Mt. Riiser-Larsen. (a) and (b) Photomicrograph of the reaction texture that orthopyroxene + sillimanite is formed between sapphirine and quartz (TH97010610). Plane-polarized light. (c) and (d) Backscattered electron image of the reaction textures.

3.4. Mineral chemistry

Chemical analyses of constituent minerals were performed using an electron microprobe with an wavelength-dispersive X-ray analytical system (JEOL JXA-8800M) at the National Institute of Polar Research. Oxide ZAF correction was applied to analyses. Probe current was kept at about 8 nA with accelerating voltage at 15 kV. Synthesized pure oxides and natural minerals were used for standards. Representative analyses are shown in Table 3.2.

(a) Sapphirine

Sapphirine shows pleochroism of pale blue to colorless. Mg / (Mg + Fe) ratio (X_{Mg}) ranges from 0.71 to 0.93, which is mainly controlled by bulk chemical compositions (Fig. 3.9). No systematic compositional differences among rock types is detected. Coarse-grained sapphirine displays weak compositional zoning of Al-increasing and Si-decreasing toward the rim, as is the similar to that described in Ellis (1980) and Harley (1986).

(b) Orthopyroxene

X_{Mg} of orthopyroxene rages from 0.63 to 0.83, which is considerably higher than those ranging from 0.48 to 0.54 in sapphirine-free orthopyroxene-bearing quartzo-feldspathic gneiss (TH97010807) (Fig. 3.10). Coarse-grained orthopyroxene commonly displays compositional zoning of Al_2O_3 content-decreasing toward the rim.

(c) Garnet

Garnet has X_{Mg} ranging from 0.49 to 0.56 (Fig. 3.11). Garnet is characterized by considerably low grossular (less than 3 mol%) and spessartine (less than 1 mol%) contents, except that in quartzo-feldspathic gneiss. Garnet in quartzo-feldspathic gneisses (TH97020516, TH97012006) shows considerably higher almandine and grossular and lower pyrope contents than those from sapphirine-bearing relatively magnesian gneisses.

(d) Osumilite

Osumilite shows the highest X_{Mg} (0.85 ~ 0.94) among the constituent minerals (Fig. 3.12). It displays pleochroism of pale yellowish white to colorless. Na/(Ca + Na + K) ratios in osumilite generally ranges from 0.05 to 0.15.

Table 3.2 Representative electron microprobe analyses of constituent minerals

mineral											Sapphirine											
sample	TH961-22709	TH970-10610	TH970-10615	TH970-10705	TH970-10820	TH970-11305	TH970-11607	TH970-11707	TH970-11709	TH970-12013	TH970-12902	TH970-12903	TH970-20414	TH970-20415	TH970-20416	TH970-20421	TH970-20427	TH970-20713	TH970-21105	TH970-21326	TH970-21406	R9802-2301D
point	101	8	76	2-17	3	133	10	188	101	138	38	132	66	34	17	40	18	29	8	60	88	128
wt %																						
SiO2	14.99	14.24	13.32	13.06	14.23	13.45	13.51	13.72	13.53	14.29	13.91	13.45	13.47	13.22	13.51	14.42	13.72	14.33	13.90	14.33	13.86	14.36
TiO2	0.06	0.00	0.00	0.00	0.02	0.00	0.02	0.00	0.03	0.03	0.02	0.00	0.05	0.06	0.01	0.05	0.08	0.05	0.08	0.08	0.03	0.05
Al2O3	60.70	61.26	63.24	62.20	62.99	62.35	63.66	58.79	62.40	61.61	61.99	61.27	61.09	61.16	61.51	61.12	61.95	60.95	60.12	60.86	62.59	60.20
Cr2O3	0.02	0.09	0.13	0.02	0.05	0.06	0.06	0.01	0.03	0.06	0.06	1.58			0.02		0.00	0.13	0.09	0.02	0.06	0.04
FeO*	6.99	9.01	8.20	6.40	2.77	7.77	6.35	11.39	7.66	8.22	7.31	7.25	8.58	8.71	8.29	5.72	5.64	8.75	9.10	7.23	7.42	10.21
MnO	0.00	0.11	0.09	0.05	0.01	0.05	0.09	0.05	0.05	0.01	0.05	0.03	0.02	0.00	0.06	0.03	0.00	0.01	0.02	0.00	0.01	0.01
ZnO	0.12	0.00	0.00	0.00	0.08	0.01	0.13	0.00	0.09	0.00	0.02	0.00						0.00	0.10	0.00	0.00	0.00
MgO	16.95	15.74	15.45	17.18	19.43	16.69	17.03	15.46	16.05	15.77	16.51	16.35	16.40	16.53	16.78	18.55	18.68	16.22	16.48	17.28	16.61	15.20
CaO	0.04	0.02	0.00	0.00	0.01	0.00	0.00	0.02	0.02	0.01	0.05	0.04	0.00	0.01	0.00	0.00	0.00	0.00	0.04	0.00	0.00	0.02
Na2O	0.01	0.03	0.00	0.03	0.00	0.02	0.00	0.00	0.00	0.00	0.00	0.00	0.08	0.03	0.06	0.00	0.00	0.02	0.02	0.00	0.00	0.08
K2O	0.00	0.00	0.00	0.00	0.00	0.00	0.00	0.00	0.00	0.00	0.00	0.00	0.00	0.00	0.00	0.00	0.00	0.00	0.00	0.00	0.00	0.00
total	99.88	100.50	100.43	98.94	99.59	100.40	100.85	99.44	99.86	100.00	99.92	99.97	99.69	99.72	100.24	99.89	100.07	100.46	99.95	99.80	100.58	100.17
cations (O=20)																						
Si	1.778	1.695	1.581	1.563	1.662	1.595	1.585	1.673	1.612	1.701	1.652	1.605	1.616	1.587	1.610	1.702	1.618	1.704	1.668	1.704	1.636	1.724
Ti	0.005	0.000	0.000	0.000	0.002	0.000	0.002	0.000	0.003	0.003	0.002	0.000	0.005	0.005	0.001	0.004	0.007	0.004	0.007	0.007	0.003	0.005
Al	8.483	8.594	8.843	8.771	8.668	8.715	8.799	8.449	8.759	8.643	8.680	8.617	8.636	8.652	8.637	8.503	8.608	8.543	8.504	8.529	8.706	8.519
Cr	0.002	0.008	0.012	0.002	0.005	0.006	0.006	0.001	0.003	0.006	0.005	0.149	0.000	0.000	0.002	0.000	0.000	0.012	0.009	0.002	0.006	0.004
Fe	0.693	0.897	0.814	0.640	0.270	0.771	0.623	1.161	0.763	0.818	0.726	0.723	0.861	0.874	0.826	0.565	0.556	0.870	0.913	0.719	0.732	1.025
Mn	0.000	0.011	0.009	0.005	0.001	0.005	0.009	0.005	0.005	0.001	0.005	0.003	0.002	0.000	0.006	0.003	0.000	0.001	0.002	0.000	0.001	0.001
Zn	0.011	0.000	0.000	0.000	0.007	0.001	0.011	0.000	0.008	0.000	0.002	0.000	0.000	0.000	0.000	0.000	0.000	0.000	0.009	0.000	0.000	0.000
Mg	2.997	2.793	2.733	3.065	3.382	2.950	2.978	2.810	2.850	2.799	2.925	2.909	2.933	2.958	2.981	3.265	3.283	2.876	2.949	3.064	2.922	2.721
Ca	0.005	0.003	0.000	0.000	0.001	0.000	0.000	0.003	0.003	0.001	0.006	0.005	0.000	0.001	0.000	0.000	0.000	0.000	0.005	0.000	0.000	0.003
Na	0.002	0.007	0.000	0.007	0.000	0.005	0.000	0.000	0.000	0.000	0.000	0.000	0.019	0.007	0.014	0.000	0.000	0.005	0.005	0.000	0.000	0.019
K	0.000	0.000	0.000	0.000	0.000	0.000	0.000	0.000	0.000	0.000	0.000	0.000	0.000	0.000	0.000	0.000	0.000	0.000	0.000	0.000	0.000	0.000
total	13.976	14.008	13.992	14.053	13.998	14.048	14.013	14.102	14.006	13.972	14.003	14.011	14.072	14.084	14.077	14.042	14.072	14.015	14.071	14.025	14.006	14.021
Xmg	0.81	0.76	0.77	0.83	0.93	0.79	0.83	0.71	0.79	0.77	0.80	0.80	0.77	0.77	0.78	0.85	0.86	0.77	0.76	0.81	0.80	0.73

* total Fe as FeO

mineral											Orthopyroxene											
sample	TH961-22709	TH970-10610	TH970-10615	TH970-10807	TH970-11305	TH970-11607	TH970-11707	TH970-11709	TH970-12013	TH970-12803	TH970-12902	TH970-12903	TH970-20414	TH970-20415	TH970-20421	TH970-20427	TH970-20713	TH970-21105	TH970-21311	TH970-21326	TH970-21406	R9802-2301A	R9802-2301D
point	106	20	67	10	149	24	176	105	158	23	32	109	31	41	80	8	9	26	28	71	97	13	121
wt %																							
SiO2	49.74	49.06	49.06	51.70	49.38	50.27	48.50	49.78	48.85	47.43	49.23	49.70	48.71	48.18	50.22	49.66	48.74	47.80	49.39	49.35	49.17	50.66	48.60
TiO2	0.15	0.07	0.00	0.10	0.08	0.11	0.16	0.12	0.12	0.07	0.15	0.07	0.02	0.05	0.20	0.09	0.46	0.09	0.05	0.08	0.12	0.21	0.25
Al2O3	10.29	10.18	10.49	1.24	10.15	11.46	10.42	10.19	10.88	8.75	11.00	10.27	9.04	9.65	10.76	11.00	11.90	10.78	7.92	11.44	11.58	5.49	9.70
Cr2O3	0.00	0.03	0.00	0.00	0.00	0.00	0.00	0.03	0.02	0.00	0.00	0.28				0.00	0.00	0.00	0.03	0.00	0.00	0.00	0.00
FeO*	14.66	17.87	18.55	30.68	15.20	12.19	19.75	16.45	17.32	19.94	16.16	16.41	18.01	16.58	11.74	11.55	15.49	18.20	21.19	14.29	15.15	22.49	20.05
MnO	0.17	0.35	0.32	0.35	0.24	0.08	0.05	0.05	0.00	0.10	0.11	0.06	0.03	0.12	0.01	0.01	0.10	0.26	0.16	0.00	0.09	0.09	0.00
ZnO	0.00	0.10	0.03	0.01	0.00	0.13	0.00	0.00	0.02	0.01	0.00	0.00					0.01	0.00	0.05	0.13	0.00	0.03	0.10
MgO	25.26	23.06	22.41	16.88	24.75	26.22	21.87	23.65	23.18	21.53	23.60	23.36	24.14	24.32	27.84	28.00	24.15	23.71	21.40	25.43	24.90	21.17	21.53
CaO	0.02	0.03	0.01	0.49	0.02	0.04	0.01	0.02	0.05	0.03	0.05	0.08	0.04	0.01	0.06	0.07	0.04	0.01	0.06	0.00	0.01	0.13	0.02
Na2O	0.02	0.02	0.01	0.01	0.03	0.00	0.01	0.33	0.04	0.09	0.03	0.04	0.01	0.00	0.02	0.01	0.03	0.00	0.03	0.03	0.02	0.01	0.00
K2O	0.00	0.00	0.00	0.00	0.00	0.00	0.00	0.00	0.00	0.00	0.00	0.00	0.00	0.00	0.00	0.00	0.00	0.00	0.00	0.00	0.00	0.00	0.00
total	100.31	100.77	100.88	101.46	99.85	100.50	100.77	100.62	100.48	97.94	100.32	100.27	100.00	98.91	100.85	100.39	100.92	100.85	100.28	100.75	101.04	100.28	100.25
cations (O=6)																							
Si	1.777	1.773	1.774	1.971	1.778	1.770	1.765	1.787	1.763	1.785	1.769	1.789	1.776	1.766	1.760	1.749	1.737	1.732	1.820	1.752	1.747	1.877	1.781
Ti	0.004	0.002	0.000	0.003	0.002	0.003	0.004	0.003	0.003	0.002	0.004	0.002	0.001	0.001	0.005	0.002	0.012	0.002	0.001	0.002	0.003	0.006	0.007
Al	0.433	0.434	0.447	0.056	0.430	0.475	0.447	0.431	0.463	0.388	0.466	0.436	0.388	0.417	0.444	0.456	0.500	0.460	0.344	0.479	0.485	0.240	0.419
Cr	0.000	0.001	0.000	0.000	0.000	0.000	0.000	0.001	0.001	0.000	0.000	0.008	0.000	0.000	0.000	0.000	0.000	0.000	0.001	0.000	0.000	0.000	0.000
Fe	0.438	0.540	0.561	0.978	0.458	0.359	0.601	0.494	0.523	0.627	0.486	0.494	0.549	0.508	0.344	0.340	0.462	0.551	0.653	0.424	0.450	0.697	0.615
Mn	0.005	0.011	0.010	0.011	0.007	0.002	0.002	0.002	0.000	0.003	0.003	0.002	0.001	0.004	0.000	0.000	0.003	0.008	0.005	0.000	0.003	0.003	0.000
Zn	0.000	0.003	0.001	0.000	0.000	0.003	0.000	0.000	0.001	0.000	0.000	0.000	0.000	0.000	0.000	0.000	0.000	0.000	0.001	0.003	0.000	0.001	0.003
Mg	1.345	1.343	1.208	0.959	1.328	1.376	1.187	1.265	1.247	1.207	1.264	1.253	1.312	1.329	1.455	1.470	1.283	1.281	1.176	1.346	1.319	1.169	1.177
Ca	0.001	0.001	0.000	0.020	0.001	0.002	0.000	0.001	0.002	0.001	0.002	0.003	0.002	0.000	0.002	0.003	0.002	0.000	0.002	0.000	0.000	0.005	0.001
Na	0.001	0.001	0.001	0.001	0.002	0.000	0.001	0.023	0.003	0.007	0.001	0.003	0.001	0.000	0.001	0.001	0.002	0.000	0.002	0.002	0.001	0.001	0.000
K	0.000	0.000	0.000	0.000	0.000	0.000	0.000	0.000	0.000	0.000	0.000	0.000	0.000	0.000	0.000	0.000	0.000	0.000	0.000	0.000	0.000	0.000	0.000
total	4.004	4.009	4.002	3.999	4.006	3.990	4.007	4.007	4.006	4.020	3.995	3.990	4.030	4.025	4.011	4.021	4.001	4.034	4.005	4.008	4.008	3.999	4.003
Xmg	0.75	0.70	0.68	0.50	0.74	0.79	0.66	0.72	0.71	0.66	0.72	0.72	0.71	0.72	0.81	0.81	0.74	0.70	0.64	0.76	0.75	0.63	0.66

* total Fe as FeO

Table 3.2 (Continue)

mineral	Garnet													
sample	TH970-10516	TH970-10615	TH970-11709	TH970-12006	TH970-12013	TH970-12803	TH970-12902	TH970-12903	TH970-20416	TH970-20516	TH970-20518	TH970-21321	R9802-2301A	R9802-2301B
point	3	79	36	19	126	26	12	130	37	16	23	108	26	48
wt %														
SiO2	38.95	40.55	40.95	38.38	40.89	38.51	40.55	40.89	40.29	37.31	39.10	39.54	38.82	40.24
TiO2	0.00	0.01	0.01	0.02	0.06	0.02	0.01	0.02	0.00	0.00	0.06	0.01	0.00	0.03
Al2O3	22.03	22.51	23.03	21.62	23.44	22.11	23.20	23.14	22.91	21.39	22.48	23.11	22.25	22.84
Cr2O3	0.02	0.04	0.00	0.00	0.01	0.01	0.02	0.01	0.00	0.00	0.00	0.00	0.06	0.07
FeO*	26.85	24.03	22.80	31.05	23.15	23.34	21.36	22.89	21.36	31.25	22.47	27.38	28.10	25.44
MnO	0.32	1.12	0.27	0.42	0.06	0.32	0.43	0.31	0.19	0.37	0.11	0.29	0.25	0.13
ZnO		0.11	0.00		0.05	0.00	0.00	0.00		0.01	0.13	0.08	0.06	0.00
MgO	9.83	12.55	13.94	4.38	13.60	12.05	14.55	13.45	14.29	6.21	13.41	10.40	9.22	11.87
CaO	1.48	0.44	0.62	4.79	0.59	0.37	0.94	0.97	0.89	1.55	0.55	1.38	1.62	0.77
Na2O	0.00	0.00	0.09	0.04	0.03	0.00	0.00	0.01	0.01	0.08	0.12	0.01	0.01	0.00
K2O	0.00	0.00	0.00	0.00	0.00	0.00	0.00	0.00	0.00	0.00	0.00	0.00	0.00	0.00
total	99.48	101.36	101.71	100.70	101.88	96.73	101.06	101.69	99.94	98.17	98.43	102.20	100.39	101.39
cations (O=12)														
Si	2.999	3.018	3.006	3.010	2.997	2.994	2.984	3.006	2.996	2.986	2.975	2.962	2.981	3.001
Ti	0.000	0.001	0.001	0.001	0.003	0.001	0.001	0.001	0.000	0.000	0.003	0.001	0.000	0.002
Al	1.999	1.974	1.993	1.998	2.025	2.026	2.012	2.005	2.008	2.018	2.016	2.040	2.013	2.008
Cr	0.001	0.002	0.000	0.000	0.001	0.001	0.001	0.001	0.000	0.000	0.000	0.000	0.004	0.004
Fe	1.729	1.495	1.400	2.036	1.419	1.517	1.314	1.407	1.328	2.092	1.430	1.715	1.804	1.587
Mn	0.021	0.071	0.017	0.028	0.004	0.021	0.027	0.019	0.012	0.025	0.007	0.018	0.016	0.008
Zn	0.000	0.006	0.000	0.000	0.003	0.000	0.000	0.000	0.000	0.001	0.007	0.004	0.003	0.000
Mg	1.129	1.392	1.526	0.512	1.486	1.397	1.596	1.474	1.584	0.741	1.521	1.161	1.055	1.320
Ca	0.122	0.035	0.049	0.402	0.046	0.031	0.074	0.076	0.071	0.133	0.045	0.111	0.133	0.062
Na	0.000	0.000	0.013	0.006	0.004	0.000	0.000	0.001	0.001	0.012	0.018	0.001	0.001	0.000
K	0.000	0.000	0.000	0.000	0.000	0.000	0.000	0.000	0.000	0.000	0.000	0.000	0.000	0.000
total	8.000	7.994	8.005	7.993	7.988	7.988	8.009	7.990	8.000	8.008	8.022	8.013	8.010	7.992
Xmg	0.40	0.48	0.52	0.20	0.51	0.48	0.55	0.51	0.54	0.26	0.52	0.40	0.37	0.45
alm	0.58	0.50	0.47	0.68	0.48	0.51	0.44	0.47	0.44	0.70	0.48	0.57	0.60	0.53
prp	0.38	0.47	0.51	0.17	0.50	0.47	0.53	0.50	0.53	0.25	0.51	0.39	0.35	0.44
grs	0.04	0.01	0.02	0.13	0.02	0.01	0.02	0.03	0.02	0.04	0.01	0.04	0.04	0.02
sps	0.01	0.02	0.01	0.01	0.00	0.01	0.01	0.01	0.00	0.01	0.00	0.01	0.01	0.00

* total Fe as FeO

mineral	Omphacite										
sample	TH970-11305	TH970-11607	TH970-11707	TH970-11709	TH970-12013	TH970-12803	TH970-20414	TH970-20415	TH970-20427	TH970-21326	TH970-21406
point	161	5	177	114	135	28	39	53	76	58	78
wt %											
SiO2	61.93	62.45	62.11	62.31	62.44	59.93	61.25	60.47	62.68	62.59	62.20
TiO2	0.06	0.03	0.08	0.06	0.13	0.03	0.09	0.44	0.00	0.02	0.04
Al2O3	23.40	23.40	23.26	23.26	22.78	23.59	23.28	22.86	23.29	23.68	23.65
Cr2O3	0.01	0.00	0.00	0.00	0.01	0.00			0.00	0.00	0.03
FeO*	1.56	1.25	2.44	2.25	1.85	1.79	2.18	1.66	1.13	1.41	1.61
MnO	0.10	0.10	0.02	0.00	0.00	0.06	0.02	0.02	0.04	0.04	0.00
ZnO	0.11	0.21	0.00	0.00	0.01	0.09				0.07	0.04
MgO	8.42	8.20	7.73	7.65	8.33	7.76	8.22	8.33	8.97	8.15	8.11
CaO	0.00	0.01	0.05	0.01	0.00	0.01	0.00	0.02	0.00	0.00	0.00
Na2O	0.27	0.27	0.22	0.34	0.22	0.29	0.36	0.26	0.19	0.35	0.28
K2O	4.34	4.06	4.29	4.51	4.49	4.23	4.52	4.52	4.47	4.16	4.36
total	100.20	99.98	100.20	100.39	100.26	97.78	99.92	98.58	100.77	100.47	100.32
cations (O=30)											
Si	10.187	10.256	10.236	10.252	10.269	10.109	10.145	10.135	10.224	10.234	10.207
Ti	0.007	0.004	0.010	0.007	0.016	0.004	0.011	0.055	0.000	0.002	0.005
Al	4.535	4.529	4.517	4.510	4.415	4.689	4.544	4.515	4.477	4.563	4.574
Cr	0.001	0.000	0.000	0.000	0.001	0.000	0.000	0.000	0.000	0.000	0.003
Fe	0.215	0.172	0.336	0.310	0.254	0.252	0.302	0.233	0.154	0.193	0.221
Mn	0.014	0.014	0.003	0.000	0.000	0.009	0.003	0.003	0.006	0.006	0.000
Zn	0.013	0.025	0.000	0.000	0.001	0.011	0.000	0.000	0.000	0.008	0.005
Mg	2.065	2.008	1.899	1.876	2.042	1.951	2.050	2.081	2.181	1.987	1.983
Ca	0.000	0.002	0.009	0.002	0.000	0.002	0.000	0.004	0.000	0.000	0.000
Na	0.086	0.086	0.070	0.108	0.070	0.095	0.116	0.084	0.060	0.111	0.089
K	0.911	0.850	0.902	0.947	0.942	0.910	0.955	0.966	0.930	0.867	0.913
total	18.034	17.946	17.982	18.012	18.010	18.032	18.106	18.076	18.032	17.971	18.000
Xmg	0.91	0.92	0.85	0.86	0.89	0.89	0.87	0.90	0.93	0.91	0.90

* total Fe as FeO

mineral	Spinel					
sample	TH970-10615	TH970-11709	TH970-12903	TH970-20416	TH970-21105	TH970-21321
point	61	57	104	9	33	59
wt %						
SiO2	0.21	0.00	0.04	0.00	0.00	0.17
TiO2	0.00	0.00	0.03	0.10	0.03	0.01
Al2O3	62.93	63.46	59.94	64.57	61.69	58.15
Cr2O3	0.55	0.00	4.10	0.04	0.25	4.93
FeO*	21.35	22.63	22.52	16.45	27.47	21.34
MnO	0.11	0.00	0.08	0.06	0.21	0.00
ZnO	4.77	0.90	2.27		0.14	6.00
MgO	9.96	12.69	11.65	16.83	10.81	9.61
CaO	0.02	0.00	0.01	0.00	0.02	0.02
Na2O	0.16	0.07	0.07	0.00	0.00	
K2O	0.00	0.00	0.00	0.00	0.00	0.00
total	100.06	99.75	100.71	98.05	100.62	100.23
cations (O=4)						
Si	0.006	0.000	0.001	0.000	0.000	0.005
Ti	0.000	0.000	0.001	0.002	0.001	0.000
Al	1.994	1.984	1.897	1.986	1.955	1.883
Cr	0.012	0.000	0.087	0.001	0.005	0.107
Fe	0.480	0.502	0.506	0.359	0.618	0.490
Mn	0.003	0.000	0.002	0.001	0.005	0.000
Zn	0.095	0.018	0.045	0.000	0.003	0.122
Mg	0.399	0.502	0.466	0.655	0.433	0.394
Ca	0.001	0.000	0.000	0.000	0.001	0.001
Na	0.008	0.004	0.004	0.000	0.000	0.000
K	0.000	0.000	0.000	0.000	0.000	0.000
total	2.998	3.010	3.009	3.004	3.021	3.002
Xmg	0.45	0.50	0.48	0.65	0.41	0.45

* total Fe as FeO

Table 3.2 (Continue)

mineral	Plagioclase																							
sample	TH961-22709	TH970-10807	TH970-10516	TH970-10610	TH970-10615	TH970-10705	TH970-10820	TH970-11305	TH970-11709	TH970-12006	TH970-12015	TH970-12803	TH970-20415	TH970-20416	TH970-20421	TH970-20515	TH970-20516	TH970-20518	TH970-20713	TH970-21105	TH970-21321	R9402-2301A	R9402-2301B	R9402-2301D
point	113	20	26	3-2	72	2-24	9	128	67	4	134	2	15	6	17	17	11	21	45	20	237	42	2	71
wt %																								
SiO2	66.02	58.53	55.84	66.19	67.40	65.53	63.86	60.75	61.91	61.30	63.77	68.04	60.18	60.99	66.52	61.55	61.03	60.95	66.57	68.22	58.54	59.11	62.59	61.69
TiO2	0.12	0.03	0.06	0.08	0.14	0.05	0.05	0.04	0.01	0.01	0.00	0.06	0.04	0.06	0.06	0.15	0.00	0.09	0.13	0.01	0.00	0.00	0.16	0.05
Al2O3	21.65	26.50	26.96	19.96	21.14	21.21	23.25	24.86	24.05	24.58	23.04	19.43	24.45	24.72	20.45	24.08	24.27	23.72	21.07	20.00	26.64	25.57	24.48	23.94
Cr2O3	0.00	0.00	0.09	0.00	0.00	0.02	0.00	0.00	0.00	0.05	0.00	0.01		0.00		0.02	0.01	0.05	0.03	0.00	0.04	0.05	0.04	0.01
FeO*	0.04	0.01	0.08	0.02	0.00	0.05	0.10	0.00	0.02	0.00	0.00	0.06	0.00	0.06	0.33	0.02	0.00	0.03	0.09	0.04	0.00	0.00	0.00	0.21
MnO	0.03	0.02	0.00	0.07	0.00	0.00	0.01	0.00	0.00	0.00	0.00	0.08	0.00	0.00	0.00	0.02	0.04	0.00	0.00	0.04	0.03	0.01	0.00	0.00
MgO	0.00	0.01	0.00	0.00	0.01	0.01	0.03	0.01	0.16	0.05	0.00	0.04	0.00	0.00	0.00	0.03	0.00	0.00	0.00	0.00	0.00	0.00	0.01	0.00
CaO	2.18	7.50	9.58	1.29	1.64	2.15	3.94	6.40	5.27	6.03	4.60	0.40	5.86	5.82	1.36	5.57	5.78	5.13	1.81	0.94	8.27	7.69	5.45	5.31
Na2O	10.29	7.06	7.13	11.10	10.83	10.24	9.17	7.96	8.23	8.08	9.01	9.53	9.00	10.18	11.10	8.75	8.72	8.66	10.09	11.20	6.93	7.03	8.52	8.42
K2O	0.24	0.19	0.05	0.25	0.24	0.13	0.05	0.17	0.37	0.15	0.16	2.21	0.13	0.11	0.07	0.10	0.08	0.12	0.58	0.18	0.13	0.26	0.17	0.16
BaO		0.00				0.05	0.04			0.09		0.00				0.12	0.00	0.11			0.00			
total	100.57	99.85	99.81	98.96	101.40	99.44	100.50	100.19	100.01	100.33	100.58	99.88	99.66	101.94	99.89	100.41	99.93	98.86	100.37	100.63	100.60	99.72	101.42	99.79
cations (O=8)																								
Si	2.886	2.616	2.527	2.939	2.916	2.894	2.798	2.697	2.744	2.712	2.805	2.995	2.694	2.681	2.927	2.725	2.713	2.735	2.913	2.968	2.598	2.646	2.757	2.743
Ti	0.004	0.001	0.002	0.003	0.005	0.002	0.002	0.001	0.000	0.000	0.000	0.002	0.001	0.002	0.002	0.005	0.000	0.003	0.004	0.000	0.000	0.000	0.005	0.002
Al	1.115	1.396	1.438	1.045	1.078	1.104	1.200	1.301	1.256	1.282	1.195	1.008	1.290	1.281	1.060	1.256	1.272	1.255	1.087	1.026	1.393	1.349	1.261	1.254
Fe	0.000	0.000	0.003	0.001	0.000	0.001	0.000	0.000	0.000	0.002	0.000	0.000	0.000	0.002	0.012	0.001	0.000	0.002	0.001	0.000	0.001	0.002	0.001	0.000
Mn	0.001	0.000	0.000	0.003	0.000	0.002	0.004	0.000	0.001	0.000	0.000	0.002	0.000	0.000	0.000	0.001	0.000	0.001	0.003	0.001	0.000	0.000	0.000	0.000
Mg	0.000	0.001	0.000	0.000	0.001	0.001	0.000	0.001	0.011	0.002	0.000	0.000	0.000	0.000	0.000	0.000	0.001	0.004	0.000	0.000	0.000	0.000	0.001	0.000
Ca	0.102	0.359	0.465	0.061	0.076	0.102	0.185	0.304	0.250	0.286	0.217	0.019	0.281	0.274	0.064	0.264	0.275	0.247	0.085	0.044	0.393	0.369	0.255	0.253
Na	0.872	0.612	0.627	0.956	0.909	0.877	0.779	0.685	0.707	0.695	0.768	0.813	0.781	0.868	0.947	0.751	0.752	0.753	0.856	0.945	0.596	0.610	0.722	0.716
K	0.013	0.011	0.005	0.014	0.013	0.007	0.003	0.010	0.021	0.008	0.009	0.124	0.007	0.006	0.004	0.006	0.005	0.007	0.032	0.010	0.008	0.015	0.009	0.009
Ba	0.000	0.000	0.003	0.000	0.000	0.001	0.001	0.000	0.000	0.002	0.000	0.000	0.000	0.000	0.000	0.002	0.000	0.002	0.000	0.000	0.000	0.000	0.000	0.000
total	4.993	4.996	5.068	5.022	4.998	4.991	4.972	4.999	4.990	4.987	4.990	4.961	5.054	5.114	5.016	5.011	5.018	5.009	4.981	4.994	4.989	4.991	4.991	4.995
an	0.105	0.366	0.424	0.060	0.076	0.103	0.191	0.305	0.256	0.289	0.218	0.020	0.263	0.239	0.063	0.259	0.267	0.245	0.087	0.044	0.394	0.371	0.259	0.256
ab	0.883	0.623	0.573	0.937	0.911	0.889	0.806	0.686	0.723	0.702	0.775	0.851	0.730	0.756	0.933	0.736	0.729	0.748	0.880	0.946	0.597	0.614	0.732	0.725
or	0.014	0.011	0.003	0.014	0.013	0.007	0.003	0.010	0.021	0.009	0.009	0.130	0.007	0.005	0.004	0.006	0.004	0.007	0.033	0.010	0.009	0.015	0.010	0.009

* total Fe as FeO

mineral	Alkali feldspar																							
sample	TH970-10807	TH970-10615	TH970-10705	TH970-11505	TH970-11709	TH970-12006	TH970-12013	TH970-12803	TH970-12902	TH970-20415	TH970-20416	TH970-20421	TH970-20427	TH970-20515	TH970-20516	TH970-20518	TH970-20713	TH970-21105	TH970-21321	R9402-2301A	R9402-2301B	R9402-2301D
point	22	89	7	3	54	5	133	18	8	30	22	14	42	2	1	18	19	6	37	29	45	41
wt %																						
SiO2	64.36	64.63	64.75	64.34	65.14	64.50	65.23	63.67	64.39	63.85	64.76	64.19	65.43	64.06	64.19	64.62	64.88	64.60	63.98	64.67	65.07	64.64
TiO2	0.00	0.04	0.09	0.02	0.08	0.00	0.06	0.02	0.06	0.05	0.03	0.18	0.01	0.16	0.02	0.10	0.11	0.05	0.12	0.05	0.09	0.09
Al2O3	18.56	18.42	17.90	18.60	18.58	18.81	18.91	18.26	18.57	18.42	19.80	18.46	18.53	18.62	18.44	18.71	20.11	19.68	18.82	18.57	18.68	18.75
Cr2O3	0.04	0.04	0.00	0.00	0.00	0.00	0.00	0.04	0.00		0.00		0.00	0.00	0.00	0.00	0.04	0.00	0.00	0.00	0.01	0.00
FeO*	0.04	0.00	0.13	0.07	0.33	0.03	0.25	0.00	0.00	0.03	0.03	0.05	0.02	0.00	0.02	0.00	0.06	0.25	0.01	0.00	0.00	0.00
MnO	0.01	0.05	0.07	0.00	0.02	0.00	0.00	0.00	0.00	0.06	0.01	0.00	0.02	0.00	0.04	0.05	0.07	0.00	0.00	0.07	0.04	0.00
MgO	0.00	0.02	0.00	0.37	0.00	0.00	0.00	0.00	0.00	0.00	0.01	0.00	0.02	0.02	0.01	0.01	0.00	0.00	0.00	0.00	0.00	0.00
CaO	0.08	0.05	0.00	0.04	0.07	0.02	0.12	0.12	0.15	0.28	1.12	0.00	0.04	0.04	0.17	0.36	1.92	0.95	0.14	0.09	0.30	0.35
Na2O	0.48	0.84	1.00	0.78	1.53	0.96	1.25	1.13	1.42	1.18	3.32	0.95	1.45	1.00	1.58	1.91	3.12	4.16	0.41	0.38	1.61	1.59
K2O	15.83	15.40	15.30	15.35	14.36	15.97	15.05	14.77	14.55	15.24	10.86	16.08	15.05	15.55	14.35	13.45	10.05	10.83	15.70	16.40	13.77	14.55
BaO	0.95			0.07		0.10		0.17					0.03	0.10	0.09	0.04	0.14		1.00		0.36	
total	100.33	99.53	99.24	99.64	100.01	100.39	100.87	98.18	99.14	99.11	99.94	99.89	100.58	99.55	98.91	99.23	100.50	100.52	100.18	100.23	99.93	99.97
cations (O=8)																						
Si	2.980	2.993	3.009	2.977	2.992	2.972	2.978	2.988	2.986	2.977	2.944	2.977	2.996	2.971	2.985	2.978	2.930	2.933	2.965	2.986	2.988	2.976
Ti	0.000	0.001	0.003	0.001	0.003	0.000	0.002	0.001	0.002	0.002	0.001	0.006	0.000	0.006	0.001	0.003	0.004	0.002	0.004	0.002	0.003	0.003
Al	1.013	1.005	0.980	1.014	1.006	1.021	1.018	1.010	1.015	1.012	1.061	1.009	1.000	1.018	1.011	1.016	1.070	1.053	1.028	1.011	1.011	1.017
Fe	0.001	0.001	0.005	0.000	0.000	0.000	0.000	0.001	0.000	0.001	0.001	0.002	0.001	0.000	0.000	0.000	0.001	0.000	0.000	0.000	0.000	0.000
Mn	0.002	0.000	0.003	0.003	0.009	0.001	0.010	0.000	0.000	0.002	0.000	0.000	0.001	0.000	0.001	0.000	0.002	0.009	0.000	0.000	0.000	0.000
Mg	0.000	0.001	0.000	0.000	0.000	0.000	0.000	0.001	0.000	0.000	0.001	0.000	0.001	0.000	0.000	0.000	0.000	0.000	0.000	0.000	0.000	0.000
Ca	0.004	0.002	0.000	0.002	0.003	0.001	0.006	0.006	0.007	0.014	0.055	0.000	0.002	0.002	0.008	0.018	0.093	0.046	0.007	0.004	0.015	0.017
Na	0.043	0.079	0.090	0.070	0.136	0.085	0.111	0.103	0.127	0.107	0.295	0.084	0.129	0.090	0.142	0.171	0.275	0.366	0.037	0.034	0.143	0.142
K	0.955	0.910	0.907	0.906	0.841	0.959	0.877	0.864	0.861	0.906	0.630	0.951	0.878	0.910	0.851	0.789	0.579	0.627	0.928	0.966	0.807	0.855
Ba	0.017	0.000	0.000	0.001	0.000	0.002	0.000	0.003	0.000	0.000	0.000	0.000	0.000	0.002	0.002	0.001	0.002	0.000	0.018	0.000	0.006	0.000
total	4.995	4.992	4.997	4.974	4.990	5.021	5.002	4.997	4.998	5.021	4.986	5.029	5.008	5.009	5.001	4.976	4.954	5.036	4.987	5.003	4.973	5.010
an	0.004	0.003	0.000	0.002	0.004	0.001	0.006	0.006	0.007	0.014	0.056	0.000	0.002	0.002	0.008	0.018	0.098	0.044	0.007	0.004	0.015	0.017
ab	0.044	0.080	0.090	0.072	0.139	0.083	0.111	0.104	0.128	0.104	0.300	0.081	0.128	0.089	0.142	0.175	0.289	0.352	0.038	0.034	0.149	0.140
or	0.952	0.918	0.910	0.926	0.858	0.916	0.883	0.890	0.865	0.883	0.645	0.919	0.870	0.909	0.849	0.807	0.613	0.603	0.955	0.962	0.836	0.843

* total Fe as FeO

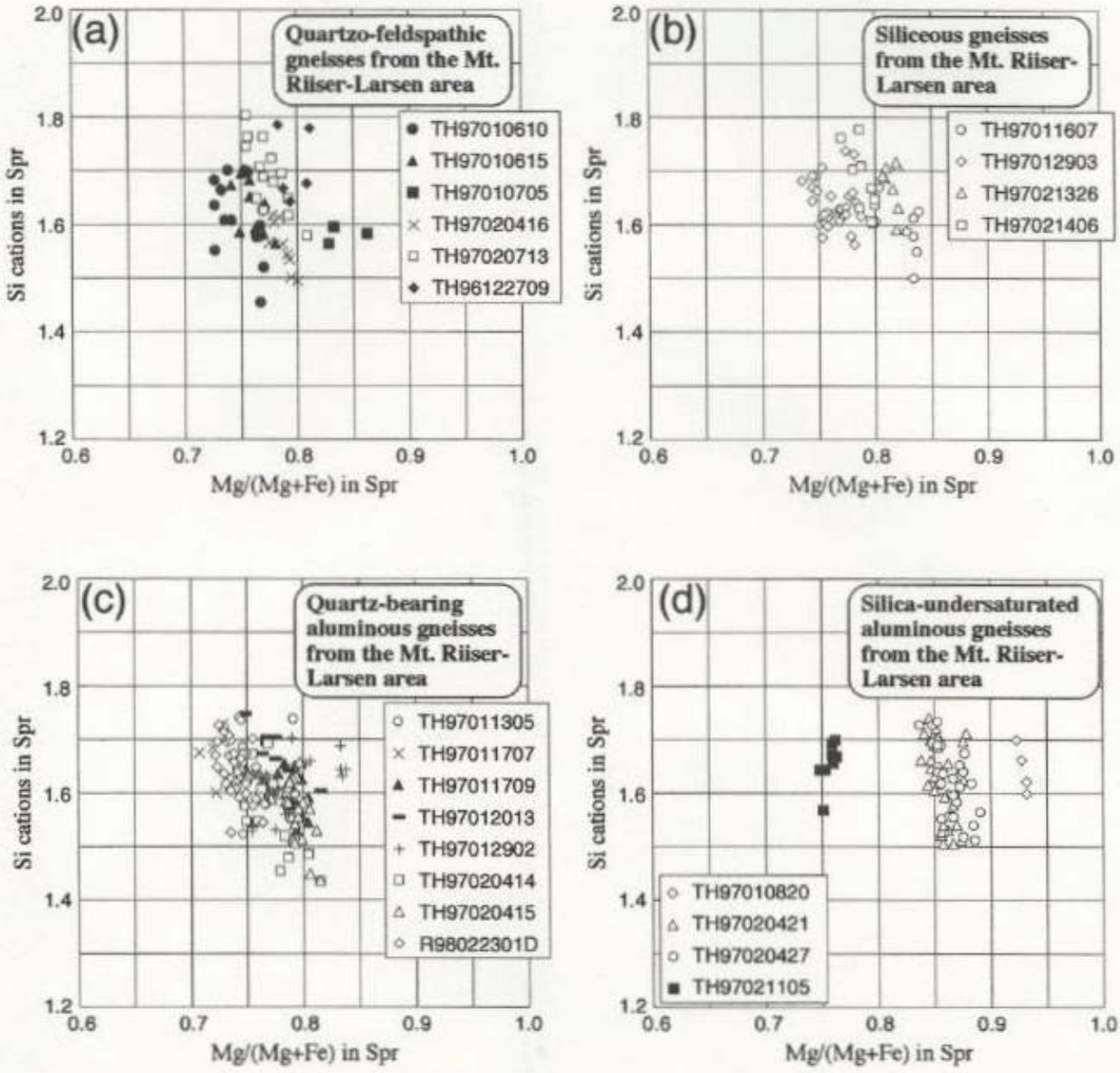

Fig.3.9 Sapphirine compositions in terms of X_{Mg} and Si cations per 20-oxygen formula unit. (a) Sapphirine from quartzo-feldspathic gneisses. (b) Sapphirine from siliceous gneisses. (c) Sapphirine from quartz-bearing aluminous gneisses. (d) Sapphirine from silica-undersaturated aluminous gneisses. Close symbols are samples from the western area, and others are those from the central area of the Mt. Riiser-Larsen.

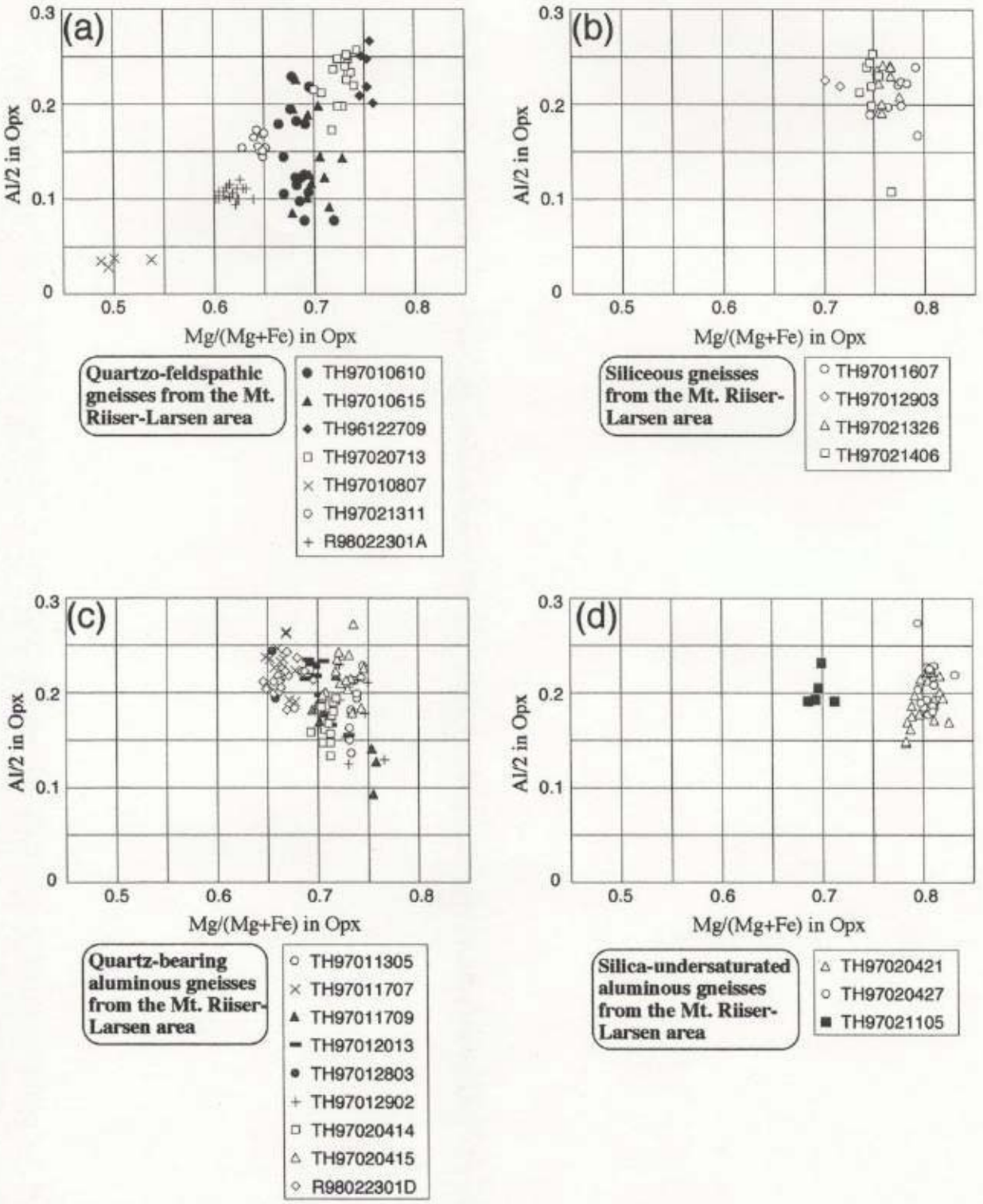

Fig. 3.10 Orthopyroxene compositions in terms of X_{Mg} and Al cations/2 per 6-oxygen formula unit. (a) Orthopyroxene from quartzo-feldspathic gneisses. (b) Orthopyroxene from siliceous gneisses. (c) Orthopyroxene from quartz-bearing aluminous gneisses. (d) Orthopyroxene from silica-undersaturated aluminous gneisses. Close symbols are samples from the western area, and others are those from the central area of the Mt. Riiser-Larsen.

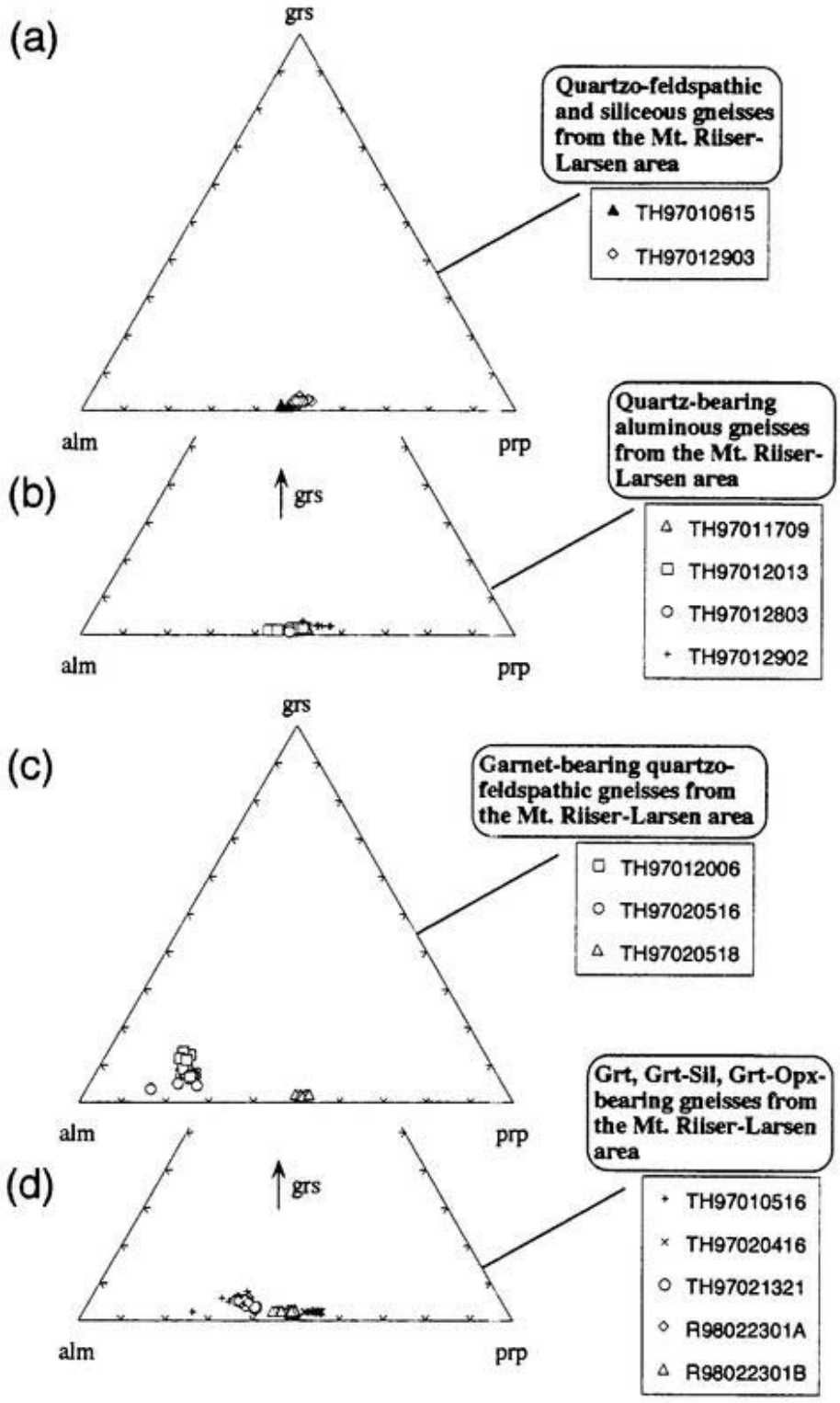

Fig.3.11 Grossular (grs)-almandine (alm)-pyrope (prp) plot of garnet compositions. (a) Garnet from quartzo-feldspathic and siliceous gneisses. (b) Garnet from quartz-bearing gneisses. (c) Garnet from garnet quartzo-feldspathic gneisses. (d) Garnet from garnet, garnet-sillimanite and garnet-orthopyroxene-bearing gneisses. Close symbols are samples from the western area, and others are those from the central area of the Mt. Riiser-Larsen.

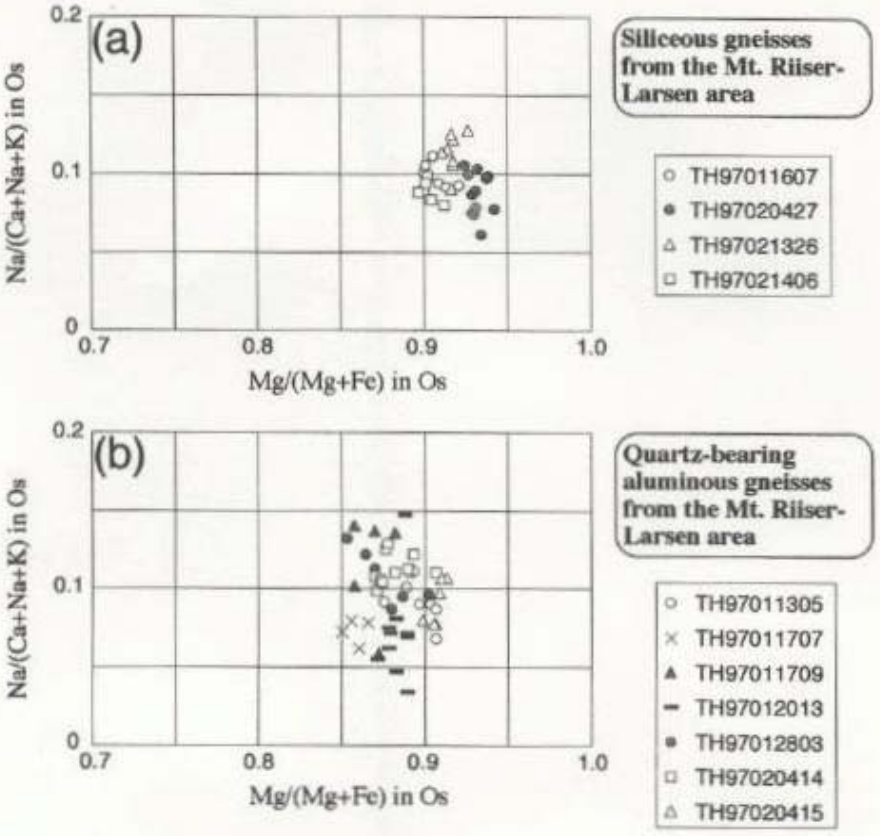

Fig.3.12 Osumilite compositions in terms of Mg/(Mg+Fe) ratios and Na/(Ca+Na+K) ratios. (a) Osumilite from siliceous gneisses. (b) Osumilite from quartz-bearing aluminous gneisses. All samples are from the central area of the Mt. Riiser-Larsen.

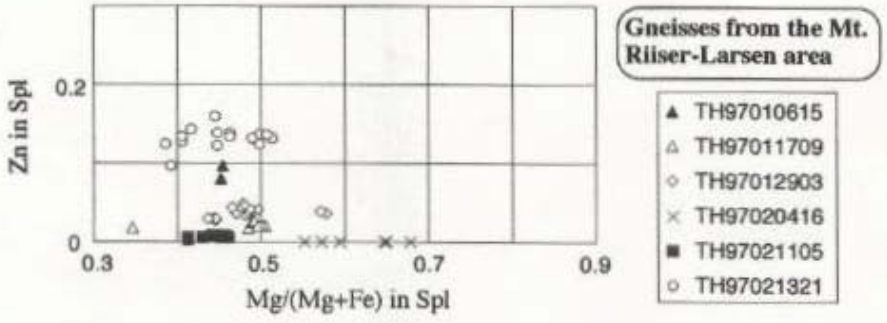

Fig.3.13 Spinel compositions in terms of Mg/(Mg+Fe) ratios and Zn cations per 4-oxygen formula unit. (a) Osumilite from siliceous gneisses. (b) Osumilite from quartz-bearing aluminous gneisses. Close symbols are samples from the western area, and others are those from the central area of the Mt. Riiser-Larsen.

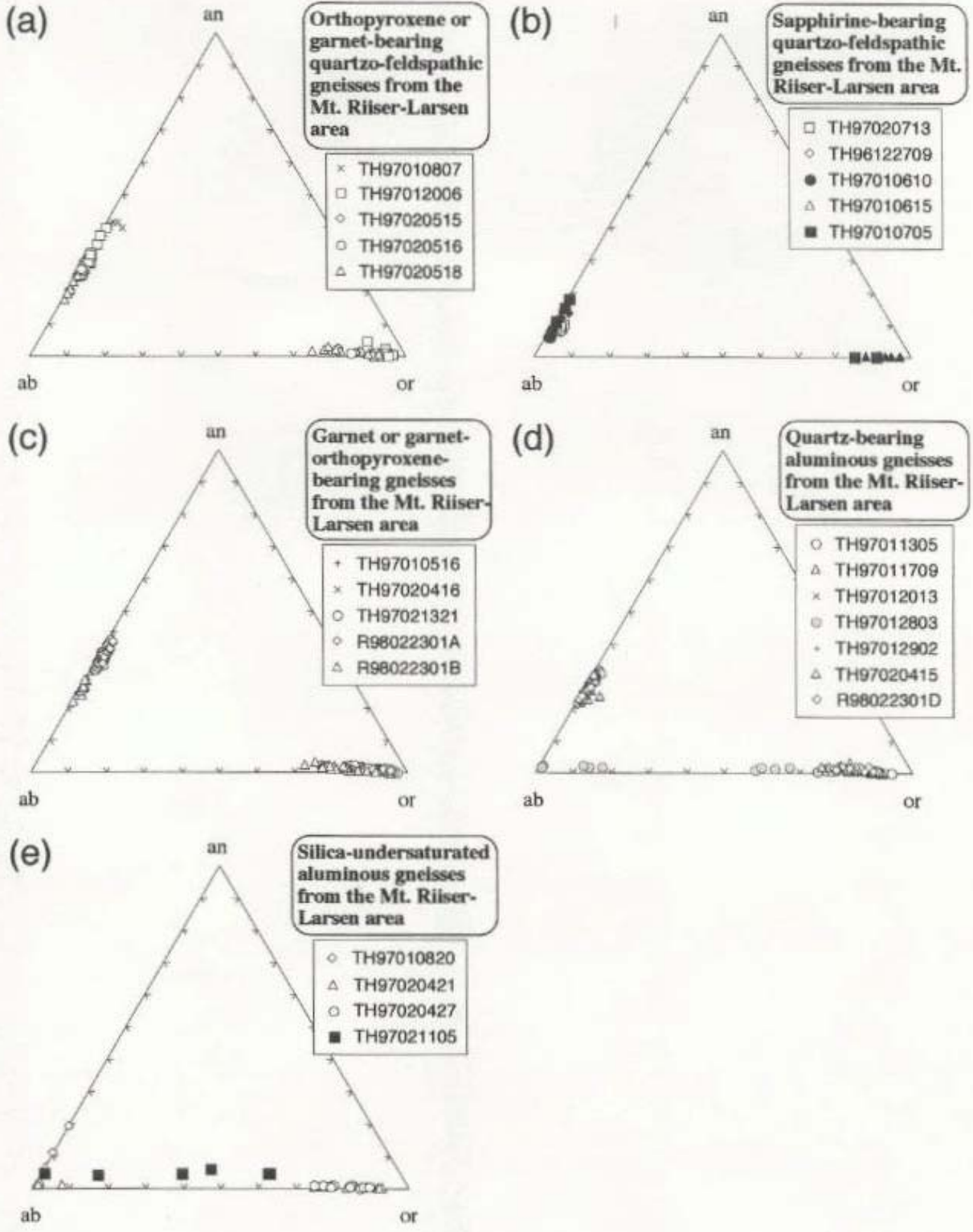

Fig.3.14 Anorthite (an)-Albite (ab)-orthoclase (or) plot of feldspar compositions. (a) Feldspar from orthopyroxene or garnet-bearing quartzo-feldspathic gneisses. (b) Feldspar from sapphirine-bearing quartzo-feldspathic gneisses. (c) Feldspar from garnet or garnet-orthopyroxene-bearing gneisses. (d) Feldspar from quartz-bearing aluminous gneisses. (e) Feldspar from silica-undersaturated aluminous gneisses. Close symbols are samples from the western area, and others are those from the central area of the Mt. Riiser-Larsen.

(e) Spinel

X_{Mg} of spinel is the lowest among that of other constituent minerals (Fig. 3.13), and varies with the change of minerals enclosing spinel. It ranges from 0.44 to 0.45 in quartz, from 0.47 to 0.50 in orthopyroxene and osumilite, and from 0.57 to 0.58 in garnet. 1.3 wt.% of ZnO is constitutes spinel in quartz, and 1.7 ~ 2.4 in orthopyroxene, osumilite and garnet.

(f) Cordierite

Cordierite is characterized by high X_{Mg} from 0.86 to 0.92. Total wt.% of the analyses indicates that cordierite is nearly anhydrous and contains H_2O less than 1 wt.%. It commonly display polysynthetic twin. Pleochroic halo is conspicuous around monazite inclusion in cordierite.

3.5. Discussion

3.5.1. Phase relations and peak P-T conditions

Phase equilibria in UHT conditions are discussed by theoretical thermodynamic calculations (Hensen, 1971; 1986; 1987; Ellis *et al.*, 1980; Grew, 1982; Holland *et al.*, 1996) and by high temperature synthetic experiments (Hensen and Green, 1971; 1972; 1973; Bertrand *et al.*, 1991; Motoyoshi *et al.*, 1993; Audibert *et al.*, 1995; Carrington and Harley, 1995a; 1995b), which are summarized in Fig. 3.15. Topology of petrogenetic grid and temperature of each reaction are almost consistent with synthetic experiments cited above. However, pressure condition is systematically deviated from each experiment, i.e., experimental results of Carrington and Harley (1995a; 1995b) (labeled 'CH95' in Fig. 3.15) are 0.2 GPa lower-pressures than those of Hensen & Green (1971; 1972; 1973), Motoyoshi *et al.* (1993) and Audibert *et al.* (1995) (labeled 'HG73,MHA93,AHB95' in Fig. 3.15), and is considered to be due to the difficulties of friction correction in the experiments (Carrington and Harley, 1995a). Carrington and Harley (1995a) performed cross-calibration experiments using both gas-media and solid-media apparatuses, and discussed that the experiments using only solid-media apparatus had considerably underestimated the required friction correction, thereby introducing a systematic error into their results. Therefore, the pressure conditions of Carrington and Harley (labeled 'CH95' in Fig. 3.15) is plausible.

Mineral parageneses of sapphirine + orthopyroxene + quartz, sapphirine + garnet + quartz and garnet + osumilite, which are observed from the

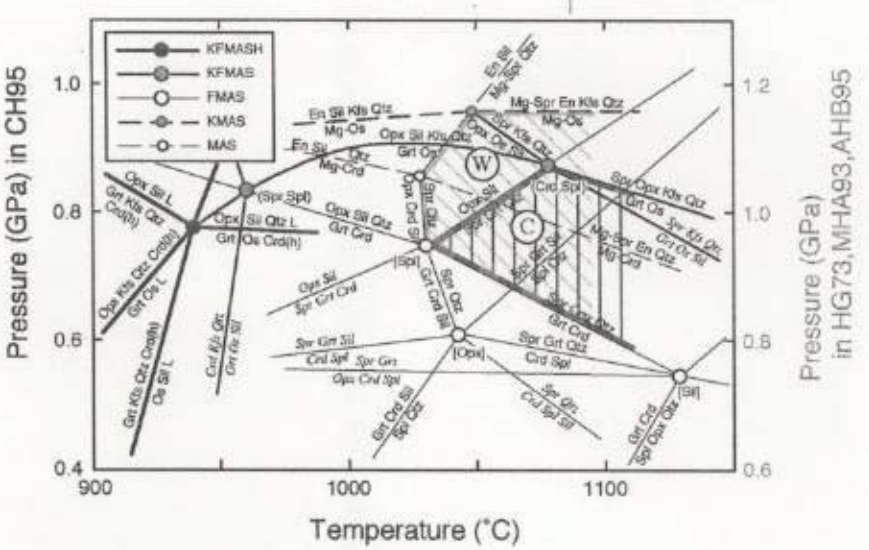

Fig.3.15 Univariant phase equilibria in UHT conditions, compiled after Hensen and Green (1973), Motoyoshi *et al.* (1993), Audibert *et al.* (1995) and Carrington and Harley (1995a, b). Pressure condition is modeified to match the experimental results of Carrington and Harley (1995a). See detail in the text. 'C' and 'W' are the peak P-T conditions constrained by the mineral parageneses for rocks of the central and the western areas of the Mt. Riiser-Larsen, respectively.

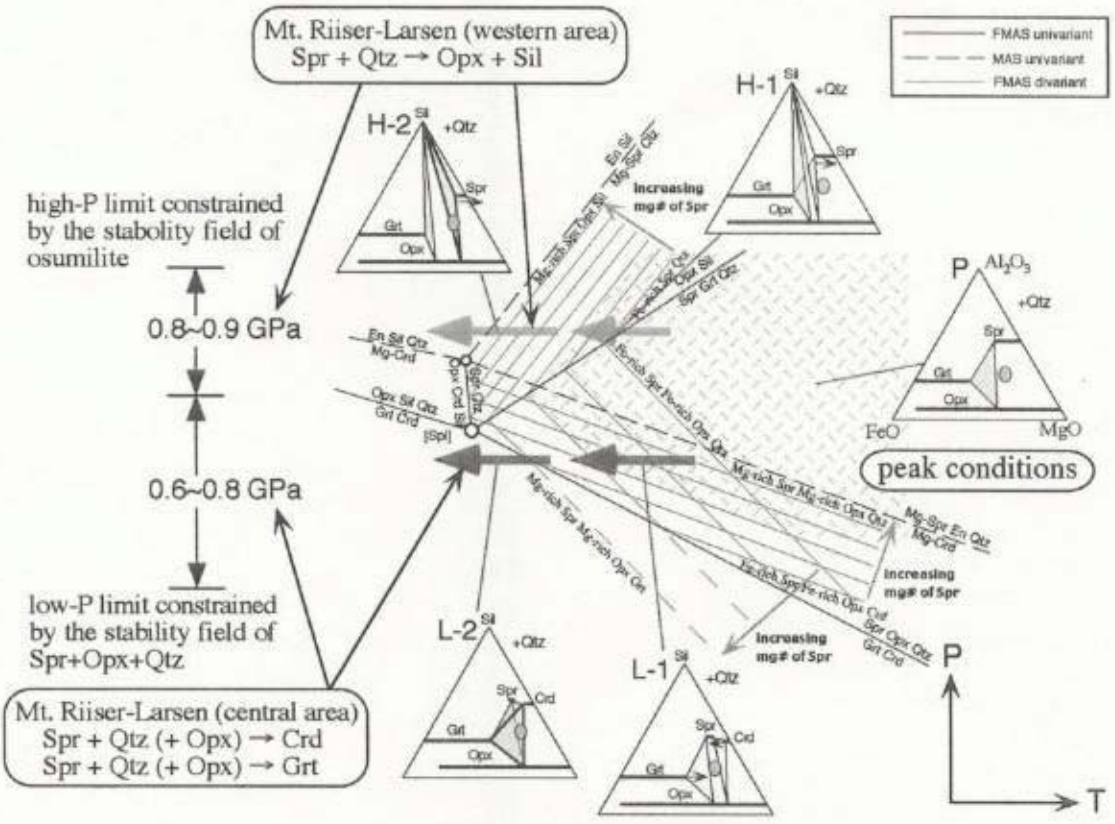

Fig.3.16 Schematic divariant phase equilibria superimposed upon the univariant curves in Fig. 3.15. Arrows indicate the shematic P-T trajectories deduced from two different types of reaction textures.

gneisses in the central area of the Mt. Riiser-Larsen, constrain the peak metamorphic conditions > 1040°C and 0.6 ~ 0.9 GPa. In the western area, where garnet + osumilite and sapphirine + garnet + quartz parageneses are not found, the occurrences of osumilite and sapphirine + orthopyroxene + quartz parageneses suggest the similar P-T or slightly lower-T / higher-P than the central area (>1030°C and 0.6~0.9 GPa).

3.5.2. Reaction textures after sapphirine + quartz

As described above, reaction textures after sapphirine + quartz are different between the central and the western areas. The reaction textures of thin cordierite and/or garnet films fill the grain boundary between sapphirine and quartz with or without orthopyroxene in the central area, and they imply the following reactions:

Spr + Qtz (+ Opx) -> Crd (1)
Spr + Qtz (+ Opx) -> Grt (2)

In contrast, secondary orthopyroxene and sillimanite is formed between sapphirine and quartz in the western area, and represents the following reaction:

Spr + Qtz -> Opx + Sil (3)

Schematic divariant phase equilibria for the FeO-MgO-Al_2O_3-SiO_2 system are qualitatively obtained from the mutual topological relationships of the univariant curves in Fig. 3.15, and are shown in Fig. 3.16. Stability field of the sapphirine-orthopyroxene-quartz mineral paragenesis in AFM diagram at the peak condition (labeled 'P' in Fig. 3.16) becomes narrow as the temperature decreasing, and stability field of orthopyroxene + sillimanite extends instead of sapphirine + quartz at higher-pressure (H-1 and H-2 in Fig. 3.16) and that of cordierite and garnet spreads at lower-pressure (L-1 and L-2 in Fig. 3.16).

The reactions (1) and (2) in the central part of the area occur at lower-pressures than the invariant point [Spl], and are explained as following divariant reactions:

Mg-rich Spr + Qtz + Mg-rich Opx = Fe-rich Spr + Fe-rich Opx + Crd (1')
Fe-rich Spr + Qtz + Fe-rich Opx = Mg-rich Spr + Mg-rich Opx + Grt (2')

Tschermak substitution in sapphirine and orthopyroxene is also responsible for the difference of the reaction textures whether orthopyroxene participates the reaction or not, but it is difficult to evaluate the change of tschermak component in sapphirine and orthopyroxene quantitatively during the reaction. For this reason, tschermak substitution is neglected in the above reaction equations for simplification.

The reaction (3) in the western area occurring at higher-pressures than the invariant point [Spl] is explained as following divariant reaction:

Fe-rich Spr + Qtz = Mg-rich Spr + Opx + Sil (3')

Fig. 3.17 illustrates X_{Mg} of the phases constituting the reaction textures. No systematic difference of X_{Mg} of sapphirine is detected between the different reaction textures. The above reactions occur at >1030°C, slightly lower temperatures than the peak temperatures, but still ultrahigh temperature conditions. These indicate that the cooling path and the possibly peak conditions of the central area of the Mt. Riiser-Larsen is lower-pressures than those of the western area. Harley (1985) proposed the near isobaric cooling path from the UHT conditions for rocks of the various localities in the Napier Complex using garnet-orthopyroxene geothermobarometry. Reaction textures discussed here is consistent with the isobaric cooling path of Harley (1985), and the Mt. Riiser-Larsen area should have experienced the isobaric cooling.

As mentioned in the description of geological outline, the central and the western areas of the Mt. Riiser-Larsen are divided by the shear zone of north-south strike and almost vertical dip. Interpretation discussed above and structural observation suggest that the western area represents deeper structural level than the central area and they have juxtaposed due to the subvertical movement along the shear zone after isobaric cooling.

3.5.3. *Implications for the regional metamorphic conditions*

Harley (1998) summarizes that the reaction textures after sapphirine + quartz are indicator for the pressure gradient during thermal peak, i.e., sapphirine + quartz rimmed by coronas involving combination of cordierite, sillimanite and garnet in the northern areas are lower pressures at cooling stage than those of sapphirine + quartz rimmed by orthopyroxene + sillimanite in the areas south of Amundsen Bay. This study shows that both these two different types of reaction textures are observed in the Mt. Riiser-Larsen area, and the rocks of the different structural level have juxtaposed due

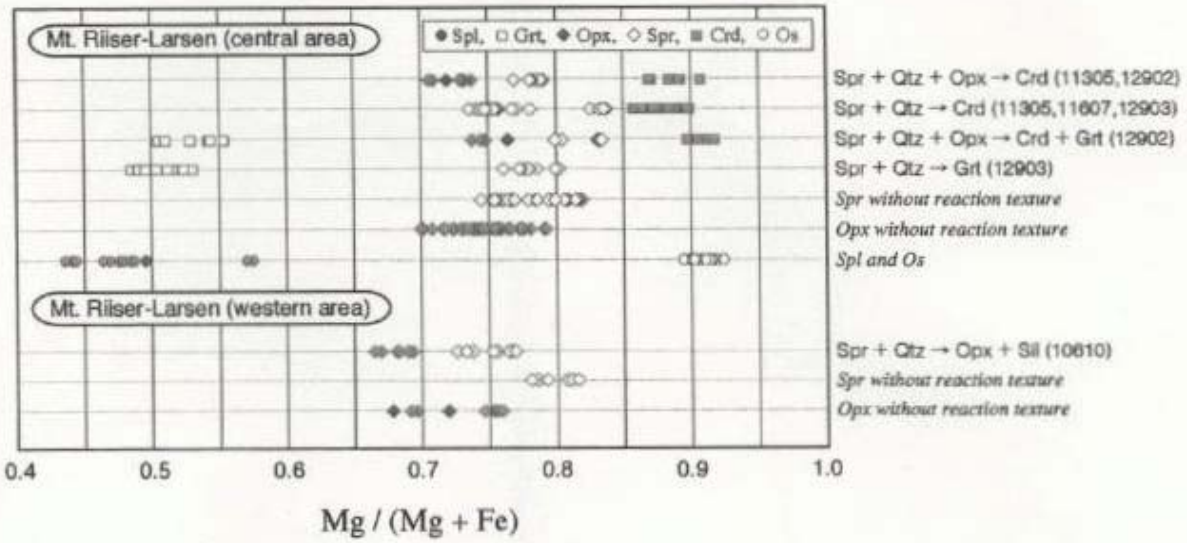

Fig.3.17 Mg/(Mg+Fe) ratios of constituent minerals in the sapphirine+quartz gneisses.

to uplift of the western area along major shear zone after isobaric cooling from the UHT conditions. Most of the area designated as the Napier Complex is covered by ice sheet, and the regional pressure gradient increasing toward south in the Napier Complex is estimated by outcrops exposed as isolated small mountains. Harley and Hensen (1990) produced a geo-isobar map that the pressure increases southward in the western part of the Napier Complex, mainly based on garnet-orthopyroxene geobarometry (Fig. 3.18). This study suggests that the regional pressure gradient in the Napier Complex does not monotonously increase southward. However, Harley and Hensen (1990) also interpreted that the uplift of south-west part of the Napier Complex relates with the transpressional tectonic event of the Proterozoic Rayner Complex. The western area representing deeper structural level than the eastern (central) area is consistent with the above interpretation (Fig. 3.18).

3.6. Summary

Peak P-T conditions of the Mt. Riiser-Larsen area are constrained by the mineral parageneses at the peak metamorphism and reaction textures after sapphirine + quartz as follows: > 1040°C and 0.6 ~ 0.8 GPa in the central part, and > 1030°C and 0.8 ~ 0.9 GPa in the western part of the area. Observed retrograde reaction textures are consistent with the previously proposed near isobaric cooling from the UHT conditions. The western area, deeper structural level, and the central area, shallower structural level, of the Mt. Riiser-Larsen have juxtaposed due to the movement of the sub-vertical shear zone after isobaric cooling, which is possibly in relation with the Proterozoic compressional tectonic regime.

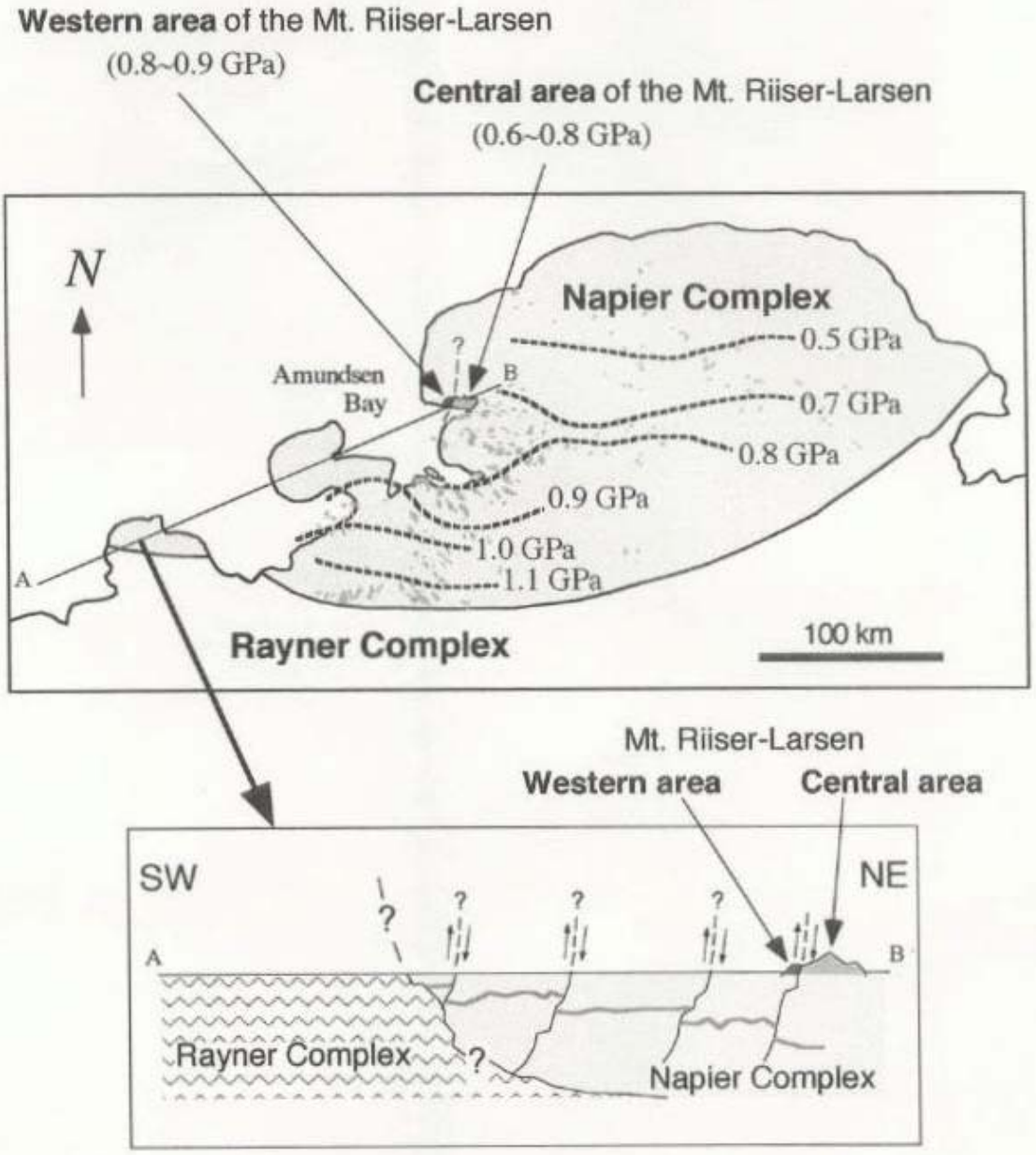

Fig. 3.18 Estimated pressure condition of the Mt. Riiser-Larsen area and its relation with regional pressure gradient within the Napier Complex. Pressure conditions at maximum temperature and schematic cross section of the western part of the Napier Complex and the Rayner Complex partly modified after Harley and Hensen (1990).

Chapter 4 Petrology and Metamorphism of Sapphirine-bearing Aluminous Gneisses from Tonagh Island

Abstract: A variety of Mg-rich silica-undersaturated aluminous gneisses containing sapphirine, spinel and corundum occur within the ultrahigh-temperature (UHT) metamorphic sequence at Tonagh Island in the Napier Complex, East Antarctica. They occur as blocks or pods in felsic (quartzo-feldspathic) gneisses or mafic granulite, or as thin layers around ultramafic rocks. The modes of occurrence, constituent minerals and mineral textures of these aluminous gneisses are different from each other, suggesting that they are derived from different protolith or formation process. Modes of field occurrence suggest that some of the aluminous gneisses in Tonagh Island may not be simple pelitic precursor but formed through the processes associated with partial melting or metasomatism. Various reaction textures and compositional zoning in constituent minerals, which reflect retrograde metamorphism, are commonly observed in these rocks. Garnet-orthopyroxene geothermobarometry using the chemical compositions of the cores of garnet and orthopyroxene yields slightly lower temperatures (800 ~ 1000°C at 0.5 ~ 1.0 GPa) than the thermal climax (>1100°C). Pressure condition of 0.8 ~ 1.1 GPa at the thermal peak (~ 1100°C) is estimated from the garnet-orthopyroxene geobarometry.

4.1. Introduction

A variety of sapphirine-bearing gneisses are found in Tonagh island, and they display at least three different modes of occurrences, i.e., 1) thin layers around ultramafic rock, 2) block in the alternation of felsic (quartzo-feldspathic) gneiss and mafic granulite, and 3) block surrounded by leucocratic quartzo-feldspathic gneiss. All of these gneisses are classified into silica-undersaturated aluminous gneiss as described above for rocks in the Mt. Riiser-Larsen area. The field occurrences in our survey suggest that some of them may be formed through the processes associated with partial melting or metasomatism. In this chapter, the field occurrences, petrography and mineral chemistry of the sapphirine-bearing aluminous gneisses from the northern part of the island (Units I and II) are described, and makes a brief discussion on the metamorphism of the area.

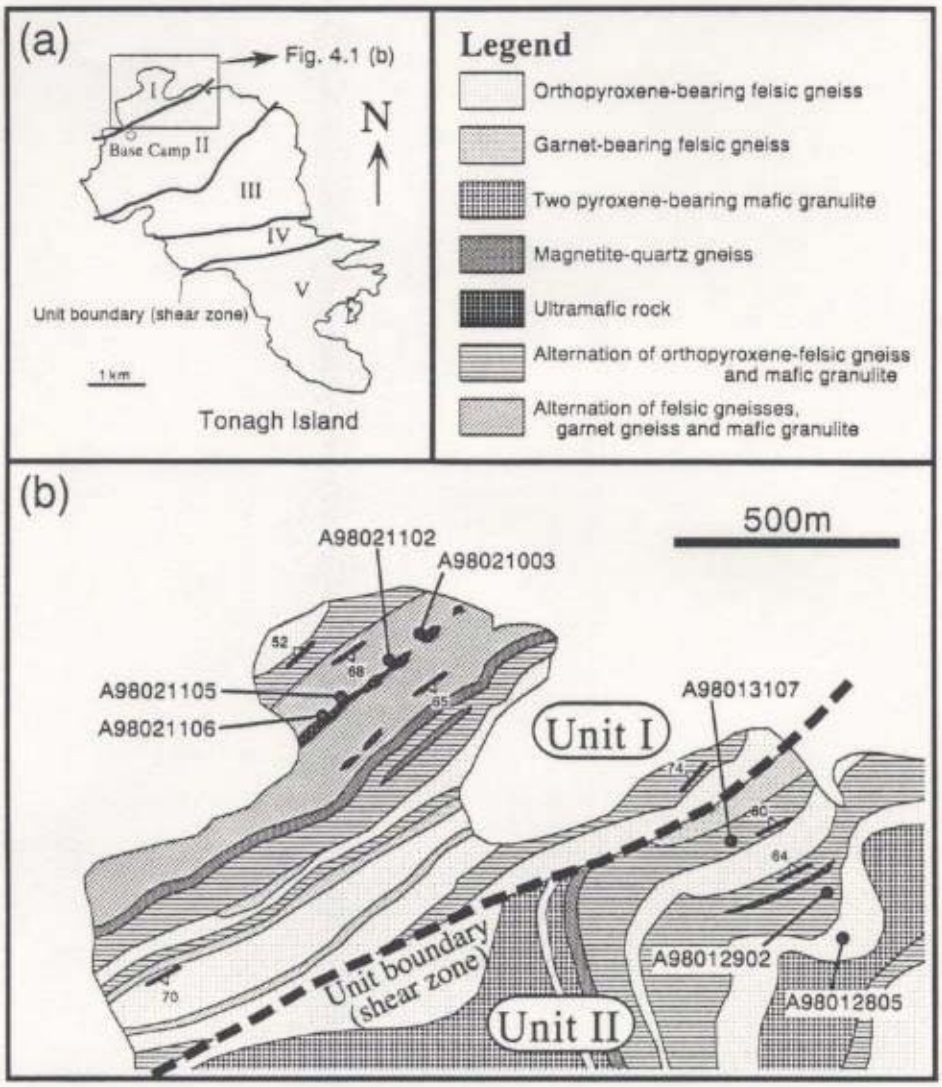

Fig. 4.1 Geological map of Tonagh Island (northern part). (a) Distributions of pseudotachylite- and mylonite-bearing shear zones which divide geological units (I, II, III, IV and V). (b) Geological map of the northern part of Tonagh Island. Sample localities of sapphirine-bearing aluminous gneisses described in the text.

4.2. Field occurrence and petrography

Sample localities of the aluminous gneisses described in this paper are shown in Fig. 4.1. Table 4.1 summarizes the constituent minerals and their chemical features.

(a) Sapphirine - garnet - orthopyroxene gneiss (A98021106A, A98021105A, A98021102H, A98021003E)

It occurs as several centimeters to a few meters thick layer around an ultramafic layer, which is locally boudinaged or shows pinch-and-swell structure, in the alternation zone of the northwest peninsula of the island (Fig. 4.2a). This layer crops out intermittently over 400 m along the strike. Mineral assemblages and modal proportion of constituent minerals are heterogeneous, and leucocratic feldspathic vein occasionally develops at the boudin neck or among the boudinaged ultramafic layer and surrounding aluminous gneisses. Representative lithologies are as follows:

A98021106A: Feldspathic portion containing garnet and sapphirine (Figs. 4.2c and e). Garnet is generally rounded. Sapphirine is porphyroblastic up to a few mm in diameter, and has exsolution lamellae of rutile and quartz. Xenomorphic and relatively fine-grained (less than 1 mm) orthopyroxene occasionally occurs around sapphirine. Matrix of the gneiss is composed of plagioclase (antiperthite) and alkali feldspar (perthite - mesoperthite). Quartz is not present.

A98021105A: Garnet and orthopyroxene-rich portion with minor amount of sapphirine and plagioclase (Figs. 4.2b and f). Garnet and orthopyroxene show granular texture. Sapphirine-orthopyroxene-plagioclase symplectite is formed around garnet. Sillimanite and cordierite are also present locally. Sillimanite is generally idiomorphic.

A98021102H: Spinel-bearing portion. Major constituent minerals are spinel, sapphirine, orthopyroxene, garnet, plagioclase and alkali feldspar. Sapphirine and garnet surround spinel and orthopyroxene, respectively (Fig. 4.2g). Corundum is locally accompanied by spinel. Retrograde biotite commonly occurs.

A98021003E: Idiomorphic sapphirine-rich portion (Figs. 4.2c and h). Constituent minerals are sapphirine, orthopyroxene, garnet, plagioclase and alkali feldspar (perthite - mesoperthite). Exsolution lamellae of rutile is observed in sapphirine. Garnet locally occurs between sapphirine and orthopyroxene (Fig. 4.12).

sample	Spr	Opx	Grt	Spl	Phl	Sil	Crn	Crd	Pl	Akfs	Qtz	Spr X_{Mg} min	Spr Al_2O_3 min	Spr Cr_2O_3 max	Opx X_{Mg} *	Opx Al_2O_3 max	Grt X_{Mg} max	Grt alm	Grt prp	Grt grs	Spl X_{Mg} max	Spl ZnO max	Phl X_{Mg} min	Phl F max
A98021106A	○	○	○			○			○	○		0.79	58.6	2.2	0.76	7.7	0.57	*0.42*	*0.55*	*0.02*				
A98021105A	○	○	○			○		○	○			0.84	61.6	0.1	0.79	10.4	0.62	*0.37*	*0.60*	*0.03*				
A98021102H	○	○	○	○			○		○	○		0.80	60.2	0.8	0.75	8.6	0.52	*0.46*	*0.50*	*0.03*	0.56	0.2		
A98021003E	○	○	○						○	○		0.80	61.2	0.7	0.78	8.5	0.63	*0.36*	*0.59*	*0.04*				
A98013107A	○			○	○		○		○			0.82	64.2	0.1							0.49	1.1	0.90	5.5
A98013107C	○			○	○		○	○	○			0.93	64.1	0.0							0.81	0.3	0.96	5.3
A98012902D	○	○	○						○			0.77	59.6	0.1	0.74	10.6	0.53	*0.46*	*0.52*	*0.01*				
A98012902I	○	○	○	○		○	○		○			0.76	61.4	0.1	0.69	9.3	0.53	*0.46*	*0.52*	*0.01*	0.56	1.0		
A98012902J	○	○	○						○			0.81	62.3	0.1	0.71	10.3	0.56	*0.43*	*0.55*	*0.01*				
A98012902P		○	○	○		○	○		○		(Δ)				0.69	9.2	0.52	*0.47*	*0.51*	*0.01*	0.65	1.1		
A98012805B	○	○	○	○		○	○		○	(Δ)	(Δ)	0.79	61.0	0.1	0.70	9.5	0.51	*0.48*	*0.49*	*0.02*	0.62	16.1		

○ : present (Δ) : local

X_{Mg} = Mg/(Mg+Fe) Al_2O_3, Cr_2O_3, ZnO, F : wt.% * : value at max Al_2O_3

Table 4.1 Constituent minerals and their chemical features in the aluminous gneisses. Mineral abbreviations are as follows. Spr: sapphirine, Opx: orthopyroxene, Grt: garnet, Spl: spinel, Phl: phlogopite, Sil: sillimanite, Crn: corundum, Crd: cordierite, Pl: plagioclase, Akfs: alkali feldspar, Qtz: quartz. Rutile, ilmenite, biotite, zircon and monazite are accessory phases.

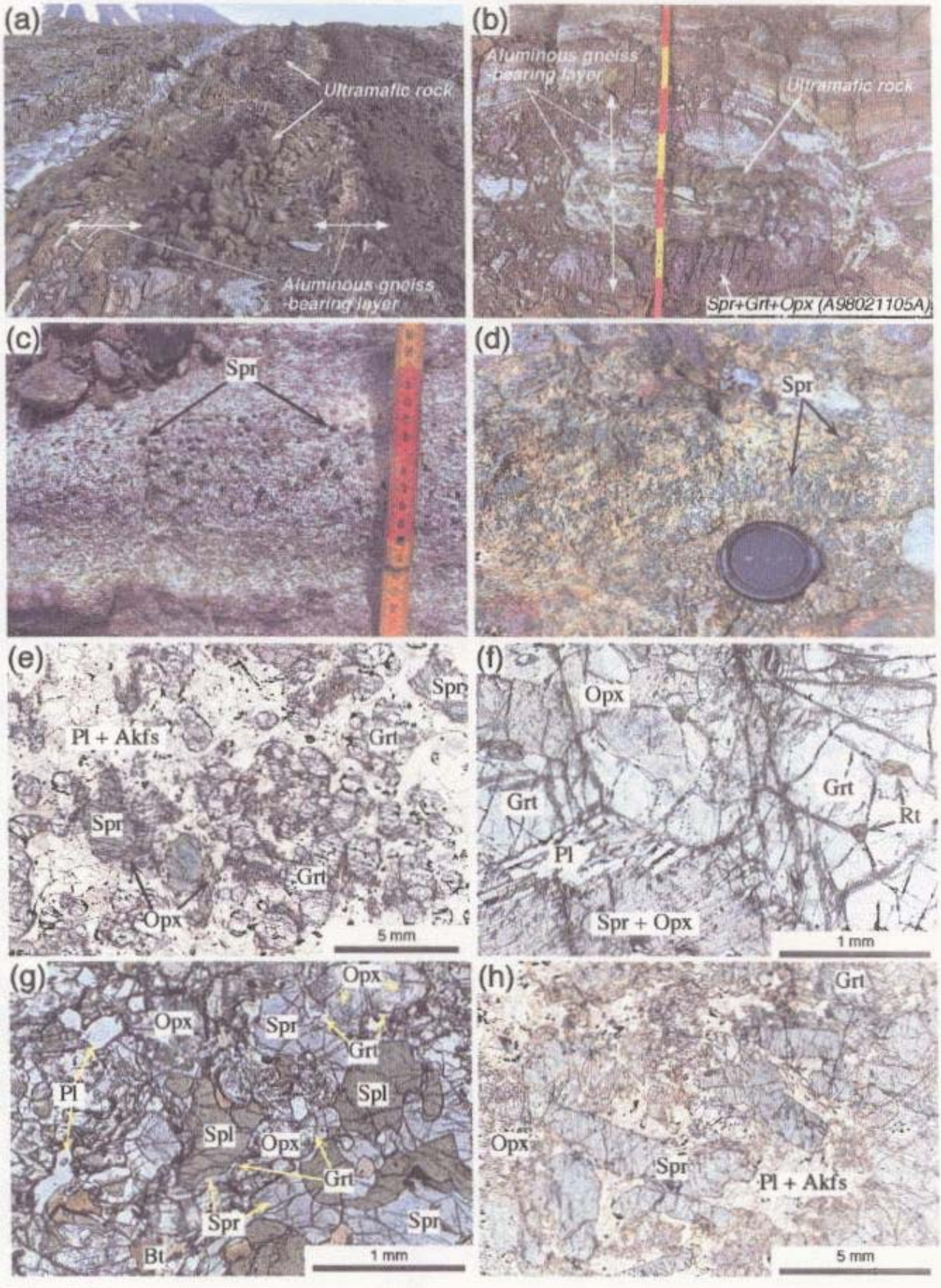
(a)
Ultramafic rock
Aluminous gneiss -bearing layer
(b)
Aluminous gneiss -bearing layer
Ultramafic rock
Spr+Grt+Opx (A98021105A)
(c)
Spr
(d)
Spr
(e)
Spr
Pl + Akfs
Grt
Spr
Grt
Opx
5 mm
(f)
Opx
Grt
Grt
Rt
Pl
Spr + Opx
1 mm
(g)
Opx
Opx
Spr
Grt
Pl
Spl
Spl
Opx
Grt
Spr
Spr
Bt
1 mm
(h)
Grt
Opx
Spr
Pl + Akfs
5 mm

Fig. 4.2

Fig. 4.2 (a) ~ (d) Sapphirine-bearing aluminous gneiss layer around ultramafic rock in the Unit I. (e) ~ (h) Photomicrograph of sapphirine-bearing aluminous gneisses in the Unit I. Plane-polarized light. (a) Boudinaged ultramafic layer accompanying sapphirine-bearing gneisses in the centimeter to meter order alternation of quartzo-feldspathic gneisses, mafic granulite, garnet gneiss, garnet-sillimanite gneiss, magnetite-quartz gneiss and pyroxenite. (b) Boudinaged ultramafic rock and surrounding feldspathic and aluminous gneisses. Garnet and orthopyroxene with minor sapphirine concentrate on the lower part of the photograph (A98021105). Leucocratic feldspathic vein develops at the boudin neck. (c) Garnet-bearing feldspathic portion in the aluminous layer (A98021106). Porphyroblastic sapphirine occurs and is accompanied by fine-grained orthopyroxene. (d) Idiomorphic sapphirine-rich portion (A98021003). (e) A98021106A: Porphyroblastic sapphirine and rounded garnet occur in the matrix of plagioclase (antiperthite) + alkali feldspar (perthite ~ mesoperthite). Fine-grained orthopyroxene occurs around sapphirine. (f) A98021105A: Granular orthopyroxene and garnet grains are concentrated. Symplectite of sapphirine-orthopyroxene-plagioclase occurs around garnet. (g) A98021102H: Brownish green spinel constitutes the rock. Spinel and orthopyroxene are generally surrounded by sapphirine and garnet, respectively. (h) A98021003E: Idiomorphic sapphirine grains are developed in the matrix of orthopyroxene, garnet, plagioclase and alkali feldspar.

Rutile is common in every rock type described above. Zircon and monazite are also minor.

(b) Corundum-spinel-sapphirine-phlogopite gneiss (A98013107)

It occurs as a block (ca. 2 m in diameter) in the alternation of orthopyroxene felsic gneiss and mafic granulite (Fig. 4.3a). Idiomorphic and porphyroblastic pseudomorph after corundum, which is mostly replaced by spinel and sapphirine, is present in phlogopite-rich matrix (Fig. 4.3b). Spinel encloses corundum, and both of them are surrounded by sapphirine. Phlogopite, plagioclase, sapphirine, corundum and subordinate cordierite constitute the matrix of the rock. Phlogopite, spinel and sapphirine in the central part of the block (A98013107C, Fig. 4.3c) are paler color than those in the marginal part (A98013107A, Fig. 4.3d), and reflect compositional variation of Mg / (Mg + Fe) ratio increasing toward the center (Tables 4.1 and 4.2).

(c) Spinel-sapphirine-garnet-orthopyroxene gneiss (A98012902)

It is enclosed within leucocratic quartzo-feldspathic gneiss (Figs. 4.3e and f). Garnet and orthopyroxene distribute separately each other and form monomineralic aggregates respectively. Plagioclase monomineralic thin vein (< 5 mm) distributes between the garnet and orthopyroxene aggregates (Figs. 4.3f and g). Spinel, sapphirine and sillimanite are associated with garnet and are commonly included in garnet (Fig. 4.3h). Corundum is sometimes accompanied by spinel. Rutile is common in the rock. A98012902D and A98012902J are the garnet and orthopyroxene rich portion in the aluminous block. A98012902I is the spinel- and corundum-bearing portion. A98012902P is marginal portion of the block and is adjacent to the surrounding quartzo-feldspathic gneiss.

(d) Spinel - corundum - sapphirine - garnet - orthopyroxene gneiss (A98012805B)

It occurs as a pod in felsic gneiss. Garnet and orthopyroxene distribute separately each other and form monomineralic aggregate. Plagioclase or alkali feldspar thin vein is present between garnet and orthopyroxene aggregates. Sapphirine, spinel and corundum are generally accompanied by or sometimes included in garnet and plagioclase. Quartz is rarely present and is restricted in the alkali feldspar vein. Rutile is common.

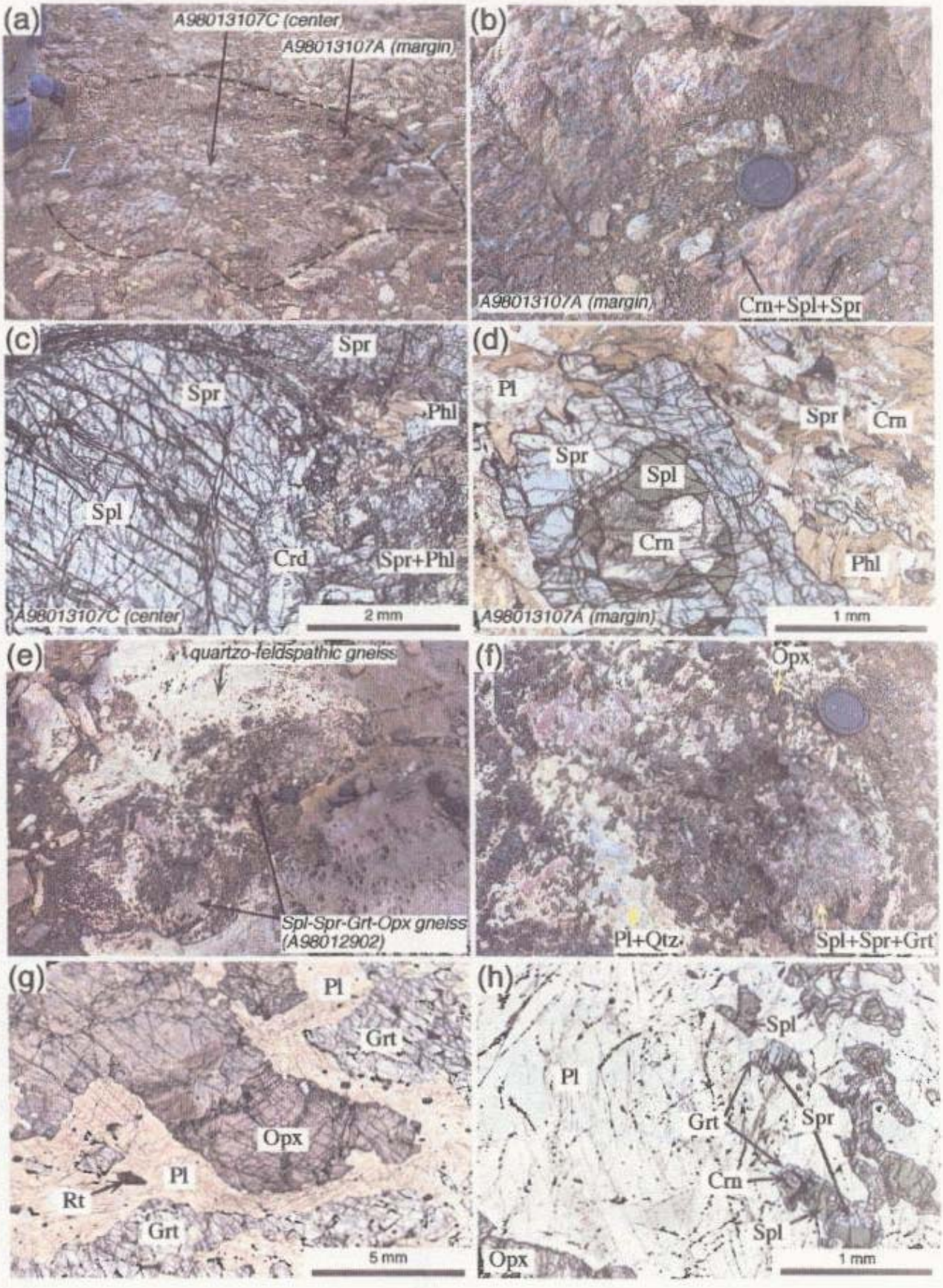
(a)
A98013107C (center)
A98013107A (margin)
(b)
A98013107A (margin)
Crn+Spl+Spr
(c)
Spr
Spr
Phl
Spl
Crd
Spr+Phl
A98013107C (center)
2 mm
(d)
Pl
Spr
Crn
Spr
Spl
Crn
Phl
A98013107A (margin)
1 mm
(e)
quartzo-feldspathic gneiss
Spl-Spr-Grt-Opx gneiss
(A98012902)
(f)
Opx
Pl+Qtz
Spl+Spr+Grt
(g)
Pl
Grt
Opx
Pl
Rt
Grt
5 mm
(h)
Spl
Pl
Grt
Spr
Crn
Spl
Opx
1 mm

Fig. 4.3

Fig. 4.3 (a) ~ (d) Corundum-spinel-sapphirine-phlogopite-bearing gneiss from the Unit II. (e) ~ (h) Spinel-sapphirine-garnet-orthopyroxene gneiss from the Unit II. (a) Field occurrence of the block of corundum-spinel-sapphirine-phlogopite gneiss. (b) Close up view of the marginal portion of the block. Idiomorphic and porphyroblastic pseudomorph after corundum, which is mostly replaced by spinel and sapphirine, is present in phlogopite-rich matrix. (c) Photomicrograph of the sample A98013107C. Spinel (X_{Mg} = 0.80 ~ 0.84) and sapphirine (X_{Mg} = 0.93 ~ 0.94) have extremely magnesian compositions and are colorless in the thin section. Plane-polarized light. (d) Photomicrograph of the sample A98013107A. Green spinel (X_{Mg} = 0.46 ~ 0.49) and pale blue sapphirine (X_{Mg} = 0.81 ~ 0.84) constitute the rock. Plane-polarized light. (e) Field occurrence of the spinel-sapphirine-garnet-orthopyroxene gneiss surrounded by leucocratic quartzo-feldspathic gneiss (A98012902). (f) Close up view of the gneiss. Plagioclase monomineralic thin vein distributes between the garnet and the orthopyroxene aggregates and is also connected to the relatively voluminous quartzo-feldspathic vein. (g) Photomicrograph of the sample A98012902P. Plagioclase monomineralic thin vein distributes between the garnet and the orthopyroxene aggregates. Plane-polarized light. (h) Photomicrograph of the sample A98012902I. Spinel, sapphirine and corundum are commonly surrounded by garnet. Plane-polarized light.

4.3. Mineral chemistry

Chemical analyses of constituent minerals were performed using an electron microprobe with an wavelength-dispersive X-ray analytical system (JEOL JXA-8800M) at the National Institute of Polar Research. Oxide ZAF correction was applied to analyses. Probe current was kept at about 8 nA with accelerating voltage at 15 kV. Synthesized pure oxides and natural minerals were used for standards. Chemical features and representative analyses of constituent minerals in the aluminous gneisses are summarized in Tables 4.1 and 4.2.

(a) Sapphirine

Mg/(Mg + Fe) ratio (= X_{Mg}) of sapphirine generally ranges from 0.76 to 0.85, but up to 0.94 at the central portion of the corundum-phlogopite block (A98013107C). It has pleochroism of colorless to pale blue. But high-Mg one (X_{Mg} > 0.9) is colorless. Sapphirine commonly shows weak compositional zoning of Al-increasing and Si-decreasing toward the rim (Fig. 4.4). In the sample A98021106A, up to 2.2 wt.% Cr_2O_3 is contained in sapphirine. Porphyroblastic sapphirine in the sample A98021106A has exsolution lamellae of quartz.

(b) Orthopyroxene

X_{Mg} of orthopyroxene ranges from 0.7 to 0.8. Orthopyroxene contains more than 10 wt.% Al_2O_3 in the core, decreasing toward the rim (Fig. 4.5). Garnet and sapphirine occur in the grain boundary of orthopyroxene as exsolution products from high-Al orthopyroxene.

(c) Garnet

Garnet in the aluminous gneisses is characterized by the high pyrope content up to 60 mol% and low grossular (< 4 mol%) and spessartine (< 1 mol%) contents. Coarse grains have compositional zoning of Fe and Ca increasing and Mg decreasing toward the rim (Fig. 4.6), reflecting retrograde intracrystalline element diffusion. Fine grains and exsolution products in the grain boundary of orthopyroxene has lower X_{Mg} than the core of the coarse one.

Table 4.2 Representative electron microprobe analyses of constituent minerals.

mineral	Sapphirine										Orthopyroxene										Spinel					
sample	Unit I : A9803-				Unit II : A9801-						Unit I : A9803-				Unit II : A9801-						A9803-	Unit II : A9801-				
	1106A	1105A	1102H	1003E	3107A	3107C	2902D	2902E	2902J	2803B	1106A	1105A	1102H	1003E	2902D	2902E	2902J	2902P	2803B		1102H	3107A	3107C	2902E	2902P	2803B
point	59	12	141	1	28	55	58	9	2	68	63	5	152	116	54	56	18	45	42		132	7	51	5	22	160
wt.%																										
SiO_2	14.89	13.65	14.43	14.14	12.89	14.29	14.93	14.06	13.90	13.99	51.56	51.40	50.91	52.19	49.69	49.25	48.42	49.39	50.06		0.08	0.01	0.01	0.00	0.07	0.00
TiO_2	0.00	0.08	0.04	0.02	0.02	0.04	0.10	0.06	0.04	0.03	0.12	0.34	0.10	0.13	0.12	0.14	0.12	0.20	0.14		0.00	0.00	0.06	0.00	0.23	0.00
Al_2O_3	58.37	62.60	60.23	61.15	64.23	64.10	59.55	61.39	62.33	62.97	7.65	8.14	8.64	8.49	10.55	9.12	10.35	9.23	9.46		63.42	64.55	62.58	64.60	64.98	62.69
Cr_2O_3	1.03	0.05	0.72	0.50	0.00	0.00	0.00	0.02	0.05	0.06	0.26	0.08	0.17	0.07	0.00	0.01	0.00	0.05	0.00		2.37	0.00	0.00	0.08	0.07	0.00
FeO*	7.12	5.60	7.25	7.19	6.14	2.61	8.75	8.34	7.27	7.97	14.56	14.09	14.89	13.47	15.44	18.78	17.43	18.39	17.29		25.08	22.41	9.81	20.39	15.79	13.75
MnO	0.04	0.06	0.16	0.08	0.04	0.04	0.05	0.07	0.00	0.05	0.07	0.05	0.08	0.11	0.05	0.20	0.12	0.08	0.14		0.09	0.36	0.04	0.02	0.00	0.00
ZnO	0.02	0.08	0.00	0.00	0.00	0.09	0.01	0.09	0.03	0.00	0.00	0.00	0.05	0.04	0.08	0.01	0.07	0.11	0.02		0.16	0.89	0.16	1.01	1.05	15.52
MgO	17.03	17.37	16.72	16.90	16.86	19.61	16.47	15.61	17.24	17.24	26.31	26.60	25.38	26.76	24.00	23.52	23.43	21.87	22.88		14.08	11.95	21.60	13.80	16.30	9.15
CaO	0.02	0.00	0.00	0.01	0.02	0.08	0.00	0.00	0.01	0.00	0.03	0.05	0.08	0.10	0.00	0.01	0.04	0.09	0.09		0.02	0.01	0.02	0.00	0.01	0.02
Na_2O	0.04	0.00	0.04	0.00	0.00	0.01	0.05	0.01	0.01	0.05	0.03	0.22	0.00	0.05	0.00	0.00	0.00	0.00	0.04							
K_2O	0.00	0.00	0.00	0.00	0.00	0.00	0.00	0.00	0.00	0.00	0.00	0.00	0.00	0.00	0.00	0.00	0.00	0.00	0.00		0.00	0.00	0.00	0.00	0.00	0.00
total	99.56	99.44	99.59	100.02	100.20	100.87	99.87	99.55	100.85	100.36	100.59	100.92	100.30	101.38	99.95	100.04	100.19	100.41	100.12		100.25	100.16	100.28	99.85	100.50	101.13
cations	O = 20										O = 6										O = 4					
Si	1.784	1.617	1.723	1.680	1.519	1.647	1.784	1.683	1.635	1.662	1.855	1.820	1.818	1.829	1.784	1.798	1.757	1.794	1.811		0.001	0.000	0.000	0.000	0.002	0.000
Ti	0.000	0.007	0.004	0.002	0.002	0.003	0.009	0.005	0.004	0.003	0.003	0.009	0.003	0.003	0.003	0.004	0.003	0.005	0.004		0.000	0.000	0.001	0.000	0.004	0.000
Al	8.270	8.742	8.478	8.561	8.932	8.705	8.388	8.659	8.641	8.527	0.321	0.340	0.364	0.351	0.446	0.392	0.442	0.395	0.402		1.954	2.005	1.996	1.995	2.008	2.004
Cr	0.173	0.005	0.068	0.050	0.000	0.000	0.000	0.002	0.005	0.006	0.007	0.001	0.005	0.002	0.000	0.000	0.000	0.001	0.000		0.049	0.000	0.000	0.001	0.001	0.000
Fe	0.713	0.555	0.724	0.714	0.695	0.251	0.872	0.825	0.715	0.792	0.453	0.417	0.443	0.401	0.463	0.573	0.529	0.558	0.522		0.489	0.494	0.203	0.447	0.346	0.312
Mn	0.004	0.006	0.016	0.008	0.004	0.004	0.005	0.007	0.000	0.005	0.002	0.001	0.002	0.003	0.002	0.006	0.004	0.002	0.004		0.002	0.008	0.001	0.000	0.000	0.000
Zn	0.002	0.003	0.000	0.000	0.000	0.008	0.001	0.008	0.000	0.000	0.000	0.000	0.001	0.000	0.002	0.000	0.002	0.003	0.001		0.002	0.017	0.003	0.019	0.020	0.311
Mg	3.042	3.069	2.977	2.992	2.963	3.368	2.955	2.785	3.022	3.054	1.396	1.404	1.351	1.398	1.284	1.226	1.278	1.218	1.234		0.549	0.469	0.795	0.519	0.618	0.370
Ca	0.003	0.000	0.000	0.001	0.002	0.010	0.000	0.000	0.001	0.000	0.001	0.002	0.003	0.004	0.000	0.000	0.002	0.003	0.003		0.001	0.000	0.001	0.000	0.000	0.001
Na	0.008	0.000	0.009	0.000	0.000	0.002	0.007	0.002	0.002	0.012	0.002	0.015	0.000	0.025	0.000	0.000	0.002	0.000	0.003							
K	0.000	0.000	0.000	0.000	0.000	0.000	0.000	0.000	0.000	0.000	0.000	0.000	0.000	0.000	0.000	0.000	0.000	0.000	0.000		0.000	0.000	0.000	0.000	0.000	0.000
total	13.999	14.004	13.999	14.008	14.018	13.998	14.001	13.976	14.026	14.071	4.000	4.009	3.992	3.994	3.984	3.999	4.019	3.999	3.986		2.998	2.993	3.000	3.001	2.989	2.998
X_{Mg}	0.81	0.85	0.80	0.81	0.85	0.93	0.77	0.77	0.81	0.79	0.76	0.77	0.75	0.78	0.73	0.68	0.71	0.69	0.70		0.56	0.49	0.80	0.55	0.63	0.54

* total Fe as FeO

mineral	Garnet								Phlogopite	
sample	Unit I : A9803-				Unit II : A9801-				Unit II : A9801-	
	1106A	1105A	1102H	1003E	2902D	2902E	2902J	2902P	2803B	3107A	3107C
point	86	49	143	73	37	67	18	20	51	2.6	2.19
wt.%											
SiO_2	40.97	41.37	40.07	40.82	40.54	40.66	41.48	41.05	40.34	40.93	42.71
TiO_2	0.05	0.02	0.00	0.04	0.01	0.02	0.00	0.10	0.00	1.92	1.13
Al_2O_3	23.13	23.39	23.23	23.51	23.25	23.29	23.47	23.39	22.91	13.92	13.62
Cr_2O_3	0.11	0.00	0.06	0.00	0.00	0.00	0.00	0.00	0.00	0.00	0.01
FeO*	21.63	18.29	23.10	17.49	22.13	21.94	20.69	21.64	23.04	4.38	1.47
MnO	0.11	0.37	0.44	0.53	0.15	0.31	0.42	0.42	0.40	0.04	0.00
ZnO	0.01	0.02	0.05	0.00	0.00	0.04	0.07	0.00	0.00	0.00	0.00
MgO	14.46	16.42	13.67	16.38	14.02	13.99	14.94	13.33	13.00	24.25	26.90
CaO	0.92	1.00	1.33	1.51	0.40	0.51	0.50	0.40	0.91	0.00	0.01
Na_2O	0.00	0.04	0.00	0.00	0.00	0.04	0.01	0.02	0.01	0.30	0.98
K_2O	0.00	0.00	0.00	0.00	0.00	0.00	0.00	0.00	0.00	10.65	9.39
F										5.26	5.04
-O										-2.21	-2.12
total	101.37	100.92	101.05	100.28	100.50	100.80	101.58	100.35	100.61	99.44	99.14
cations	O = 12									O = 22	
Si	3.003	3.005	2.983	2.980	2.993	2.998	3.013	3.030	3.004	5.759	5.890
Ti	0.002	0.000	0.000	0.002	0.001	0.001	0.000	0.006	0.000	0.203	0.117
Al	1.998	2.001	1.959	2.022	2.023	2.024	2.009	2.034	2.011	2.308	2.214
Cr	0.006	0.000	0.004	0.000	0.000	0.000	0.000	0.000	0.000	0.000	0.001
Fe	1.326	1.110	1.438	1.068	1.366	1.353	1.256	1.336	1.435	0.515	0.170
Mn	0.007	0.022	0.028	0.033	0.009	0.019	0.026	0.026	0.025	0.005	0.000
Zn	0.001	0.001	0.003	0.000	0.000	0.002	0.003	0.000	0.000	0.000	0.000
Mg	1.580	1.777	1.517	1.783	1.543	1.534	1.618	1.467	1.443	5.086	5.531
Ca	0.072	0.078	0.106	0.118	0.032	0.040	0.039	0.032	0.073	0.000	0.001
Na	0.000	0.006	0.000	0.000	0.000	0.006	0.001	0.003	0.001	0.082	0.262
K	0.000	0.000	0.000	0.000	0.000	0.000	0.000	0.000	0.000	1.912	1.653
F										2.340	2.198
total	7.995	7.999	8.038	8.006	7.967	7.981	7.965	7.954	7.992	15.870	15.038
X_{Mg}	0.54	0.62	0.51	0.63	0.53	0.53	0.56	0.52	0.50	0.91	0.97
alm	0.45	0.37	0.47	0.36	0.46	0.46	0.43	0.47	0.48	-	-
prp	0.53	0.59	0.49	0.59	0.51	0.52	0.53	0.51	0.49	-	-
grs	0.02	0.03	0.03	0.04	0.01	0.01	0.01	0.01	0.02	-	-
sps	0.00	0.01	0.01	0.01	0.00	0.01	0.01	0.01	0.01	-	-

* total Fe as FeO

mineral	Plagioclase										Alkali feldspar			
sample	Unit I : A9803-					Unit II : A9801-					Unit I : A9803-			A9801-
	1106A	1105A	1102H	1102K	1003E	3107A	2902D	2902E	2902J	2803B	1106A	1102H	1003E	2803B
point	80	16	98	104	5	16	59	92	10	13	86	105	7	170
wt.%			core	rim										
SiO_2	61.79	60.21	58.37	57.14	57.31	62.71	64.66	64.98	63.20	64.79	62.88	65.23	65.07	64.54	63.06
TiO_2	0.00	0.06	0.00	0.00	0.00	0.04	0.02	0.00	0.07	0.00	0.00	0.00	0.00	0.00	0.00
Al_2O_3	24.60	24.67	25.81	27.08	27.10	23.43	21.81	21.89	22.07	22.14	23.32	18.73	18.47	18.68	18.63
Cr_2O_3	0.08	0.00	0.00	0.01	0.00	0.08	0.00	0.04	0.08	0.09	0.00	0.06	0.01	0.00	0.01
FeO*	0.00	0.04	0.00	0.02	0.05	0.13	0.00	0.04	0.32	0.01	0.10	0.00	0.00	0.00	0.00
MnO	0.00	0.02	0.08	0.12	0.05	0.00	0.00	0.09	0.08	0.02	0.08	0.00	0.08	0.00	0.00
MgO	0.00	0.08	0.01	0.00	0.08	0.00	0.00	0.00	0.00	0.00	0.00	0.00	0.00	0.00	0.00
CaO	5.83	6.45	8.46	9.00	8.75	4.46	2.70	2.86	3.36	3.09	4.23	0.20	0.24	0.18	0.08
Na_2O	8.28	7.90	7.13	6.23	6.38	8.73	9.81	9.71	9.63	9.58	9.01	1.54	1.45	1.42	1.10
K_2O	0.14	0.19	0.08	0.35	0.10	0.06	0.39	0.48	0.33	0.56	0.20	14.58	14.44	14.48	14.07
BaO	0.00	0.00	0.16	0.01	0.00	0.05	0.07	0.25	0.15	0.02	0.14	0.12	0.27	0.47	2.74
total	100.47	99.55	100.05	99.96	99.77	99.66	99.46	100.34	99.21	100.30	99.91	100.46	99.98	99.97	99.64
cations	O = 8											O = 8			
Si	2.734	2.693	2.594	2.566	2.572	2.778	2.857	2.861	2.820	2.849	2.786	2.987	2.995	2.980	2.964
Ti	0.000	0.002	0.000	0.000	0.000	0.001	0.001	0.000	0.002	0.000	0.000	0.000	0.000	0.000	0.000
Al	1.278	1.300	1.708	1.433	1.433	1.223	1.136	1.136	1.161	1.147	1.218	1.011	1.002	1.016	1.032
Cr	0.001	0.000	0.000	0.000	0.000	0.001	0.000	0.001	0.003	0.000	0.000	0.002	0.000	0.000	0.000
Fe	0.000	0.001	0.000	0.001	0.002	0.006	0.000	0.001	0.012	0.000	0.004	0.000	0.000	0.000	0.000
Mn	0.000	0.001	0.001	0.005	0.002	0.000	0.000	0.005	0.001	0.001	0.001	0.000	0.001	0.000	0.000
Mg	0.000	0.002	0.001	0.000	0.002	0.000	0.000	0.000	0.000	0.000	0.000	0.000	0.000	0.000	0.000
Ca	0.273	0.308	0.703	0.433	0.420	0.212	0.128	0.135	0.161	0.146	0.201	0.010	0.012	0.009	0.002
Na	0.708	0.685	0.574	0.542	0.555	0.750	0.840	0.829	0.815	0.817	0.774	0.137	0.129	0.145	0.100
K	0.008	0.011	0.005	0.020	0.006	0.003	0.022	0.027	0.019	0.031	0.011	0.852	0.848	0.850	0.844
Ba	0.000	0.000	0.003	0.000	0.000	0.001	0.000	0.004	0.003	0.000	0.002	0.002	0.005	0.009	0.050
total	4.994	5.003	4.995	5.000	4.992	4.975	4.985	4.997	5.015	4.994	4.997	5.001	4.992	5.012	4.992
an	0.28	0.31	0.71	0.44	0.43	0.22	0.13	0.14	0.16	0.15	0.20	0.01	0.01	0.01	0.00
ab	0.71	0.68	0.28	0.54	0.56	0.78	0.85	0.84	0.82	0.82	0.79	0.14	0.13	0.14	0.11
or	0.01	0.01	0.01	0.02	0.01	0.00	0.02	0.03	0.02	0.03	0.01	0.85	0.86	0.85	0.89

* total Fe as FeO

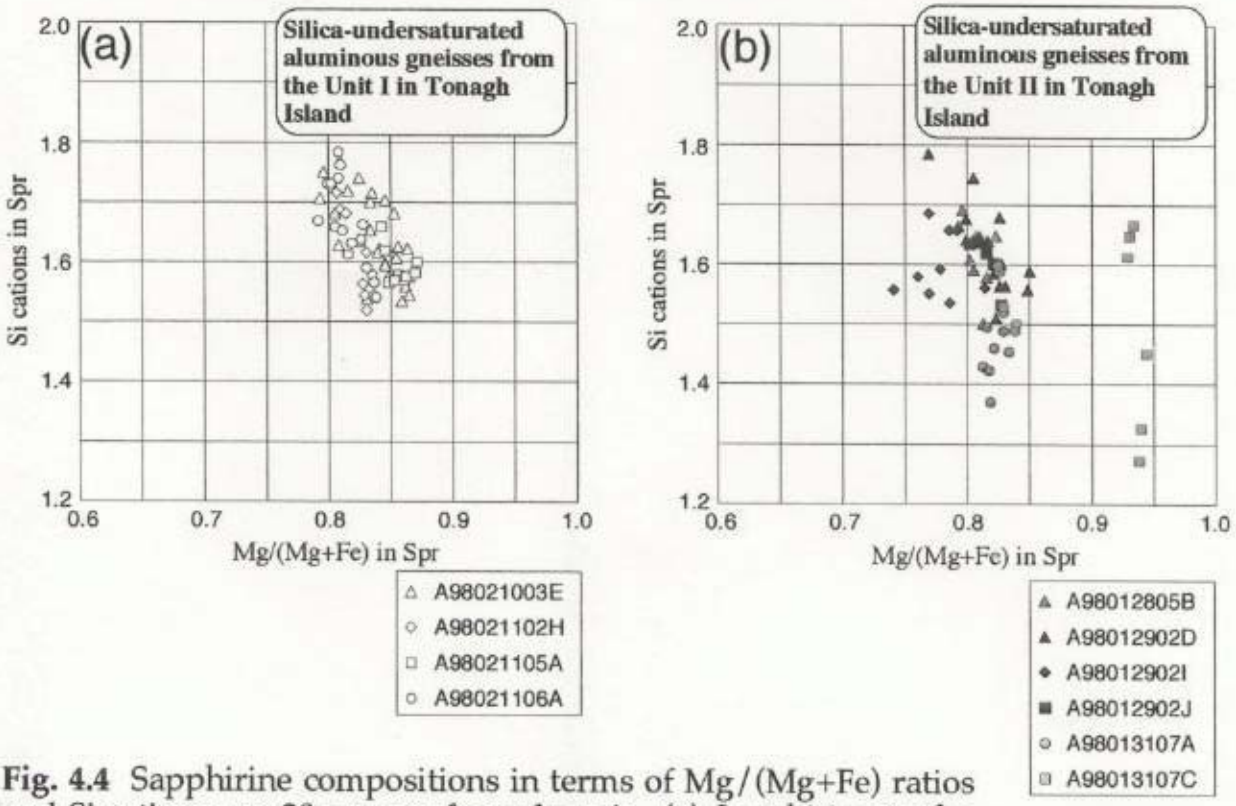

Fig. 4.4 Sapphirine compositions in terms of Mg/(Mg+Fe) ratios and Si cations per 20-oxygen formula unit. (a) Sapphirine in the silica-undersaturated aluminous gneisses from the Unit I. (b) Sapphirine in the silica-undersaturated aluminous gneisses from the Unit II.

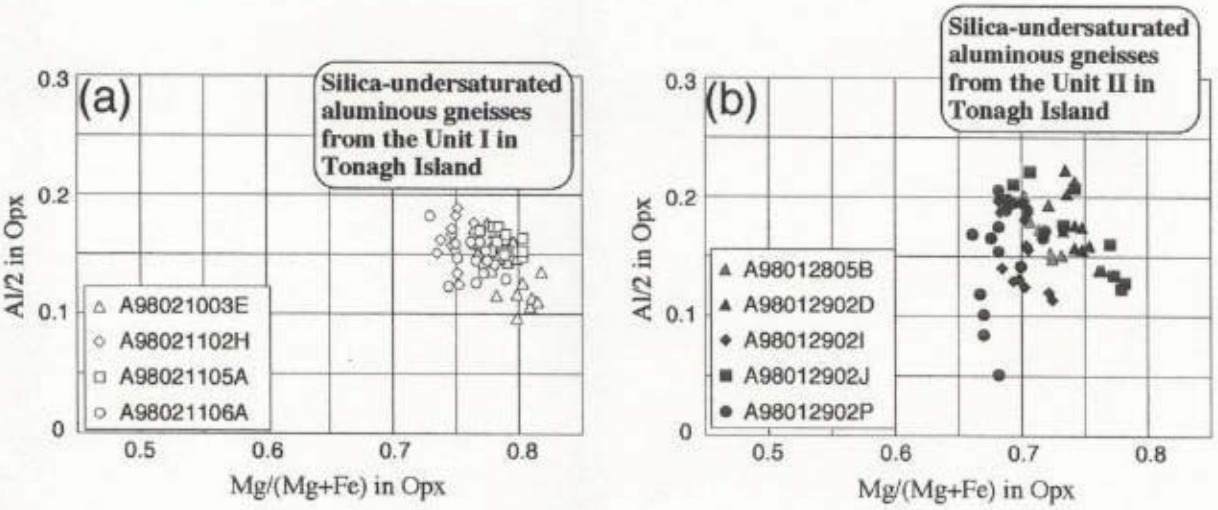

Fig. 4.5 Orthopyroxene compositions in terms of Mg/(Mg+Fe) ratios and Al cations/2 per 6-oxygen formula unit. (a) Orthopyroxene in the silica-undersaturated aluminous gneisses from the Unit I. (b) Orthopyroxene in the silica-undersaturated aluminous gneisses from the Unit II.

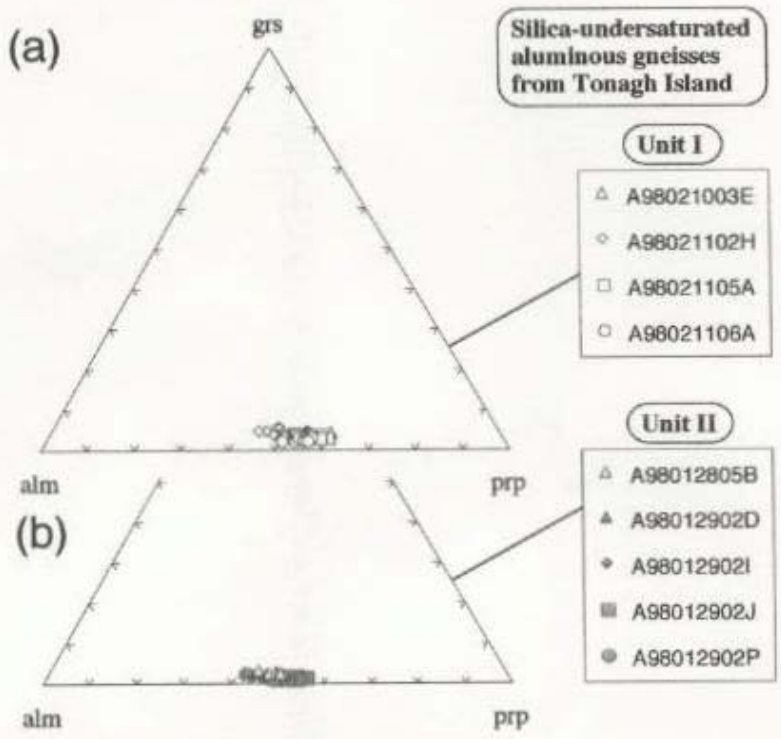

Fig. 4.6 Grossular (grs)-almandine (alm)-pyrope (prp) plot of garnet compositions. (a) Garnet from silica-undersaturated aluminous gneisses from the Unit I of Tonagh Island. (b) Garnet from silica-undersaturated aluminous gneisses from the Unit II of Tonagh Island.

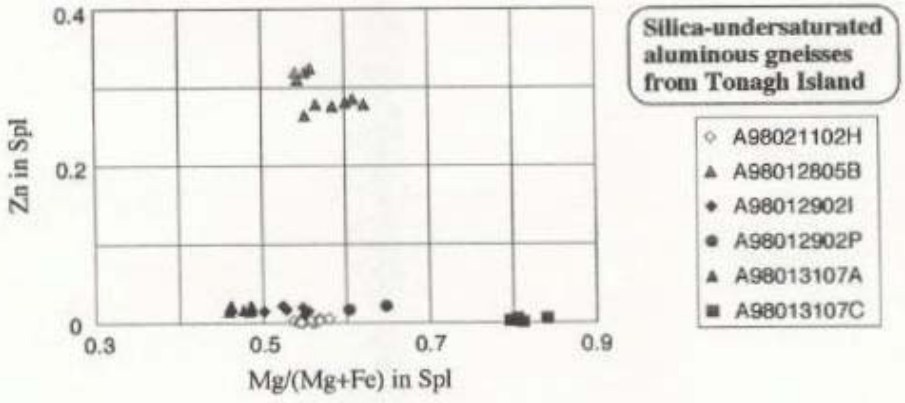

Fig. 4.7 Spinel compositions in terms of Mg/(Mg+Fe) ratios and Zn cations per 4-oxygen formula unit.

(d) Spinel

X_{Mg} of spinel generally ranges from 0.46 to 0.65, except that from the central portion of the corundum-phlogopite block (A98013107C) up to 0.81. Spinel in the sample A98012805B contains ZnO of up to 16 wt.%. (Fig. 4.7)

(e) Phlogopite

Non-retrograde phlogopite is contained only in the sample A98013107. X_{Mg} ranges from 0.90 ~ 0.97. Phlogopite in A98013107C, which is collected from the center portion of the corundum-phlogopite block, has higher X_{Mg} than that in A98013107A, which from the marginal portion of the block. Both of them contain about 5 wt.% of F.

(f) Plagioclase

Chemical compositions of plagioclase are shown in Fig. 4.8. Plagioclase in the aluminous gneisses around ultramafic layer (A98021106A, A98021105A, A98021102H, A98021003E) is characterized by relatively high anorthite content. Plagioclase in A98021102H and A98021003E show compositional zoning of decreasing anorthite content toward the rim, from 75 mol% to 48 mol% and from 47 mol% to 37 mol%, respectively. Some plagioclase grains in the samples A98021106A and A98021003E have antiperthitic exsolution lamellae.

Plagioclase from the other aluminous gneisses has relatively lower anorthite content than the above. Plagioclase occurring as the thin vein between garnet and orthopyroxene in the sample A98012902 shows weak compositional zoning of increasing anorthite content (less than 2 mol percentage points) from garnet-side to orthopyroxene-side.

(g) Alkali feldspar (mesoperthite)

Occurrence of alkali feldspar is restricted in the aluminous gneisses around ultramafic rocks (A98021003E, A98021102H, A98021106A) or in the leucocratic portion of the aluminous gneiss (A98012805B). Chemical compositions of the analyzed alkali feldspar are represented in Fig. 4.8. Exsolution lamellae commonly develops, and original mineral compositions of mesoperthite (and antiperthitic plagioclase) are estimated from modal proportions of host and lamellae multiplied by chemical compositions of each. Chemical compositions of mesoperthitic alkali feldspars are characterized by high anorthite content up to 17 mol% (an:ab:or = 17:43:40, in A98021106A). Alkali feldspars in the sample A98012805B shows chemical zoning of wide compositional range from perthite (an:ab:or = 5:36:59) to antiperthite (an:ab:or = 13:63:14) almost continuously.

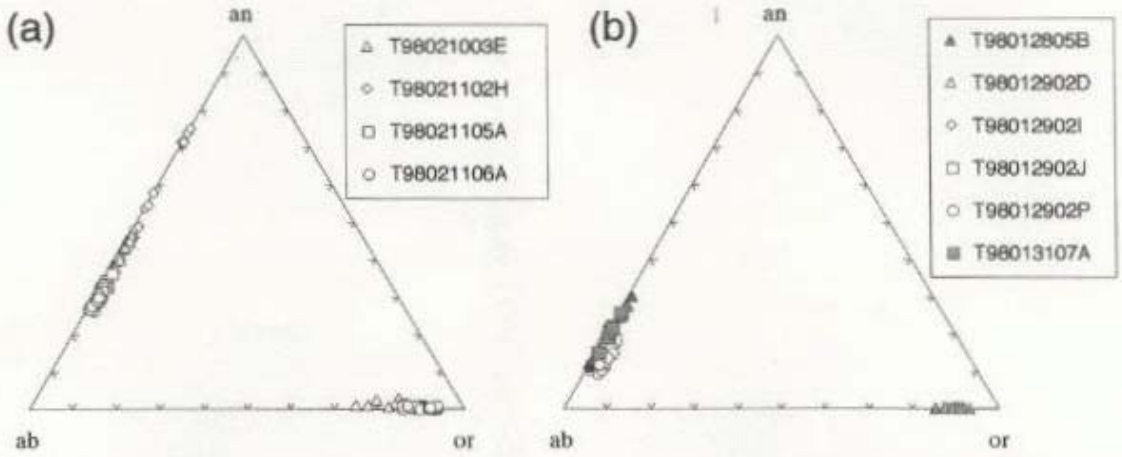

Fig. 4.8 Anorthite (an)-Albite (ab)-orthoclase (or) plot of feldspar compositions. (a) Feldspar from silica-undersaturated aluminous gneisses from the Unit I of Tonagh Island. (b) Feldspar from silica-undersaturated aluminous gneisses from the Unit II of Tonagh Island.

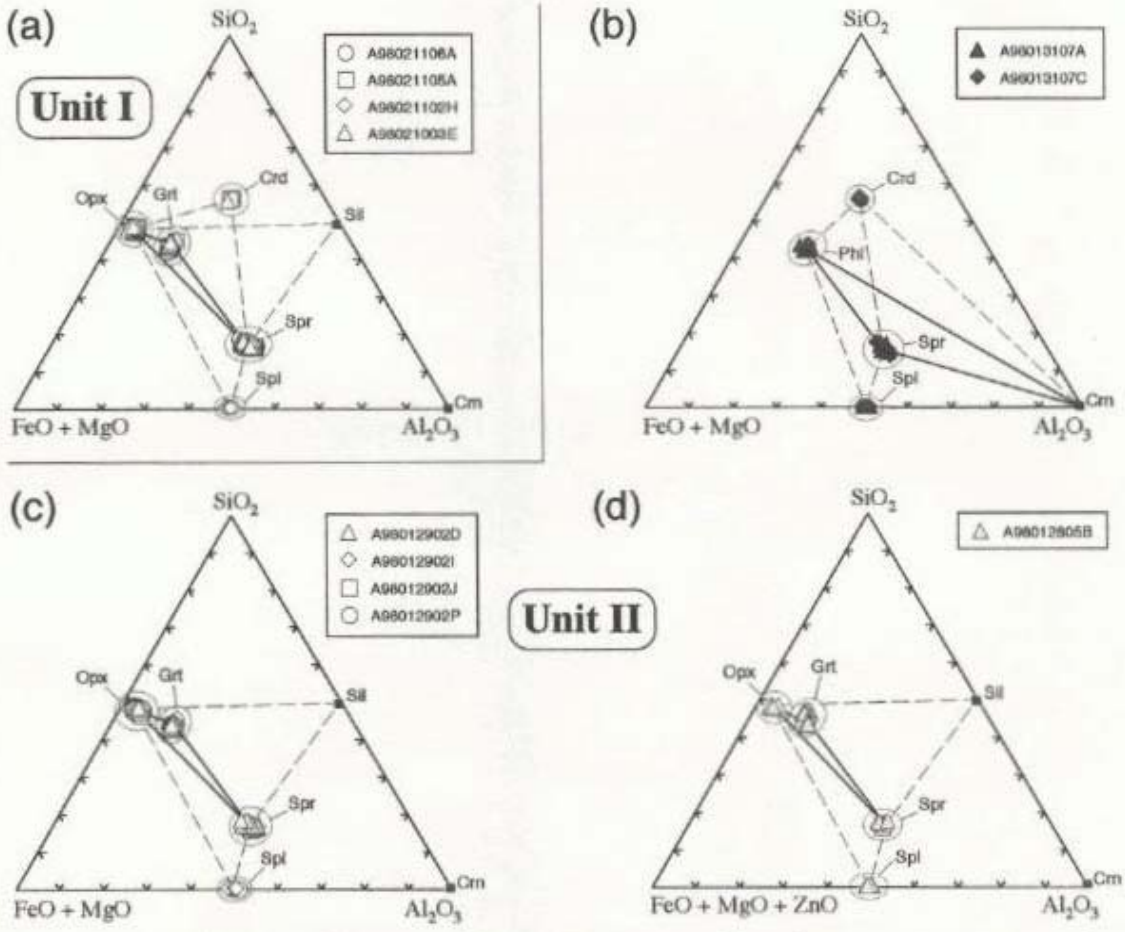

Fig. 4.9 SiO2-Al2O3-(FeO+MgO) projection of the phases constituting the aluminous gneisses. Phlogopite is projected from K2O. Solid lines represent initial mineral parageneses. Dashed lines indicate local or retrograde parageneses. (a) Aluminous gneisses from the Unit I. (b) The sample A98013107 from the Unit II. (c) The sample A98012902 from the Unit II. (d) The sample A98012805B from the Unit II. ZnO is added to FeO + MgO, because spinel in this sample contains over 30 mol% of ZnO.

4.4. Discussion

4.4.1. Lithological features of the aluminous gneisses

Fig. 4.9 illustrates the mineral compositions and mineral parageneses of the aluminous gneisses. The important feature is the quartz-free silica-undersaturated mineral parageneses composed of relatively high X_{Mg} phases. Sapphirine + garnet + orthopyroxene is the stable mineral paragenesis for all analyzed samples (A98021106A, A98021105A, A98021102H and A98021003E) from the Unit I. Spinel is the additional constituent for A98021102H. Cordierite and sillimanite locally constitute the gneisses (A98021106A, A98021105A) and are considered to reflect the differences of local bulk compositions. Some cordierite, sillimanite and garnet grains are obviously retrograde products, but it is difficult to judge whether the other cordierite, sillimanite and garnet grains are stable phase or not at the peak metamorphism from mineral textures and mineral compositions. A98012902 and A98012805B from the Unit II also show the similar mineral assemblages to those from the Unit I, but sapphirine is commonly surrounded by garnet. This observation suggests that the sapphirine has possibly coexisted with garnet and orthopyroxene at the peak conditions, and that garnet is formed around sapphirine during retrograde metamorphism. A98012902 and A98012805B occasionally contain spinel, corundum and sillimanite, and are considered to reflect the differences of local bulk compositions. Sapphirine + corundum + phlogopite is the stable mineral paragenesis for A98013107 in the Unit II.

The occurrence of silica-undersaturated aluminous gneiss from the Unit I (A98021106A, A98021105A, A98021102H and A98021003E) is restricted to the layers between ultramafic rock and quartzo-feldspathic rock. This suggests that the formation of the aluminous gneiss is originated from the interaction (whether metasomatism or mixing accompanied by partial melting) between the ultramafic rock and the quartzo-feldspathic rock. However, the definite formation process is beyond the scope of this study.

A98012902 and A98012805B from the Unit II are associated with leucocratic vein composed of quartz + feldspar (either plagioclase or plagioclase + alkali feldspar) or of monomineralic plagioclase. The leucocratic vein should be crystallized from melt judging from the field occurrence (Figs. 4.3e and f), and, therefore, suggests that the formation of the aluminous gneisses resulted from partial melting.

A98013107 is composed of a large amount of F-bearing phlogopite with corundum-spinel-sapphirine porphyroblast. This represents not pelitic but rather ultramafic bulk chemical composition. Higher X_{Mg} of the constituent minerals in the center (A98013107C) of the block than those in the margin (A98013107A) indicates the compositional zonal structure of the block. It is difficult to judge whether this zonal structure of the block reflects original compositional variation or is formed through the process associated with metasomatism.

4.4.2. *Metamorphic conditions of the aluminous gneisses*

Quartz does not coexist with sapphirine, spinel or corundum in the aluminous gneisses discussed here. Metamorphic conditions cannot be constrained by the phase relation because of high degree of freedom in the system. Geothermobarometry using element partitioning between garnet and orthopyroxene (Harley, 1984b; Harley, 1984a; corrected by Fitzsimons and Harley, 1994) indicates equilibrium conditions of 800~1000°C and 0.5~1.0 GPa, from garnet core of the highest pyrope content and orthopyroxene core of the highest Al content (Fig. 4.10). The estimated temperatures are lower than those estimated from mineral compositions of mesoperthitic alkali feldspar in the same sample indicating >1100°C (see Chapter 5) and from the occurrence of sapphirine-quartz association in the central part of Tonagh Island, suggesting >1030°C. Fig. 4.11 illustrates the compositional zoning patterns of Mg and Ca in garnet and those of Fe and Al in orthopyroxene. Mg and Al components are enriched in cores of garnet and orthopyroxene, respectively, and these compositional zoning patterns are considered to reflect intracrystalline element diffusion during retrograde metamorphism. Al in orthopyroxene, which is modeled in geobarometer (Harley, 1984b; corrected by Fitzsimons and Harley, 1994), is less diffusive than Mg and Fe, which mainly contributes on geothermometer (Harley, 1984a), and this implies that the temperature obtained from the geothermometer is underestimated compared to pressure from the geobarometer. Therefore, the pressure condition of 0.8~1.1 GPa is estimated for the thermal peak (~1100°C) using the geobarometer (solid and dashed lines in Fig. 4.10). P-T conditions of 600~700°C and 0.4~0.6 GPa (those from A98012902P representing the higher P-T, ca. 800°C and 0.8 GPa) are obtained from element partitioning between the rims of garnet and orthopyroxene, and between the garnet exsolution and the adjacent portion of the host orthopyroxene. However, it is difficult to judge as to whether they are in equilibrium with each other or not, because retrograde reaction textures are

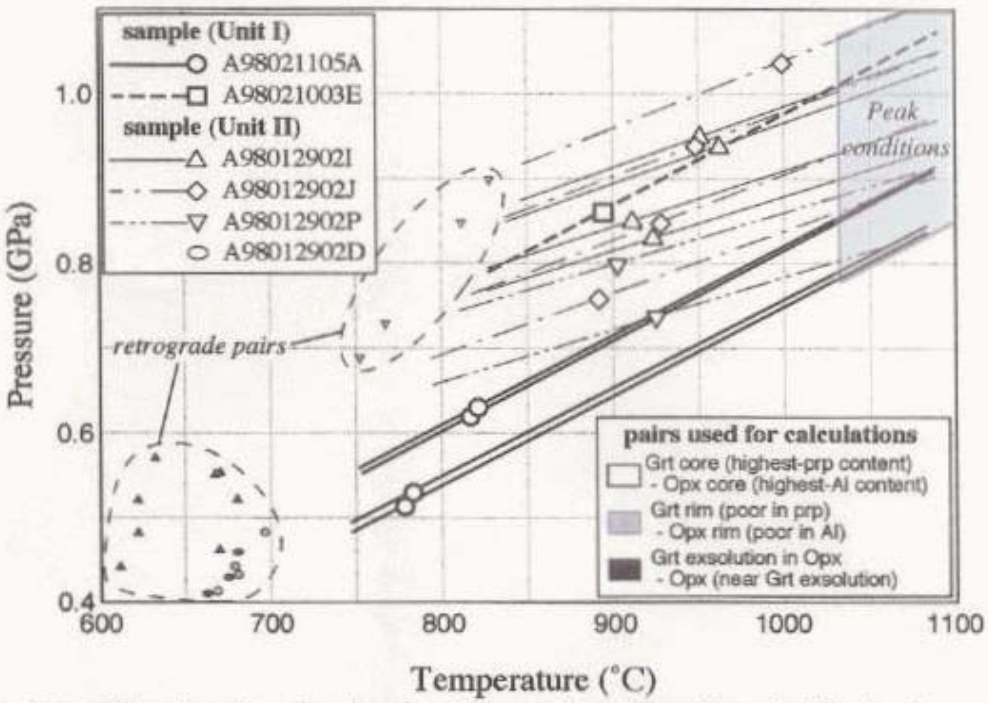

Fig. 4.10 P-T estimations for the aluminous gneisses from Tonagh Island using garnet-orthopyroxene geothermobarometer (Harley, 1984a, b). Peak conditions are extrapolated from geobarometry to the peak temperatures obtained from other method. See text in detail.

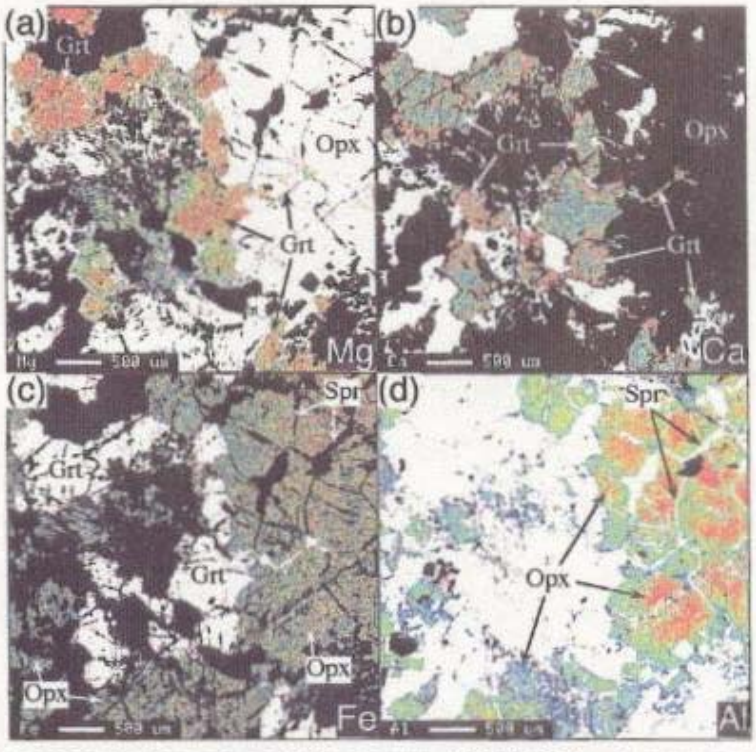

Fig. 4.11 X-ray concentration map of the sample A98021105A. A warm color represents higher-concentration (white is the highest) and a cold one is lower-concentration (black is the lowest), respectively. (a) X-ray map of Mg. (b) X-ray map of Ca. (c) X-ray map of Fe. (d) X-ray map of Al. Garnet shows compositional zoning of Mg-decreasing and Fe- and Ca-increasing toward the rim and orthopyroxene show compositional zoning of Al- and Fe-decreasing and Mg-increasing toward the rim. Exsolution of garnet and sapphirine occurs at the grain boundary of orthopyroxene.

commonly developed as will be discussed below and not only intracrystalline diffusion but also retrograde reaction modify the chemical composition. In addition, a part of garnet grain is considered to be crystallized from decomposition of orthopyroxene, suggesting reaction relation.

A variety of reaction textures are observed around sapphirine and orthopyroxene, as follows (Fig. 4.12).

(1) Sapphirine + orthopyroxene -> garnet
(2) Al-rich orthopyroxene -> garnet + Al-poor orthopyroxene
(3) Al-rich orthopyroxene -> sapphirine + Al-poor orthopyroxene
(4) Si-rich sapphirine -> garnet + Si-poor sapphirine

The reaction (1) is observed as the garnet thin film occurring between sapphirine and orthopyroxene (Figs. 4.12a and b). It can be also expressed as the combination of the reactions (2) and (4). Garnet and sapphirine exsolutions occur as thin film at the grain boundary of orthopyroxene grains (Figs. 4.12b and c) and demonstrate the reactions (2) and (3), respectively. Garnet surrounding sapphirine is observed common in the aluminous gneisses (Fig. 4.12d), and suggests the reaction (4). All these reactions are resulted from decreasing Al_2O_3 content in orthopyroxene or decreasing SiO_2 content in sapphirine accompanied by cooling (Figs. 4.4 and 4.5).

4.5 Summary

Three different modes of occurrences of sapphirine-bearing silica-undersaturated aluminous gneisses are observed in the northern part of Tonagh Island. Field occurrence and lithological feature suggest that they are not simply derived from pelitic precursor but formed through the process associated with partial melting or metasomatism. Garnet-orthopyroxene geobarometry yields the pressure condition for the thermal peak of Tonagh Island from 0.8 GPa to 1.1 GPa.

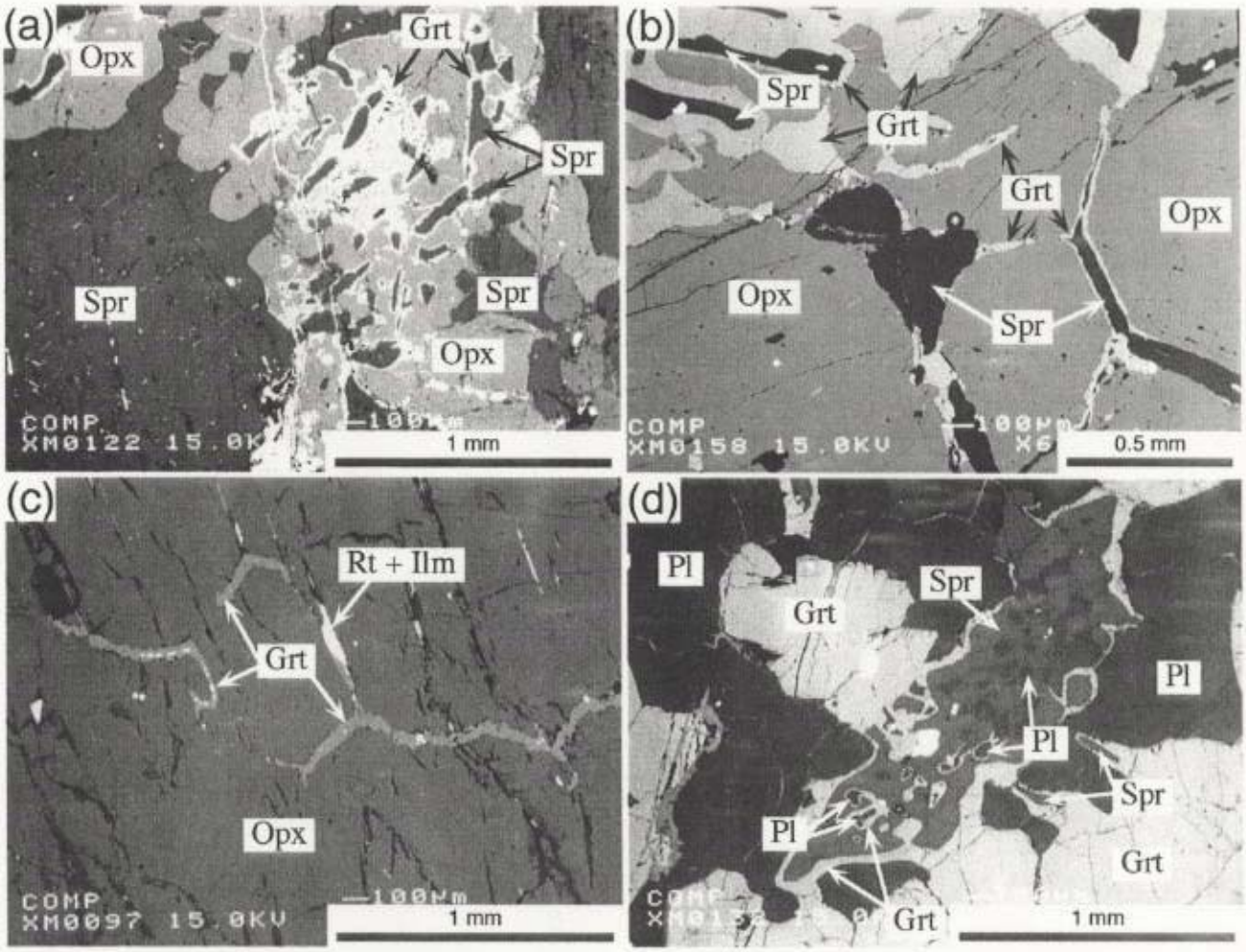

Fig. 4.12 Backscattered electron images of retrograde reaction textures in the aluminous gneisses. (a) Garnet is formed between sapphirine and orthopyroxene (A98021003E). (b) Exsolution of sapphirine after orthopyroxene, and, subsequent garnet is formed between sapphirine and orthopyroxene (A98012902D). (c) Exsolution of garnet after orthopyroxene (A98012902I). (d) Thin film of garnet surrounds sapphirine (A98012902J).

Chapter 5 Mineral Chemistry of Feldspars

Abstract: Perthitic, mesoperthitic or antiperthitic ternary feldspars occur in several rock types in the Napier Complex. The original chemical compositions of the feldspars from quartzo-feldspathic gneisses, garnet-sillimanite gneiss, garnet-orthopyroxene-bearing gneisses and sapphirine-bearing aluminous gneisses of the Mt. Riiser-Larsen area and those from sapphirine-bearing aluminous gneisses of Tonagh Island have been estimated from modal proportions and chemical analyses of host and lamellae formed by exsolution. Maximum anorthite contents in the original feldspar range from 30 mol% (an0.30ab0.49or0.21) to 14 mol% (an0.14ab0.38or0.48) to 4 mol% (an0.04ab0.16or0.80). According to ternary feldspar solvus models, the above compositions were stable at 1100°C or above at 0.8 GPa, which would be the closure temperature of intracrystalline diffusion between CaAl and (Na, K)Si in the feldspar grain, and, hence, a minimum temperature estimation for the thermal peak. The Mt. Riiser-Larsen area and Tonagh Island are both located within the highest-grade portion of the Napier Complex. Consequently, the feldspar compositions reported here suggest that temperatures in this portion of the Napier Complex have reached or exceeded 1100°C on a regional scale, and give a significant constraint on the heat source and the tectonic process of the complex.

5.1. Introduction

As discussed in the preceding chapters, the UHT metamorphism is characterized by the presence of sapphirine+quartz, spinel+quartz and osumilite-bearing mineral parageneses and inverted metamorphic pigeonite, which imply that metamorphic temperatures exceeded 1000°C in the mid to lower crust. However, these diagnostic mineral parageneses are not common. In addition, they do not give the maximum temperatures attained, but only indicate that temperatures exceeded the lower-temperature stability limits of the parageneses.

Information constraining the maximum temperatures in a wider variety of rocks is necessary. Such information is provided by perthitic to mesoperthitic ternary feldspar with high anorthite content which occurs in several rock types throughout the Napier Complex, i.e., felsic (quartzo-feldspathic) gneisses, garnet gneiss, garnet-sillimanite gneiss and sapphirine-bearing aluminous gneisses.

High Ca contents in mesoperthite from the Napier Complex have been reported by Sandiford (1985), Sheraton *et al.* (1987). Recently, ternary feldspar

solvus models are proposed based on the synthetic experiments (Seck, 1971) and the thermodynamic modeling (e.g., Ghiorso, 1984; Furhman and Lindsley, 1988; Lindsley and Nekvasil, 1989; Elkins and Grove, 1990).

This study estimates the original chemical compositions of perthitic or mesoperthitic ternary feldspars, from modal proportions and chemical analyses of host and lamellae formed by exsolution, in felsic (quartzo-feldspathic) gneisses, garnet-sillimanite gneiss and sapphirine-bearing aluminous gneisses of the Mt. Riiser-Larsen area and those in sapphirine-bearing aluminous gneisses of Tonagh Island. The estimated mineral compositions could provide temperature conditions of the thermal peak from a variety of rock types in the Napier Complex.

5.2. Thermodynamic models for the ternary feldspars

Under equilibrium condition at a given P and T, chemical potentials of albite (Ab), orthoclase (Or) and anorthite (An) components in coexisting plagioclase and alkali feldspar are equal:

$$\mu(\text{Ab in Akfs}) = \mu(\text{Ab in Pl}) \quad (1)$$
$$\mu(\text{Or in Akfs}) = \mu(\text{Or in Pl}) \quad (2)$$
$$\mu(\text{An in Akfs}) = \mu(\text{An in Pl}) \quad (3)$$

where,

$$\mu(\text{Ab in Akfs}) = \mu_0(\text{Ab in Akfs}) + RT \ln a(\text{Ab in Akfs})$$

and

$$\mu(\text{Ab in Pl}) = \mu_0(\text{Ab in Pl}) + RT \ln a(\text{Ab in Pl})$$

or, equivalently:

$$a(\text{Ab in Akfs}) = a(\text{Ab in Pl}) \quad (4)$$
$$a(\text{Or in Akfs}) = a(\text{Or in Pl}) \quad (5)$$
$$a(\text{Or in Akfs}) = a(\text{Or in Pl}) \quad (6)$$

According to Fuhrman and Lindsley (1988), activities are expressed as follows:

$$a(Ab) = \mathbf{X(Ab)} \exp \{(W_{OrAb} [2 X_{Ab} X_{Or} (1 - X_{Ab}) + X_{Or} X_{An} (1/2 - X_{Ab})] + W_{AbOr} [X_{Or}^2 (1 - 2 X_{Ab}) + X_{Or} X_{An} (1/2 - X_{Ab})] + W_{AbAn} [X_{An}^2 (1 - 2 X_{Ab}) + X_{Or} X_{An} (1/2 - X_{Ab})] + W_{AnAb} [2 X_{An} X_{Ab} (1 - X_{Ab}) + X_{Or} X_{An} (1/2 - X_{Ab})] + W_{OrAn} [X_{Or} X_{An} (1/2 - X_{Ab} - 2 X_{An})] + W_{AnOr} [X_{Or} X_{An} (1/2 - X_{Ab} - 2 X_{Or})] + W_{OrAbAn} [X_{Or} X_{An} (1 - 2 X_{Ab})]) / RT\}$$

$$a(An) = \mathbf{X(An)} \exp \{(W_{OrAb} [X_{Ab} X_{Or} (1/2 - X_{An} - 2 X_{Ab})] + W_{AbOr} [X_{Ab} X_{Or} (1/2 - X_{An} - 2 X_{Or})] + W_{AbAn} [2 X_{Ab} X_{An} (1 - X_{An}) + X_{Ab} X_{Or} (1/2 - X_{An})] + W_{AnAb} [X_{Ab}^2 (1 - 2 X_{An}) + X_{Ab} X_{Or} (1/2 - X_{An})] + W_{OrAn} [2 X_{Or} X_{An} (1 - X_{An}) + X_{Ab} X_{Or} (1/2 - X_{An})] + W_{AnOr} [X_{Or}^2 (1 - 2 X_{An}) + X_{Ab} X_{Or} (1/2 - X_{An})] + W_{OrAbAn} [X_{Or} X_{Ab} (1 - 2 X_{An})]) / RT\}$$

$$a(Or) = \mathbf{X(Or)} \exp \{(W_{OrAb} [X_{Ab}^2 (1 - 2 X_{Or}) + X_{Ab} X_{An} (1/2 - X_{Or})] + W_{AbOr} [2 X_{Ab} X_{Or} (1 - X_{Or}) + X_{Ab} X_{An} (1/2 - X_{Or})] + W_{AbAn} [X_{Ab} X_{An} (1/2 - X_{Or} - 2 X_{An})] + W_{AnAb} [X_{Ab} X_{An} (1/2 - X_{Or} - 2 X_{Ab})] + W_{OrAn} [X_{An}^2 (1 - 2 X_{Or}) + X_{Ab} X_{An} (1/2 - X_{Or})] + W_{AnOr} [2 X_{Or} X_{An} (1 - X_{Or}) + X_{Ab} X_{An} (1/2 - X_{Or})] + W_{OrAbAn} [X_{An} X_{Ab} (1 - 2 X_{Or})]) / RT\}$$

where,

$$\mathbf{X(Ab)} = X_{Ab} (1 - X_{An}^2)$$
$$\mathbf{X(An)} = X_{An} (1 + X_{An})^2 / 4$$
$$\mathbf{X(Or)} = X_{Or} (1 - X_{An}^2)$$

for the model of Fuhrman and Lindsley (1988), and

$$\mathbf{X(Ab)} = X_{Ab}$$
$$\mathbf{X(An)} = X_{An}$$
$$\mathbf{X(Or)} = X_{Or}$$

for the models of Lindsley and Nekvasil (1989) and Elkins and Grove (1990).

Excess free-energy terms (W) for ternary feldspars used in each model are summarized in Table 5.1.

Based on these equations and excess free energy terms, equilibrium plagioclase and alkali feldspar compositions, ternary feldspar solvus, are calculated for 800°C, 900°C, 1000°C, 1100°C at 0.8 GPa using the models proposed by Fuhrman and Lindsley (1988), Lindsley and Nekvasil (1989) and Elkins and Grove (1990). The results are shown in Fig. 5.1. Solvus compositions are different from each model, and the differences in 1100°C are larger than those in 800°C. In plagioclase side of the solvus, isothermal curve varies from orthoclase-rich to poor in the following order, Fuhrman and Lindsley (1988), Lindsley and Nekvasil (1989), Elkins and Grove (1990). Whereas in the alkali feldspar side, isothermal curve varies from anorthite-rich to poor in the following order, Lindsley and Nekvasil (1989), Fuhrman and Lindsley (1988), Elkins and Grove (1990).

Kroll *et al.* (1993) calculated the pressure dependencies of 15.9~18.3°C/0.1 GPa for the solvus crest and 12.3~12.9°C/0.1 GPa for the solvus limb at X_{Or} = 0.8, based on the experimental results of Elkins and Grove (1990) and Hovis *et al.* (1991).

5.3. Method to re-integrate feldspar composition

Re-integration has used to be conducted by electron microprobe analyses of area scans with a slightly defocused beam (e.g., Harley, 1985; 1986), especially for fine-scale exsolution lamellae. However, this method needs a large number of analyses to reduce uncertainties due to the differences of volumetric proportions of host and lamellae in the analyzed area. In addition, Raase (1998) reported the systematic matrix-effect error in this analyses.

In the analyzed samples, relatively coarse exsolution lamellae, up to > 10 μm in thickness, are developed, and the original mineral compositions of perthite, mesoperthite and antiperthite were re-integrated from the modal proportions and the chemical analyses of host and lamellae of exsolution. Volume proportions of host and lamellae domains of exsolution were estimated by computer image analysis of backscattered electron images. Chemical composition of unmixed host and lamellae domains of feldspars was analyzed using an electron microprobe with an wavelength-dispersive X-ray analytical system (JEOL JXA-8800M) at the National Institute of Polar Research. Focused beam was used and probe current was kept at about 8 nA with accelerating voltage at 15 kV. Oxide ZAF correction was applied to analyses.

	Fuhrman and Lindsley (1988)			Lindsley and Nekvasil (1989)			Elkins and Grove (1990)		
W_G	W_H	W_S	W_V	W_H	W_S	W_V	W_H	W_S	W_V
W_{OrAb}	27320	10.3	0.394	27320	10.3	0.3264	27320	10.3	0.3264
W_{AbOr}	18810	10.3	0.394	18810	10.3	0.4602	18810	10.3	0.4602
W_{OrAn}	47396	0	0	33415	0	0	40317	0	0
W_{AnOr}	52468	0	-0.12	43369	8.428	-0.1037	38974	0	-0.1037
W_{AbAn}	28226	0	0	14129	6.176	0	7924	0	0
W_{AnAb}	8471	0	0	11226	7.874	0	0	0	0
W_{OrAnAb}	8700	0	-1.094	19969	0	-1.095	12545	0	-1.095

Note: $W(G) = W(H) - T \cdot W(S) + P \cdot W(V)$

Table 5.1 Excess free-energy terms for ternary feldspars. Units are joules, kelvins, and bars. See detail in each paper and references therein.

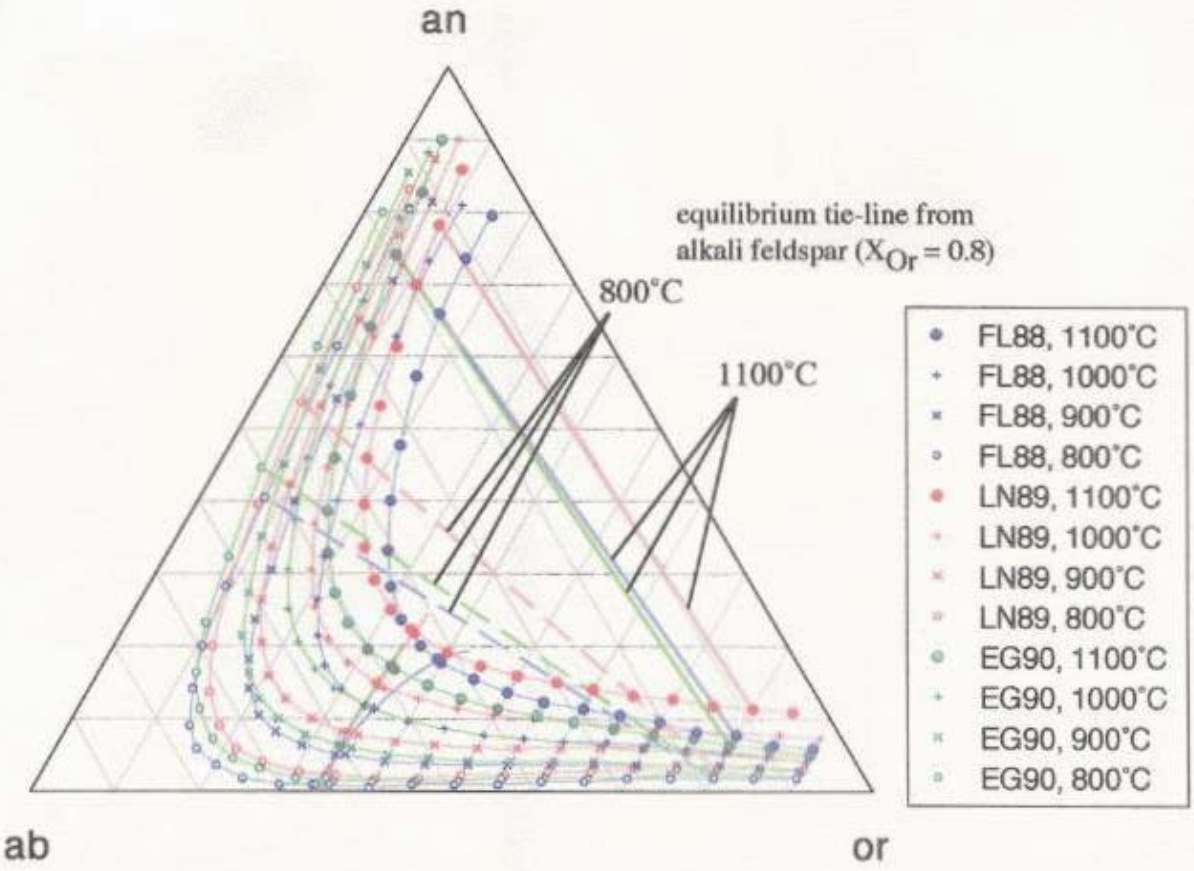

Fig. 5.1 Comparison of ternary feldspar solvus calculated for 0.8 GPa using the following models. FL88: Fuhrman and Lindsley (1988), LN89: Lindsley and Nekvasil (1989), EG90: Elkins and Grove (1990).

Synthesized pure oxides and natural minerals were used for standards. To avoid the overlapping of the host and the lamellae domains in the microprobe analysis, the analytical data with the highest anorthite and orthoclase contents were chosen for the chemical composition of plagioclase and K-feldspar domains of the exsolution, respectively.

5.4. Sample description

5.4.1. Mt. Riiser-Larsen

a) Orthopyroxene felsic gneiss (TH97010807)

It is the most common and voluminous rock types in the Napier Complex. Major constituents are quartz, plagioclase and orthopyroxene, and minor phases are apatite and ilmenite. Plagioclase sometimes contains antiperthitic exsolution lamellae (Fig. 5.3).

b) Garnet felsic gneiss (TH97020515, TH97020516, TH97020518)

It is also one of the common rock type in the complex. Major constituents are quartz, alkali feldspar (mesoperthite~perthite) and garnet, and minor phases are ilmenite, monazite and zircon. Sample TH97020518 locally contains sillimanite and pseudomorph of osumilite, which is completely replaced by the symplectite of cordierite-k-feldspar-quartz-orthopyroxene. Exsolution lamellae commonly develop in the feldspars from TH97020515 and TH97020516. Independent grain of plagioclase is not contained in the samples, but alkali feldspar is commonly surrounded by plagioclase film (Fig. 5.4a), which is also considered to be the exsolution product. In sample TH97020518, some exsolution lamellae gradually decreases toward a side of the grain edge (Fig. 5.4c).

c) Garnet megacryst-bearing feldspathic gneiss (TH97012006)

This sample is garnet megacryst-bearing portion of garnet felsic gneiss. Plagioclase and alkali feldspar (mesoperthite) constitute the rock in addition to garnet megacryst of up to over 5 cm in diameter (Fig. 5.5a). Quartz is absent near the garnet megacryst, and rounded quartz inclusion and alkali feldspar representing wetting angle against garnet and quartz are included in garnet megacryst. mesoperthitic exsolution lamellae develops in alkali feldspar, but plagioclase does not represent exsolution texture.

d) Garnet-sillimanite(-spinel) gneiss (TH97021321)

Main constituents are garnet, sillimanite, quartz, plagioclase (antiperthite), alkali feldspar (mesoperthite and perthite), and minor spinel, monazite and zircon are also subordinated. Garnet occurs as idiomorphic porphyroblast. (Fig. 5.6)

e) Garnet-orthopyroxene quartzo-feldspathic and siliceous gneisses (R98022301A, R98022301B)

It occurs as heterogeneous and relatively coarse-grained garnet and orthopyroxene-bearing gneisses and is always associated with sapphirine-bearing aluminous gneisses (R98022301D). R98022301A is quartzo-feldspathic portion composed of garnet, orthopyroxene, plagioclase (antiperthite) and quartz. R98022301B is siliceous portion composed of garnet and quartz with minor orthopyroxene and alkali feldspar (perthite). Ilmenite, monazite and zircon are also contained as minor phases. (Fig. 5.7)

f) Sapphirine-bearing gneisses (R98022301D, TH97020415, TH97020421)

R98022301D and TH97020415 are classified as quartz-bearing aluminous gneiss and is composed of sapphirine, orthopyroxene, plagioclase-alkali feldspar (antiperthite~mesoperthite~perthite) and quartz (R98022301D), and sapphirine, orthopyroxene, osumilite, plagioclase, alkali feldspar (perthite) and quartz (TH97020415), respectively. TH97020421 is composed of sapphirine, orthopyroxene and alkali feldspar (perthite), and is classified as silica-undersaturated aluminous gneiss. (Fig. 5.8)

5.4.2. Tonagh Island

Sapphirine-bearing gneisses from Tonagh Island (A98012805B, A98021003E, A98021106A)

See detailed petrography in chapter 4. Plagioclase without exsolution lamellae constitutes the main part of A98012805B, and alkali feldspar (perthite~mesoperthite~antiperthite) occurs locally as thin vein between garnet and orthopyroxene. A98021106A is composed three different types of feldspars, i.e., plagioclase (with or without antiperthitic lamellae) and two different alkali feldspars (mesoperthite and perthite). Plagioclase without exsolution lamellae and alkali feldspar (with or without exsolution lamellae) are composed in A98021003E. (Fig. 5.9)

5.5. Results and discussion

Estimated mineral compositions of feldspars from the Mt. Riiser-Larsen area and Tonagh Island are summarized in Table 5.2 and Fig. 5.2. Maximum anorthite contents of the estimated compositions at a certain orthoclase content range from 26 mol% (an0.26ab0.44or0.30) to 14 mol% (an0.14ab0.36or0.51) to 8 mol% (an0.08ab0.20or0.72), except 3 re-integrated compositions (labeled '*' of TH97021321 and A98021003E representing extremely high anorthite content as will be discussed below). They are just on the 1100°C isotherm curve of Fuhrman and Lindsley (1988), and are on 1100°C at solvus crest and ~1000°C at solvus limb of Lindsley and Nekvasil (1989), and are 1100~1200°C of Elkins and Grove (1990). These temperatures suggested from ternary feldspar solvus would be closure temperatures of intracrystalline diffusion between CaAl and (Na,K)Si in the feldspar crystal, and, hence, a minimum temperature estimations for the thermal peak. In the following, compositional features of analyzed feldspars in each sample are discussed.

5.5.1. Mt. Riiser-Larsen

a) Single antiperthitic plagioclase in orthopyroxene-bearing quartzo-feldspathic gneiss (TH97010807)

Re-integrated compositions vary from $An_{30}Ab_{50}Or_{20}$ to $An_{30}Ab_{47}Or_{23}$ (Table 5.2; Fig. 5.3), and indicate minimum temperatures of 1010 ~ 1050°C (T_{FL}). Exsolution texture is not always observed in plagioclase grains, and those without exsolution lamellae also widely occur.

b) Single mesoperthitic ~ perthitic alkali feldspar in garnet-bearing quartzo-feldspathic gneiss (TH97020515, TH97020516, TH97020518)

Re-integrated compositions range from $An_8Ab_{30}Or_{62}$ to $An_{10.5}Ab_{33}Or_{56.5}$, and suggest minimum temperatures of 1020 ~ 1070°C (T_{FL}) (Table 5.2; Fig. 5.4).

c) Mesoperthite - plagioclase disequilibrium pairs in garnet megacryst-bearing feldspathic gneiss (TH97012006)

Plagioclase without (or with a scarce amount of) exsolution lamellae and alkali feldspar constitute in matrix, and the alkali feldspar is classified into two;

Sample	position	Volume ratio of exsolution (%)		Re-integrated feldspar composition (mol%)			Minimum equilibrium temperature (°C)		
		Pl	Kfs	An	Ab	Or	T (FL)	T (LN)	T (EG)
Mt. Riiser-Larsen									
orthopyroxene-bearing quartzo-feldspathic gneiss									
TH97010807	f1	80.3	19.7	30.4	50.0	19.6	1005	1020	1084
	f2	78.4	21.6	31.8	46.8	21.4	1038	1059	1134
	f3	76.7	23.3	30.4	46.5	23.1	1049	1071	1148
garnet-bearing quartzo-feldspathic gneiss									
TH97020515	f1	30.3	69.7	8.5	28.0	63.5	1046	980	1086
	f2	37.9	62.1	10.6	32.8	56.6	1071	1018	1118
TH97020516	f1	27.3	72.7	7.7	30.2	62.1	1016	956	1049
	f2	28.5	71.5	8.0	30.9	61.1	1026	963	1055
TH97020518	f1	42.9	57.1	9.0	37.7	53.3	1030	975	1051
	f2	39.4	60.6	8.2	35.2	56.6	1030	962	1041
garnet-bearing feldspathic gneiss									
TH97012006	f1	45.6	54.4	13.5	35.7	50.8	1100	1060	1161
	f2	47.5	52.5	13.7	37.7	48.6	1094	1056	1150
	f3a	53.4	46.6	16.1	39.1	44.8	1108	1080	1176
	f3b	65.6	34.4	20.2	47.6	32.2	1070	1059	1129
	f4	63.8	36.2	19.7	46.5	33.8	1078	1065	1139
garnet-sillimanite-spinel gneiss									
TH97021321	f1-1a	69.8	30.2	26.1	43.7	30.2	1099	1110	1199
	f1-1b	79.4	20.6	29.6	49.2	21.2	1020	1037	1104
	f1-2a	12.8	87.2	7.3	23.1	69.6	1031	954	1071
	f1-2b	80.2	19.8	28.2	52.2	19.6	996	1001	1059
	f2-1	74.3	25.7	27.4	48.2	24.4	1052	1059	1130
	f2-2	51.7	48.3	20.7	32.8	46.5	1178	1161	1303
	f3-0	58.8	41.2	23.2	37.8	39.0	1150	1149	1266
	f4-0	72.9	27.1	27.4	47.0	25.6	1060	1074	1149
garnet-orthopyroxene-bearing quartzo-feldspathic gneiss									
R98022301A	f1-1	74.3	25.7	26.2	47.4	26.4	1066	1071	1144
	f1-2	69.8	30.2	25.5	45.1	29.4	1087	1095	1178
	f2-1	69.5	30.5	24.6	45.0	30.4	1089	1095	1178
	f2-2	72.3	27.7	25.2	46.9	27.9	1070	1076	1152
garnet-orthopyroxene-bearing siliceous gneiss									
R98022301B	f1	28.6	71.4	6.6	30.2	63.2	1001	926	1011
	f2	21.9	78.1	7.5	32.2	60.3	1018	949	1033
sapphirine-orthopyroxene-quartz gneiss									
R98022301D	f1	63.5	36.5	15.6	50.9	33.5	1037	1009	1066
	f2	67.8	32.2	16.6	53.7	29.7	1020	994	1045
	f3	50.1	49.9	12.5	42.1	45.4	1062	1022	1097
sapphirine-orthopyroxene-ovumilite-quartz gneiss									
TH97020415	f1	27.9	72.1	7.6	29.9	62.5	1019	954	1047
	f2	28.1	71.9	7.7	30.0	62.3	1022	956	1050
sapphirine-orthopyroxene gneiss									
TH97020421	f1	19.6	80.4	0.4	25.5	74.1	677	640	661
	f2	15.6	84.4	0.3	22.0	77.7	642	606	628
Tonagh Island									
sapphirine-orthopyroxne-garnet gneiss									
A98021106A	f1-1	55.7	44.3	15.2	43.5	41.3	1078	1049	1125
	f1-2	51.7	48.3	14.6	40.4	45.0	1090	1056	1143
	f1-3	53.6	46.4	15.8	41.9	42.3	1091	1063	1147
	f1-4	85.1	14.9	23.2	62.4	14.4	894	876	912
	f2-1	12.9	87.1	4.0	16.7	79.3	926	834	936
	f2-2	47.6	52.4	13.2	41.1	45.7	1074	1035	1116
	f2-3	55.7	44.3	16.6	43.3	40.1	1088	1064	1144
	f2-4	87.4	12.6	25.4	62.1	12.5	868	856	892
	f2-5a	46.0	54.0	13.4	36.6	50.0	1095	1055	1153
	f2-5b	48.5	51.5	14.0	38.4	47.6	1093	1057	1149
	f2-6	12.0	88.0	4.3	19.3	76.4	933	847	944
A98021003E	f1-1a	17.1	82.9	7.7	20.5	71.8	1055	970	1104
	f1-1b	37.1	62.9	16.2	29.3	54.5	1164	1124	1272
	f1-2	10.3	89.7	4.5	16.0	79.5	947	858	971
A98012805B	f1-1	42.3	57.7	5.5	42.3	52.2	952	890	942
	f1-2	47.5	52.5	5.8	46.2	48.0	953	894	940
	f1-3	37.6	62.4	5.6	38.3	56.1	958	894	954
	f2-1a	85.0	15.0	12.8	73.1	14.1	821	788	810
	f2-1b	71.3	28.7	10.8	62.8	26.4	940	896	928
	f2-2	65.6	34.4	9.9	59.1	31.0	960	914	949
	f2-3a	33.2	66.8	5.0	35.6	59.4	944	878	939
	f2-3b	64.7	35.3	9.7	58.3	32.0	963	916	953
	f3-1	57.8	42.2	8.7	54.0	37.3	941	925	966
	f3-2	60.6	39.4	9.2	54.8	36.0	977	928	968

Table 5.2 Re-intergrated feldspar compositions and estimations of minimum equilibrium temperatures. Temperature estimations are based on the following models; T(FL): Fuhrman and Lindsley (1988), T(LN): Lndsley and Nekvasil (1989), T(EG): Elkins and Grove (1990).

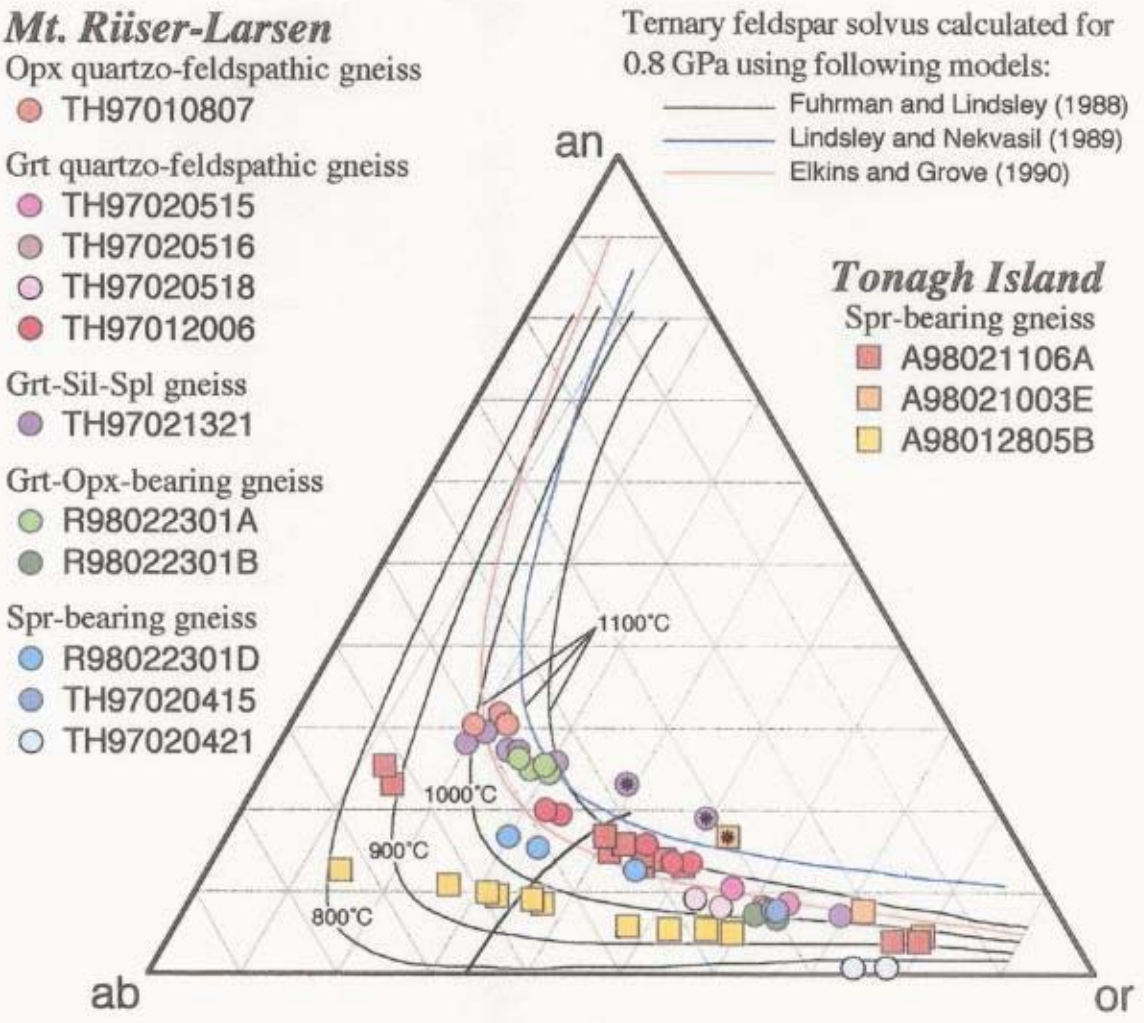

Fig. 5.2 Summary of calculated feldspar compositions. See detail in the text.

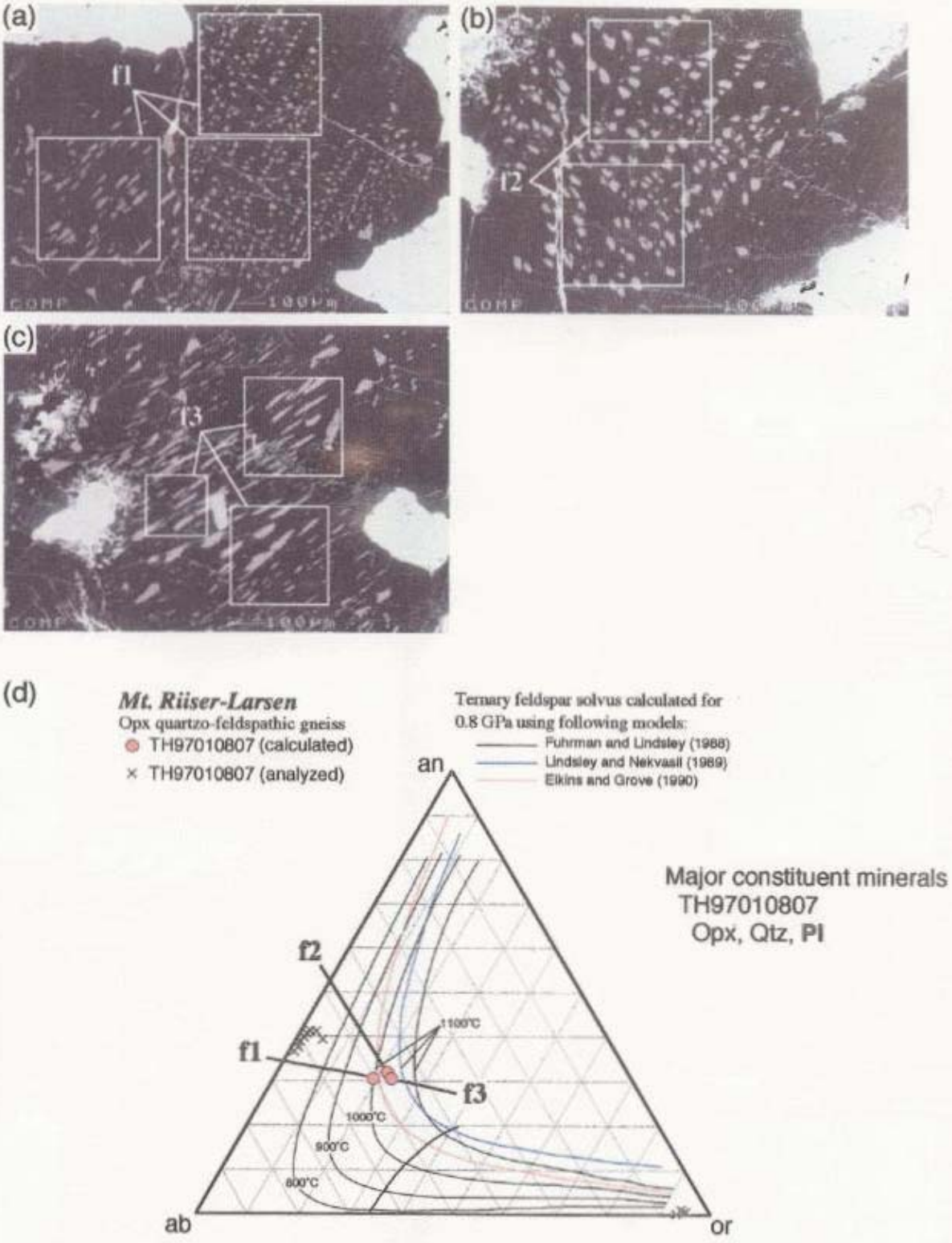

Fig. 5.3 (a), (b), (c) Backscattered electron images of the analyzed feldspars from orthopyroxene-bearing quartzo-feldspathic gneiss in the Mt. Riiser-Larsen. Dark and bright portions of the exsolution represent plagioclase and K-feldspar domains, respectively. (d) Ternary plot of the analyzed and calculated feldspar compositions.

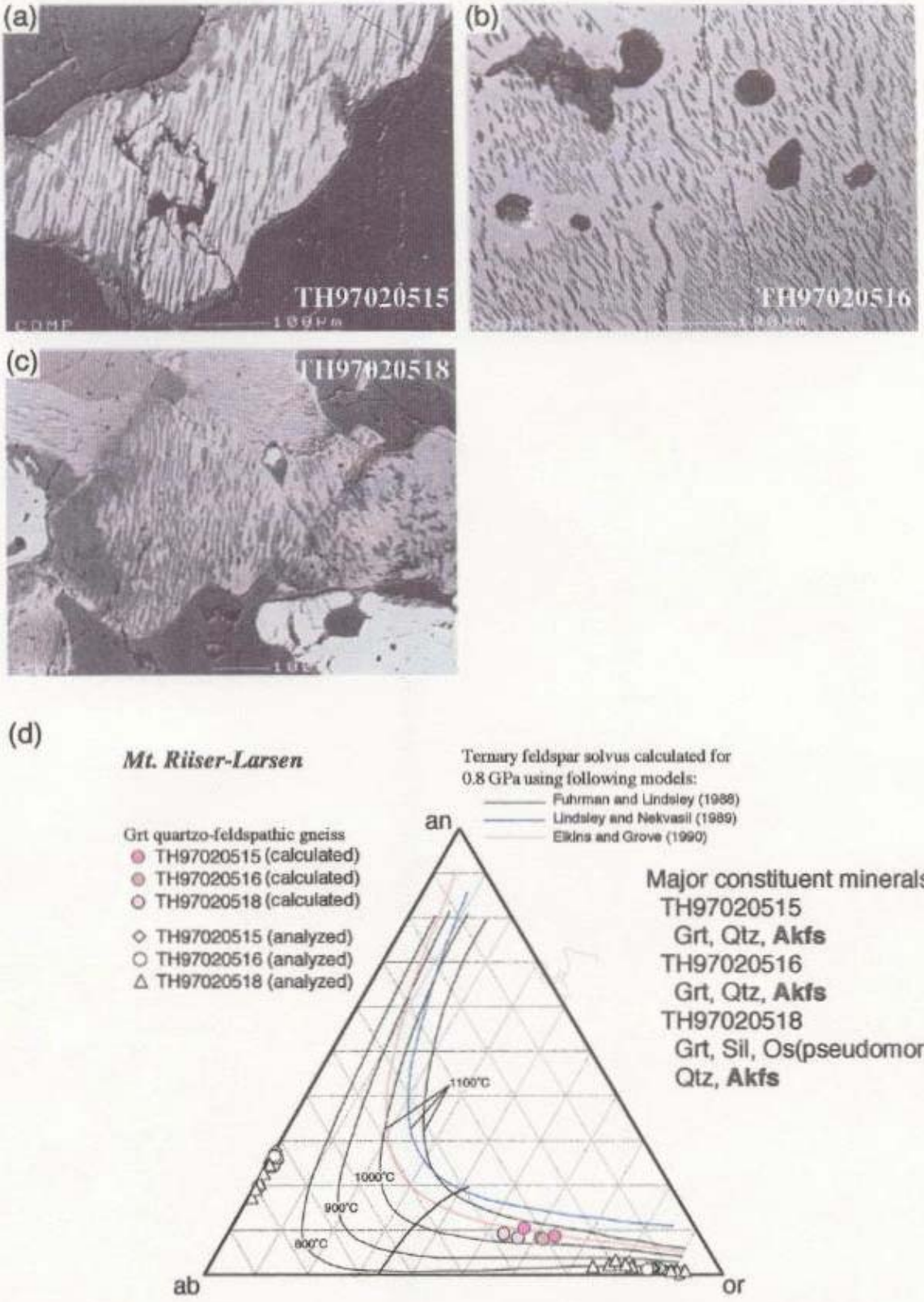

Fig. 5.4 (a), (b), (c) Backscattered electron images of feldspars from garnet-bearing quartzo-feldspathic gneisses in the Mt. Riiser-Larsen. Dark and bright portions of the exsolution represent plagioclase and K-feldspar domains, respectively. (d) Ternary plot of the analyzed and calculated feldspar compositions.

mesoperthitic alkali feldspar with one-directional strings-type exsolution lamellae (f3-a), and mesoperthitic alkali feldspar with two-directional interlocking-type exsolution lamellae (f3-b, f4) (Fig. 5.5). The occurrence of f3-a feldspar is restricted to adjacent portion of garnet-megacryst and shows slightly higher orthoclase content ($An_{16}Ab_{39}Or_{45}$) than the Akfs-2 ($An_{20}Ab_{47}Or_{33}$) in other portion of matrix. Another type of mesoperthitic alkali feldspar is included in garnet megacryst (f1, f2), and shows similar composition ($An_{14}Ab_{38}Or_{49}$ and $An_{13}Ab_{36}Or_{51}$) to f3-a. These mesoperthitic alkali feldspars suggest similar values of minimum equilibrium temperatures in the range of 1070~1110°C (T_{FL}) irrespective of the types of exsolution textures. As suggested from anorthite-albite-orthoclase ternary plot, plagioclase and mesoperthitic alkali feldspar do not show equilibrium compositions with each other.

d) Antiperthitic plagioclase, mesoperthitic and perthitic alkali feldspars in garnet-sillimanite(-spinel) gneiss (TH97021321)

Re-integrated compositions of antiperthitic plagioclase range from $An_{28}Ab_{52}Or_{20}$ to $An_{26}Ab_{44}Or_{30}$ and indicate 1000~1100°C (T_{FL}) (Table 5.2; Fig. 5.6), and those of perthitic alkali feldspar ($An_7Ab_{23}Or_{70}$) shows 1030°C (T_{FL}) for minimum equilibrium temperatures. Whereas, the mesoperthitic alkali feldspars ($An_{23}Ab_{38}Or_{39}$ and $An_{21}Ab_{33}Or_{46}$) with interlocking exsolution lamellae suggest extremely high temperatures of 1150°C and 1180°C (T_{FL}).

e) Single antiperthitic plagioclase in garnet-orthopyroxene-bearing quartzo-feldspathic gneiss (R98022301A) and single perthitic alkali feldspar in garnet-orthopyroxene-bearing siliceous gneisses (R98022301B)

Re-integrated compositions of antiperthitic plagioclase in garnet-orthopyroxene-bearing quartzo-feldspathic gneiss (R98022301A) range from $An_{26}Ab_{47.5}Or_{26.5}$ to $An_{25}Ab_{45}Or_{30}$ and indicate 1070~1090°C (T_{FL}) (Table 5.2; Fig. 5.7). Those of perthitic alkali feldspar in siliceous gneiss (R98022301B) show $An_7Ab_{30}Or_{63}$ and $An_8Ab_{32}Or_{60}$, and represent 1000°C and 1020°C.

f) Feldspars in sapphirine-bearing aluminous gneisses (R98022301D, TH97020415, TH97020421)

Feldspars in R98022301D contain various extent of perthitic or antiperthitic exsolution lamellae and show compositional zoning from antiperthitic plagioclase to perthitic alkali feldspar by means of the difference of volume ratio between plagioclase and K-feldspar domains of the exsolution.

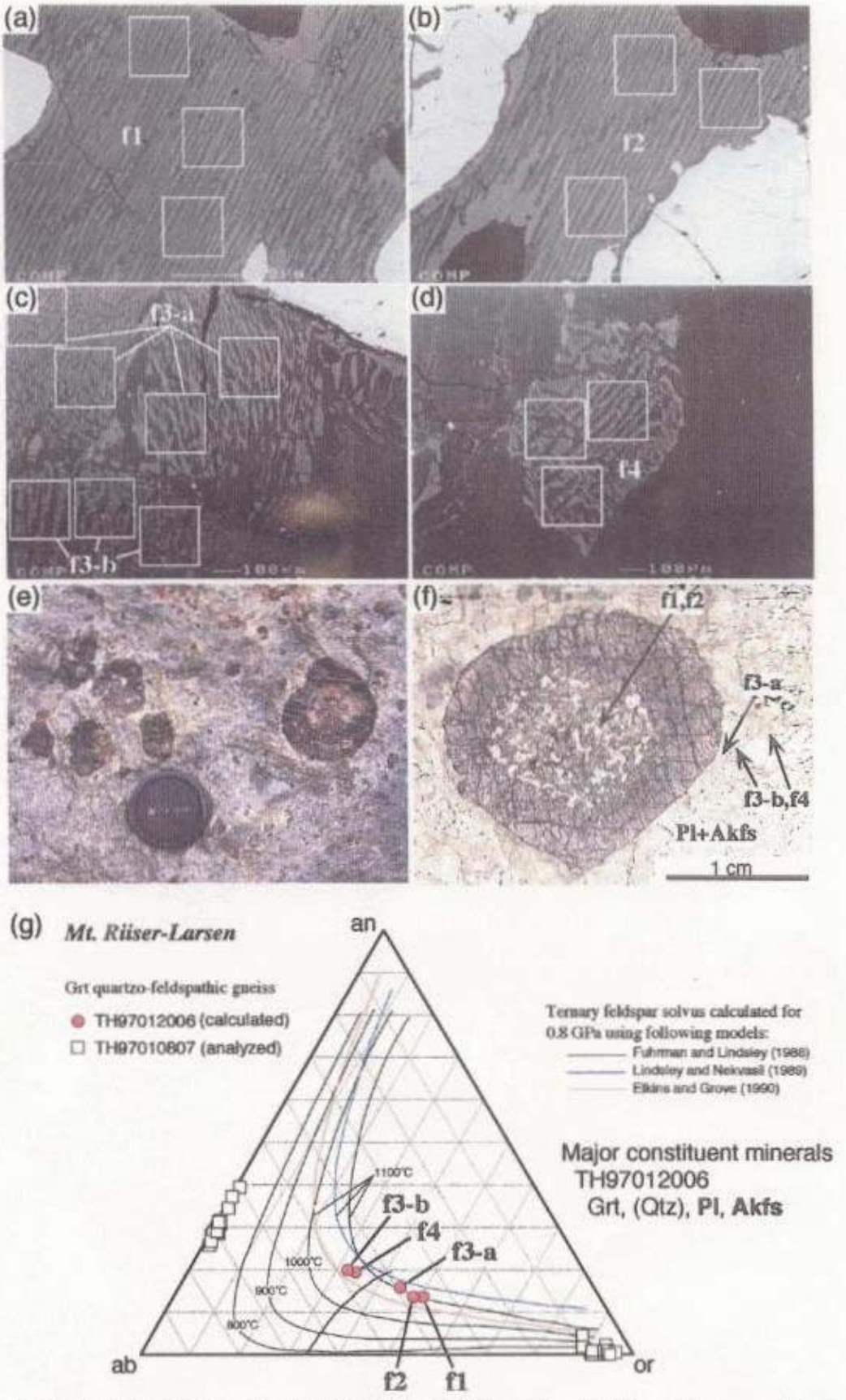

Fig. 5.5 (a), (b), (c), (d) Backscattered electron images of the analyzed feldspars from garnet-bearing feldspathic gneiss in the Mt. Riiser-Larsen. Dark and bright portions of the exsolution represent plagioclase and K-feldspar domains, respectively. (e) Field occurrence of garnet megacryst-bearing feldspathic gneiss. (f) Photomicrograph of garnet megacryst in the feldspathic matrix. Plane-polarized light. (g) Ternary plot of the analyzed and calculated feldspar compositions.

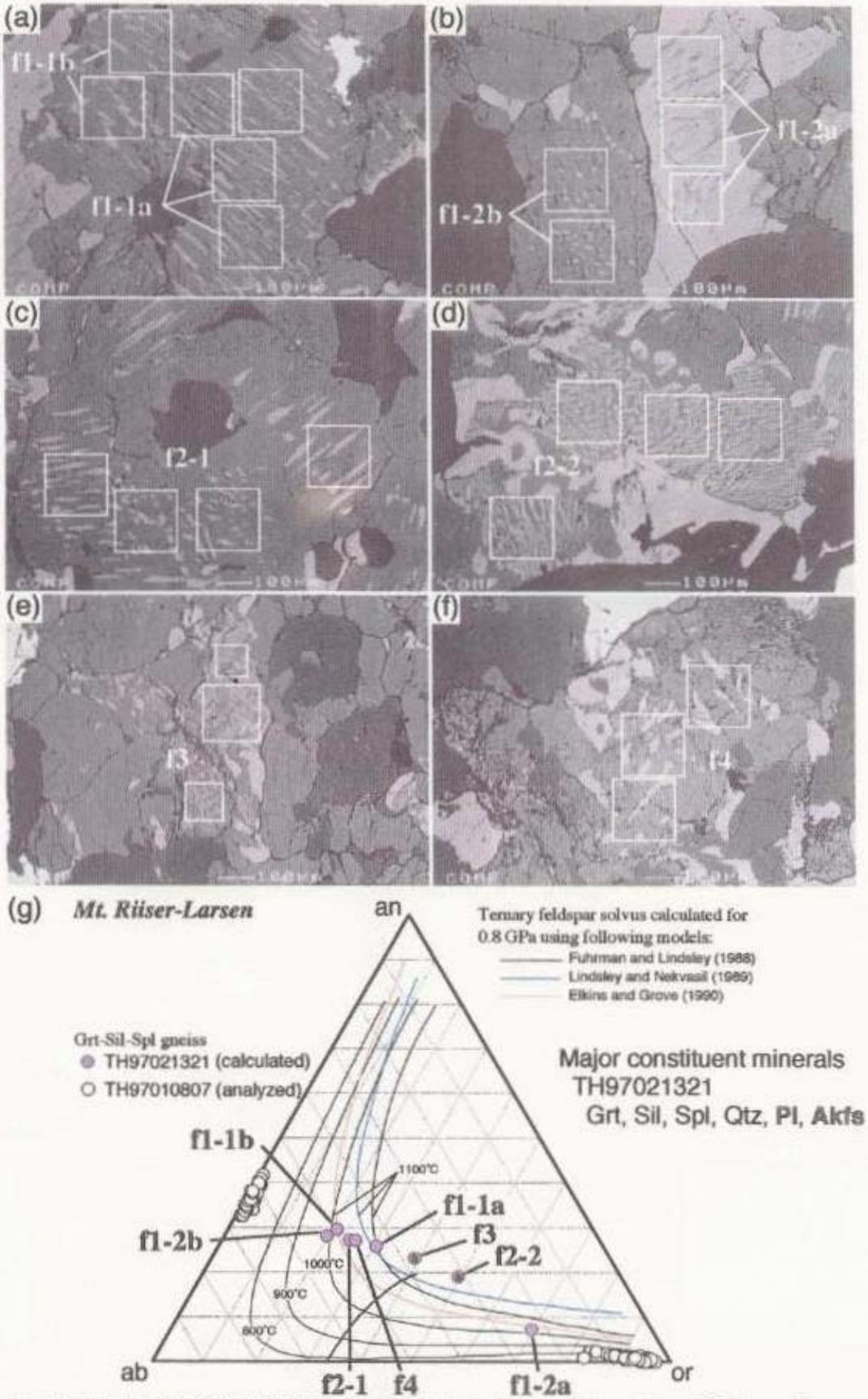

Fig. 5.6 (a), (b), (c), (d), (e), (f) Backscattered electron images of the analyzed feldspars from garnet-sillimanite(-spinel) gneiss in the Mt. Riiser-Larsen. Dark and bright portions of the exsolution represent plagioclase and K-feldspar domains, respectively. (g) Ternary plot of the analyzed and calculated feldspar compositions.

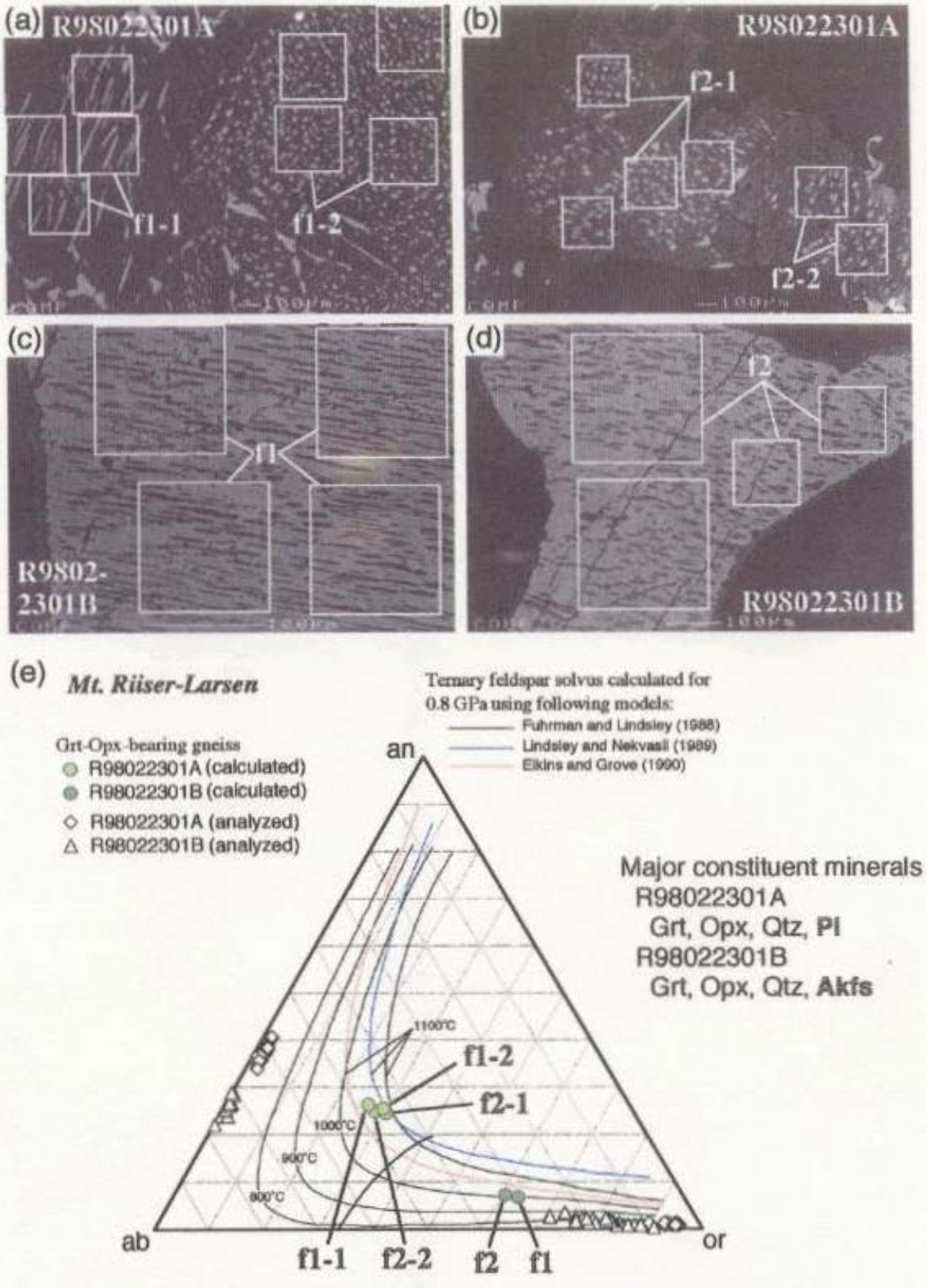

Fig. 5.7 (a), (b), (c), (d) Backscattered electron images of the analyzed feldspars from garnet-orthopyroxene-bearing quartzo-feldspathic and siliceous gneisses in the Mt. Riiser-Larsen. Dark and bright portions of the exsolution represent plagioclase and K-feldspar domains, respectively. (e) Ternary plot of the analyzed and calculated feldspar compositions.

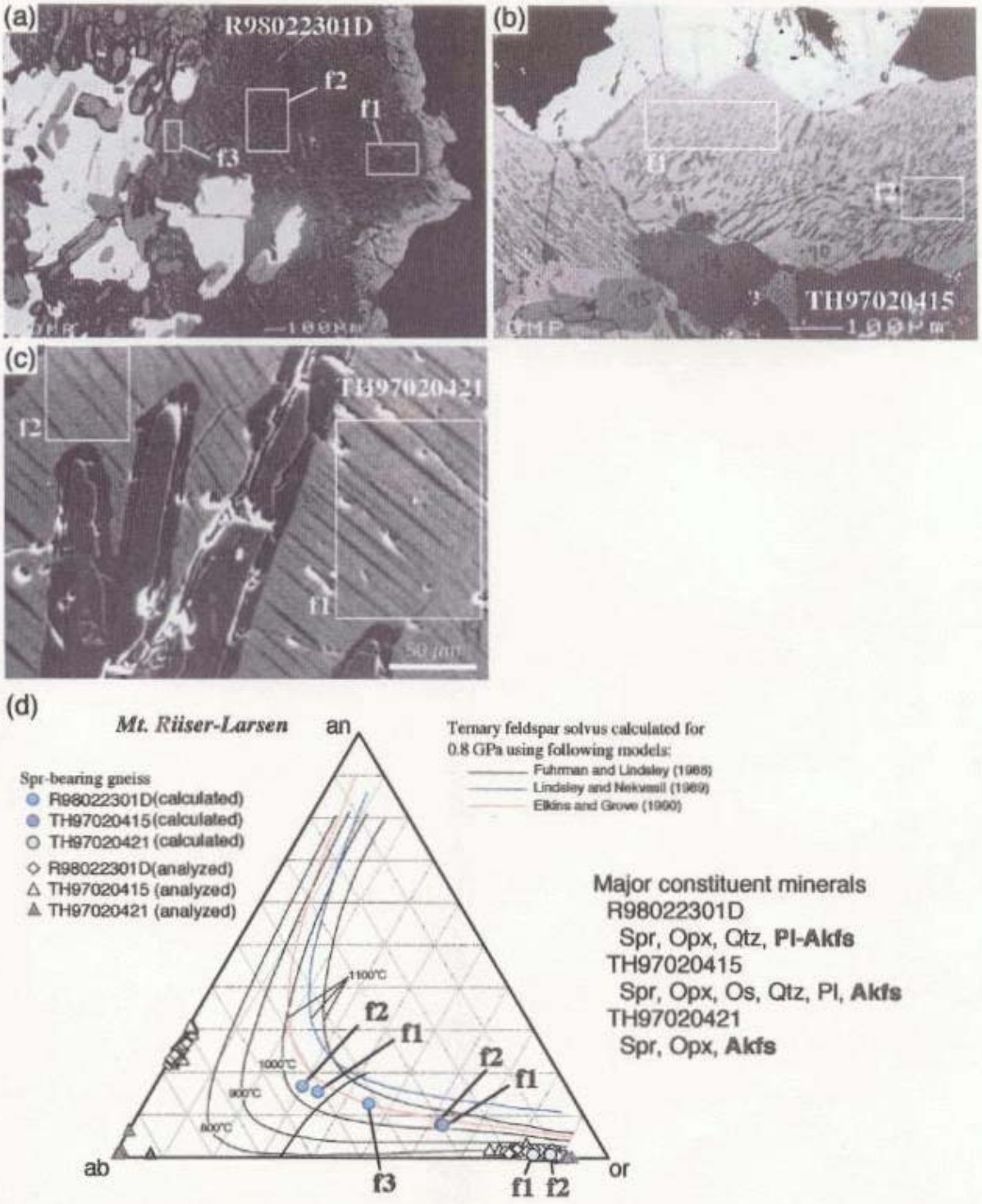

Fig. 5.8 (a), (b), (c) Backscattered electron images of the analyzed feldspars from sapphirine-bearing aluminous gneisses in the Mt. Riiser-Larsen. Dark and bright portions of the exsolution represent plagioclase and K-feldspar domains, respectively. (d) Ternary plot of the analyzed and calculated feldspar compositions.

In general, perthitic alkali feldspar distributes adjacent to quartz, and antiperthitic plagioclase occur in the opposite side, suggesting the chemical potential gradient with respect to μ_{Al} decreasing and μ_{Si} increasing within feldspar grain toward quartz. Three re-integrated compositions ($An_{16}Ab_{54}Or_{30}$ ~ $An_{13}Ab_{42}Or_{45}$) suggest 1020~1060°C (T_{FL}) (Table 5.2; Fig. 5.8).

TH97020415 contains plagioclase and perthitic alkali feldspar. Re-integrated compositions of perthitic feldspar ($An_8Ab_{30}Or_{62}$) indicate 1020°C. (Table 5.2; Fig. 5.8)

Perthitic K-feldspar in TH97020421 represents quite low anorthite content of 0.3~0.4 mol% ($An_0Ab_{22}Or_{78}$ ~ $An_0Ab_{26}Or_{74}$) mainly due to Ca-poor bulk chemical composition, and constrain the minimum equilibrium temperatures of 640~680°C. (Table 5.2; Fig. 5.8)

5.5.2. Tonagh Island

Feldspars in sapphirine-bearing aluminous gneisses from Tonagh Island (A98021106A, A98021003E, A98012805B)

Antiperthitic plagioclase, mesoperthitic and perthitic alkali feldspars constitute A98021106A. Compositional range of the re-integrated antiperthite, mesoperthite and perthite are $An_{25}Ab_{62}Or_{13}$ ~ $An_{23}Ab_{62.5}Or_{14.5}$, $An_{17}Ab_{43}Or_{40}$ ~ $An_{13}Ab_{37}Or_{50}$, and $An_4Ab_{17}Or_{79}$ ~ $An_4Ab_{19}Or_{77}$, respectively. They represent 870~890°C, 1070~1100°C, 930°C, respectively. (Table 5.2; Fig. 5.9)

A98021003E also contain plagioclase, perthitic and mesoperthitic alkali feldspars. Re-integrated compositions are $An_{4.5}Ab_{16}Or_{79.5}$, $An_8Ab_{20}Or_{72}$, and $An_{16}Ab_{29}Or_{55}$, and indicate 950°C, 1060°C and 1160°C, respectively. (Table 5.2; Fig. 5.9)

Plagioclase is the dominant feldspars in A98012805B. Antiperthitic-perthitic feldspar occurs as thin vein between garnet and orthopyroxene. It shows compositional zoning from antiperthitic plagioclase to perthitic alkali feldspar by means of the difference of volume ratio between plagioclase and K-feldspar domains of the exsolution. In general, antiperthitic plagioclase is distributed at garnet-side of the vein and perthitic alkali feldspar occurs at orthopyroxene-side, respectively, and suggesting the chemical potential gradient with respect to μ_{Al} decreasing and μ_{Si} increasing from garnet-side to orthopyroxene-side within the feldspar grain. (Table 5.2; Fig. 5.9)

In general, intracrystalline diffusion between K and Na in feldspar crystal persists significantly lower temperature than that between CaAl and

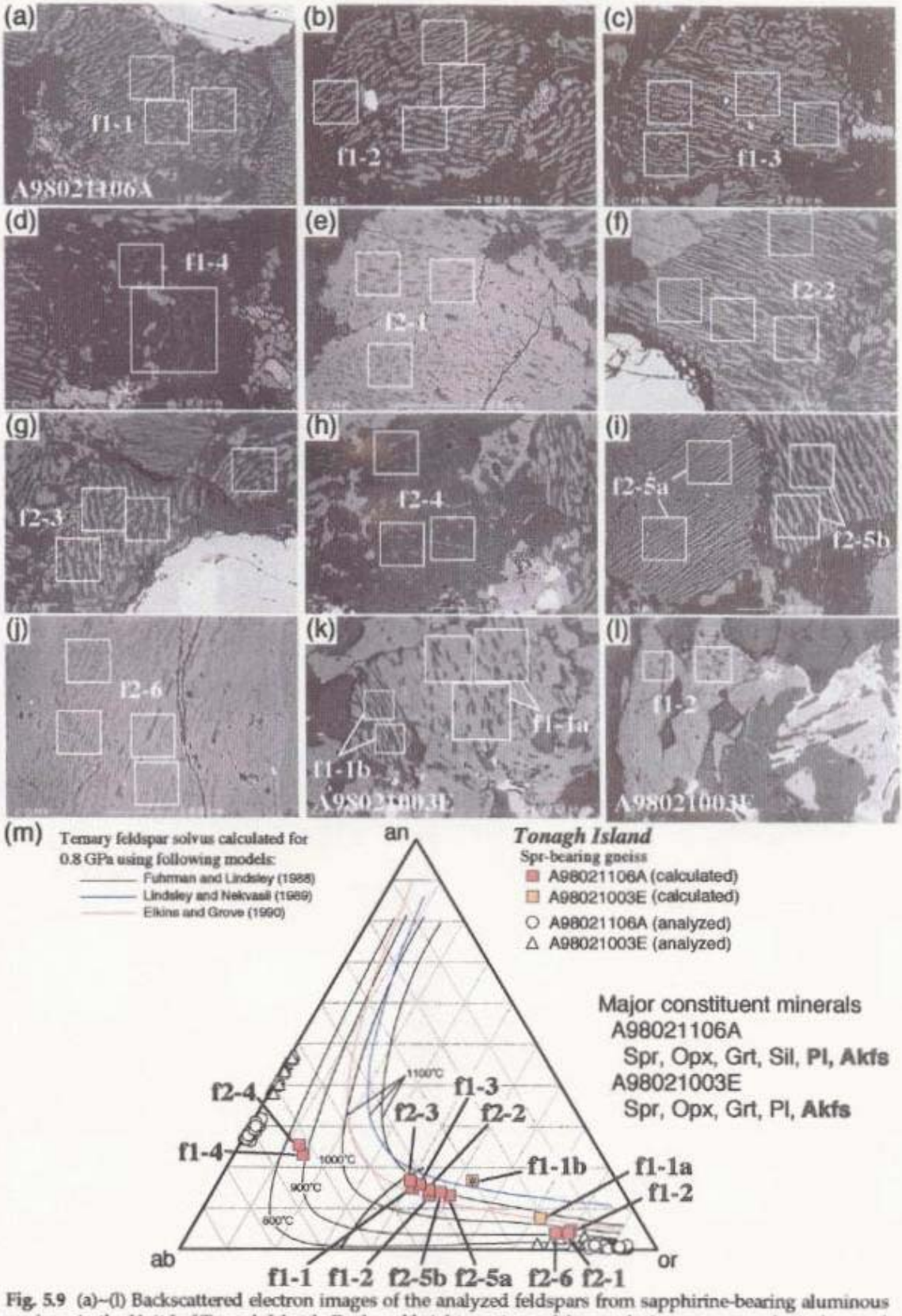

Fig. 5.9 (a)~(l) Backscattered electron images of the analyzed feldspars from sapphirine-bearing aluminous gneisses in the Unit I of Tonagh Island. Dark and bright portions of the exsolution represent plagioclase and K-feldspar domains, respectively. (m) Ternary plot of the analyzed and calculated feldspar compositions.

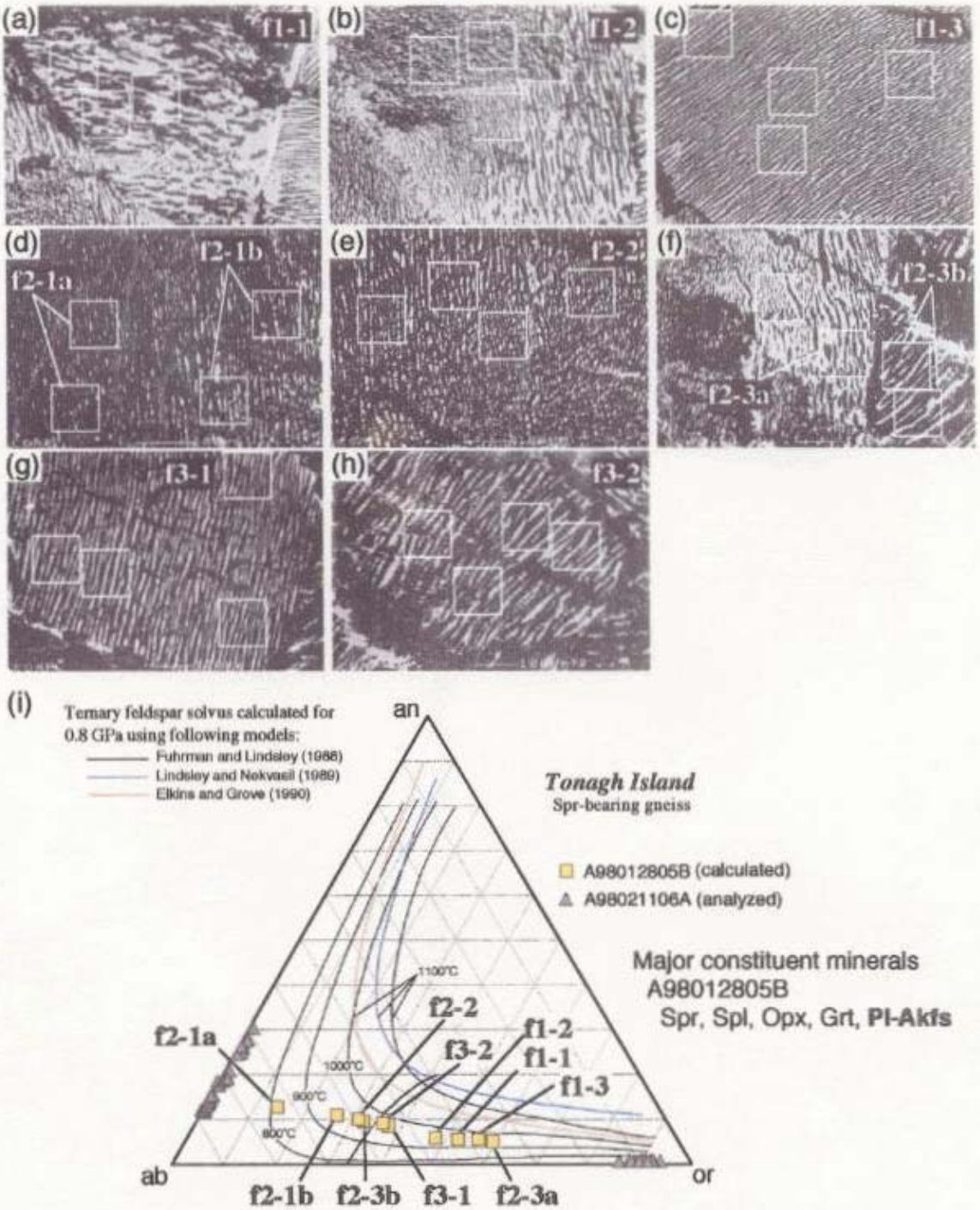

Fig. 5.10 (a)~(h) Backscattered electron images of the analyzed feldspars from sapphirine-bearing aluminous gneiss in the Unit II of Tonagh Island. Dark and bright portions of the exsolution represent plagioclase and K-feldspar domains, respectively. (i) Ternary plot of the analyzed and calculated feldspar compositions.

(Na,K)Si. The formation of the exsolution lamellae in feldspar is mainly due to the slow diffusion rate of $CaAl(Na,K)_{-1}Si_{-1}$ substitution. Hence, the re-integrated feldspar compositions suggest reliable value with respect to anorthite content, but albite and orthoclase content in feldspar at high temperature conditions is not always preserved. For this reason, equilibrium compositions of coexisting perthitic alkali feldspar and plagioclase needs to be recalculated by reversing the intercrystalline K-Na exchange (Kroll *et al.*, 1993). However, feldspars in the gneisses from the Napier Complex show complicated mode of occurrence, which may reflect the difference of crystallization temperature, retrograde recrystallization, and interaction with partial melt.

Three compositions represent minimum equilibrium temperatures of 1150~1170°C (labeled '*') and are extremely higher than those of ~1100°C estimated from many other compositions. It is possible that the peak metamorphic conditions reached such extremely high temperatures. However, another possibility is that they may be crystallized initially as a composite grain of plagioclase and alkali feldspar domains. 'f2-2' and 'f3' grains of TH97021321 (Figs. 5.6d and e) contain two-directional interlocking-type exsolution lamellae. The larger one of two-directional exsolution lamellae may be not exsolution product, but initially composite domain to the host.

For the further study, relative reliability of the different ternary feldspar models to the UHT conditions should be re-investigated experimentally.

5.6. Summary

Re-integrated mineral compositions of perthitic, mesoperthitic or antiperthitic feldspars from the Mt. Riiser-Larsen area and Tonagh Island in the Napier Complex suggest the minimum equilibrium temperatures of 1100°C or above at 0.8 GPa. The Mt. Riiser-Larsen area and Tonagh Island are both located within the highest-grade portion of the Napier Complex. Consequently, the feldspar compositions presented here suggest that temperatures in this portion of the Napier Complex have reached or exceeded 1100°C on a regional scale, consistent with the areal distribution of diagnostic mineral parageneses.

Chapter 6 Geochronology

6.1. Introduction

Harley and Black (1997) interpreted the ultrahigh-temperature metamorphism of the Napier Complex occurred at ~2.8 Ga based mainly on the SHRIMP U-Pb zircon dating. However, a number of ages around 2.5 Ga have been obtained from several localities in the high-grade region of the Napier Complex (Grew and Manton, 1979; De Paolo *et al.*, 1982; Owada *et al.*, 1994; Tainosho *et al.*, 1994; Tainosho *et al.*, 1997), and suggest UHT metamorphism may occur at that time. Recent SHRIMP dating of Shiraishi *et al.* (1997) and even that of Harley and Black (1997) obtained 2.5 Ga ages. Harley and Black (1997) interpreted the fluid ingress rather than solely by increasing temperatures promoted resetting or recrystallization at that time. To asses this interpretation, U-Th-Pb monazite and zircon datings in situ of the thin section using electron microprobe with WDS were conducted in this study. Same method has been already applied for the samples from the Napier Complex (Asami *et al.*, 1998), and 2.5~3.6 Ga have been obtained.

Theory

Crystallization age of monazite and zircon in the gneisses from the Napier Complex is estimated based on chemical analyses of U, Th and Pb using electron microprobe. Monazite and zircon contain up to several tens wt.% of ThO_2 and UO_2, and little amount of initial PbO. With the passage of time, radiogenic Pb is generated by the decomposition of Th and U within the monazite and the zircon grains as follows:

$$^{232}Th \rightarrow 6a + 4b + {}^{208}Pb$$
$$^{235}U \rightarrow 7a + 4b + {}^{207}Pb$$
$$^{238}U \rightarrow 8a + 6b + {}^{206}Pb$$

and the numbers of Pb atom produced by each radioactive decay during t years are expressed as the following equation:

$$^{208}Pb = {}^{232}Th\{\exp(\lambda_{232}\cdot t) - 1\}$$
$$^{207}Pb = {}^{235}U\{\exp(\lambda_{235}\cdot t) - 1\}$$
$$^{206}Pb = {}^{238}U\{\exp(\lambda_{238}\cdot t) - 1\}$$

where, λ is decay constant of each radioactive decay (after Steiger and Jäger, 1977):

$\lambda_{232} = 4.9475 \times 10^{-11}$ [years^{-1}],
$\lambda_{235} = 9.8485 \times 10^{-11}$ [years^{-1}],
$\lambda_{238} = 1.55125 \times 10^{-11}$ [years^{-1}],
and atomic ratio $^{238}U/^{235}U = 137.88$ (present value).

Based on this, quantitative measurements of Th, U and Pb in monazite and zircon without isotopic composition indicate the time after the crystal formation.

$$Pb(\text{measured}) = (\text{initial Pb} \approx 0) + {}^{208}Pb + {}^{207}Pb + {}^{206}Pb$$
$$U(\text{measured}) = {}^{235}U + {}^{238}U$$
$$Th(\text{measured}) = {}^{232}Th$$

Suzuki *et al.* (1991) explained in detail the method to date the monazite using electron microprobe. Th-U-Pb relations can be expressed approximately in terms of the PbO and ThO_2^* value (sum of measured ThO_2 and ThO_2 equivalent of the measured UO_2). ThO_2^* is calculated from each set of the ThO_2, UO_2 and PbO analyses (wt.%) by the following equation:

$$ThO_2^* = ThO_2 + UO_2 \cdot W_{Th}/W_U[\exp(l_{232}\cdot t) - 1] \times [\{\exp(l_{235}\cdot t) + 137.88\cdot\exp(l_{238}\cdot t)\}/138.88 - 1]$$

and t an approximate age is obtained by solving the equation:

$$PbO/W_{Pb} = ThO_2/W_{Th} \times [\exp(l_{232}\cdot t) - 1] + UO_2/W_U \times [\{\exp(l_{235}\cdot t) + 137.88\cdot\exp(l_{238}\cdot t)\}/138.88 - 1]$$

where, W is molecular weight of each oxide:

$W_{Th} = 264$,
$W_U = 270$,
W_{Pb} (for monazite) = 224,
W_{Pb} (for zircon) = 222.

6.2. Analytical technique

Analytical technique essentially follows Yokoyama and Saito (1996) which partly modifies the method of Suzuki *et al.* (1991). Mineral compositions of monazite and zircon were analyzed on an electron microprobe with wavelength-dispersive spectrometers. The operating conditions were 15kV accelerating voltage and 2 μm probe diameter. Probe current was kept at 0.2 μA and 0.4-0.5 μA for monazite and zircon, respectively. Prz correction, which modified ZAF correction provided by California Institute of Technology, was applied for the analyses. Standard materials for U and Th in this study were synthetic U_3O_8 and ThO_2 prepared by Dr. K. Yokoyama at National Science Museum. Natural and synthesized minerals were used as standards for other elements. 14 elements (P, Si, La, Ce, Pr, Nd, Sm, Gd, Dy, Y, U, Th, Pb, Ca) and 7 elements (Si, Zr, Y, Hf, U, Th, Pb) were analyzed for monazite and zircon, respectively. UMa, ThMa, PbMa were used for analyses and the overlapping of ThMa upon UMa and ThMa, YLa and ZrKa upon PbMa were corrected. The chemical compositions are more or less affected by selections of standards materials, correction methods and others. Therefore, monazite of 3.0 Ga and zircon of 1.0 Ga that had been dated by SHRIMP were analyzed as internal standards, and the analytical results were corrected as shown in Table 6.1.

6.3. Sample description

a) Sapphirine-orthopyroxene-quartz gneiss (TH97020713, TH97021326)

TH97020713 and TH97021326 are the same samples as described in chapter 3 for rocks with sapphirine in direct contact with quartz.

b) Sapphirine-orthopyroxene-osumilite-quartz gneiss (TH97011305, TH97020414, TH97020415)

TH97011305 is the same sample as described in chapter 3 for rock with cordierite formed from sapphirine and quartz.

TH97020414 is composed of sapphirine, orthopyroxene, osumilite, quartz with minor sillimanite and K-feldspar. Sapphirine is generally surrounded by cordierite-K-feldspar-quartz-orthopyroxene symplectite, which is considered to be the pseudomorph after osumilite, or by K-feldspar and does not in direct contact with quartz. TH97020414 had been preliminary dated by Dr. K.

mineral		monazite			zircon	
internal standard sample		Korea	3.0 Mnz	20414	1.0 Zrn	20414
method	U std.	(Ga)	(Ga)	(Ga)	(Ga)	(Ga)
SHRIMP (ANU)	-	1.890	3.020	-	0.994	-
WDS-prz (NSM)	UO_3	1.903	3.014	2.520	1.025	2.539
WDS-ZAF (NIPR)	UO_3	1.799	2.835	2.268	0.840	2.156
to SHRIMP age		*x 1.051*	*x 1.065*	-	*x 1.184*	-
to WDS (NSM) age		*x 1.058*	*x 1.063*	*x 1.111*	*x 1.220*	*x 1.177*
correction factor			***x 1.07***		***x 1.18***	
WDS-prz (NIPR)	UO_3	1.903	2.953	2.461	0.836	2.148
to SHRIMP age		*x 0.993*	*x 1.023*	-	*x 1.189*	-
to WDS (NSM) age		*x 1.000*	*x 1.020*	*x 1.024*	*x 1.226*	*x 1.182*
correction factor			***x 1.02***		***x 1.185***	
WDS-prz (NIPR)	U_3O_8	1.923	3.025	2.520	0.969	2.433
to SHRIMP age		*x 0.983*	*x 0.998*	-	*x 1.026*	-
to WDS (NSM) age		*x 0.990*	*x 0.996*	*x 1.010*	*x 1.057*	*x 1.044*
correction factor			***x 1.00***		***x 1.04***	

Table 6.1 Comparison of age determinations between SHRIMP and the method using WDS, and between ZAF and prz corrections for WDS, and between UO_3 and U_3O_8 for stadandard minerals of WDS. ANU: Australian National University, NSM: National Science Museum, NIPR: National Institute of Polar Research. See text in detail.

Yokoyama using the same method at National Science Museum, and the results were listed in Table 6.1.

TH97020415 is the same sample as described in chapter 5 for rock with perthitic feldspar.

c) Garnet-orthopyroxene quartzo-feldspathic or siliceous gneisses (R98022301A, R98022301B)

R98022301A and R98022301B are the same samples as described in chapter 5 for rocks with mesoperthitic and perthitic feldspars.

d) Garnet feldspathic gneiss (TH97012006)

TH97012006 is the same sample as described in chapter 5 for rock with mesoperthitic feldspar.

e) Garnet-sillimanite gneiss (TH97021321)

TH97021321 is the same sample as described in chapter 5 for rock with mesoperthitic and perthitic feldspars.

6.4. Results and discussion

Microprobe analyses of ThO_2, UO_2 and PbO together with the apparent age and ThO_2^* are listed in Table 6.2. Fig. 6.1 shows the diagram of ThO_2^* vs. PbO, and most of the measurements fall near 2.5 Ga line with some analyses indicate younger ages. Fig. 6.2 illustrates the histogram of apparent ages for analyzed monazite and zircon grains in gneisses from the Mt. Riiser-Larsen area. Older ages than 2.5 Ga which have been reported by previous SHRIMP dating of the Napier Complex (Black *et al.*, 1986; Harley and Black, 1997) are not obtained in the analyses. Several monazite and zircon grains enclosed within osumilite in TH97020414 (Figs. 6.3a and b) also represent 2.3-2.5 Ga. 2.7-2.9 Ga are obtained only for three zircon grains (5 spots) in TH97020713.

Very few of the older age than 2.5 Ga suggest that the monazite and the zircon grains of the analyzed samples are completely recrystallized at 2.5 Ga. The analyzed samples are composed mostly of UHT minerals, i.e., sapphirine, high-Al orthopyroxene, osumilite and mesoperthite, with minor amounts of garnet, quartz and plagioclase which are not necessarily crystallized at UHT stage. A number of pre-2.5 Ga SHRIMP ages have been reported from the quartzofeldspathic gneisses (Black *et al.*, 1986; Harley and Black, 1997), and are considered that relatively large amounts of quartz with plagioclase, garnet and

sample	mineral assemblage	mineral	correc-tion	n.	average age (Ga)	s.d.	note
TH97011305	Spr-Opx-Os-Qtz	Mnz	prz	26	2.48	0.07	
TH97020713	Spr-Opx-Pl-Qtz	Zrn	prz	10	2.65**	0.18	bimodal
TH97021326	Spr-Opx-Os-Qtz	Zrn	prz	8	2.52	0.06	
TH97020414	Spr-Opx-Os-Qtz	Mnz	prz	12	2.55	0.07	
		Mnz	ZAF	39	2.47	0.05	
		Zrn	prz	14	2.48	0.05	
		Zrn	ZAF	74	2.44	0.08	
TH97020415	Spr-Opx-Os-Pl-Akfs-Qtz	Mnz	ZAF	9	2.50	0.03	
		Zrn	ZAF	8	2.49	0.06	
TH97020416	Spr-Grt-Akfs-Qtz	Mnz	ZAF	3	2.51	0.03	
		Zrn	ZAF	29	2.40	0.08	
TH97012006	Grt-Pl-Akfs	Mnz	ZAF	21	2.30	0.25	
		Zrn	ZAF	14	2.40	0.04	
TH97012909	Grt-Opx-Pl-Akfs	Zrn	ZAF	3	2.39	0.07	
R98022301A	Grt-Opx-Pl-Akfs-Qtz	Zrn	ZAF	5	2.45	0.06	
		(Zrn	*ZAF*	*71*	*2.37**	*0.20*	*) low Pb*
R98022301B	Grt-Opx-Qtz	Mnz	ZAF	6	2.52	0.03	
		(Zrn	*ZAF*	*47*	*2.41**	*0.30*	*) low Pb*
R9802301C	Spr-Opx-Pl-Akfs-Qtz	Zrn	ZAF	28	2.43	0.07	
TH97010610	Spr-Opx-Pl-Qtz	*(Zrn*	*ZAF*	*16*	*2.60**	*0.42*	*) low Pb*

Table 6.2 Average values and standard deviations (s.d.) of age determinations. n.: numbers of analyses. *: analyses of low Pb content less than 0.1 wt.%, containing considerable uncertainties. **: bimodal age distributions of 2.5 and 2.8 Ga.

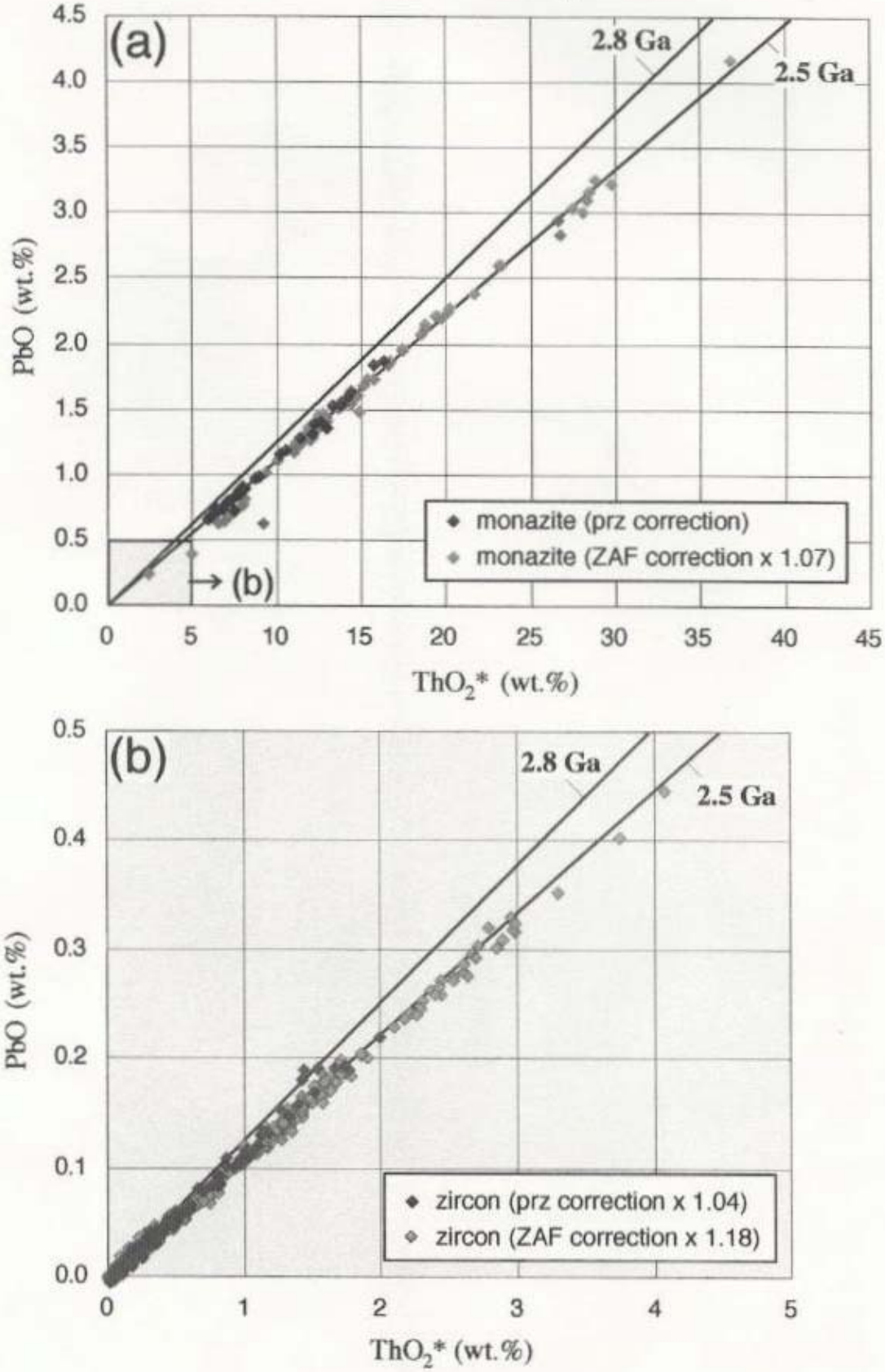

Fig. 6.1 ThO_2*-PbO plot for whole analyzed monazite and zircon grains. See detail in the text.

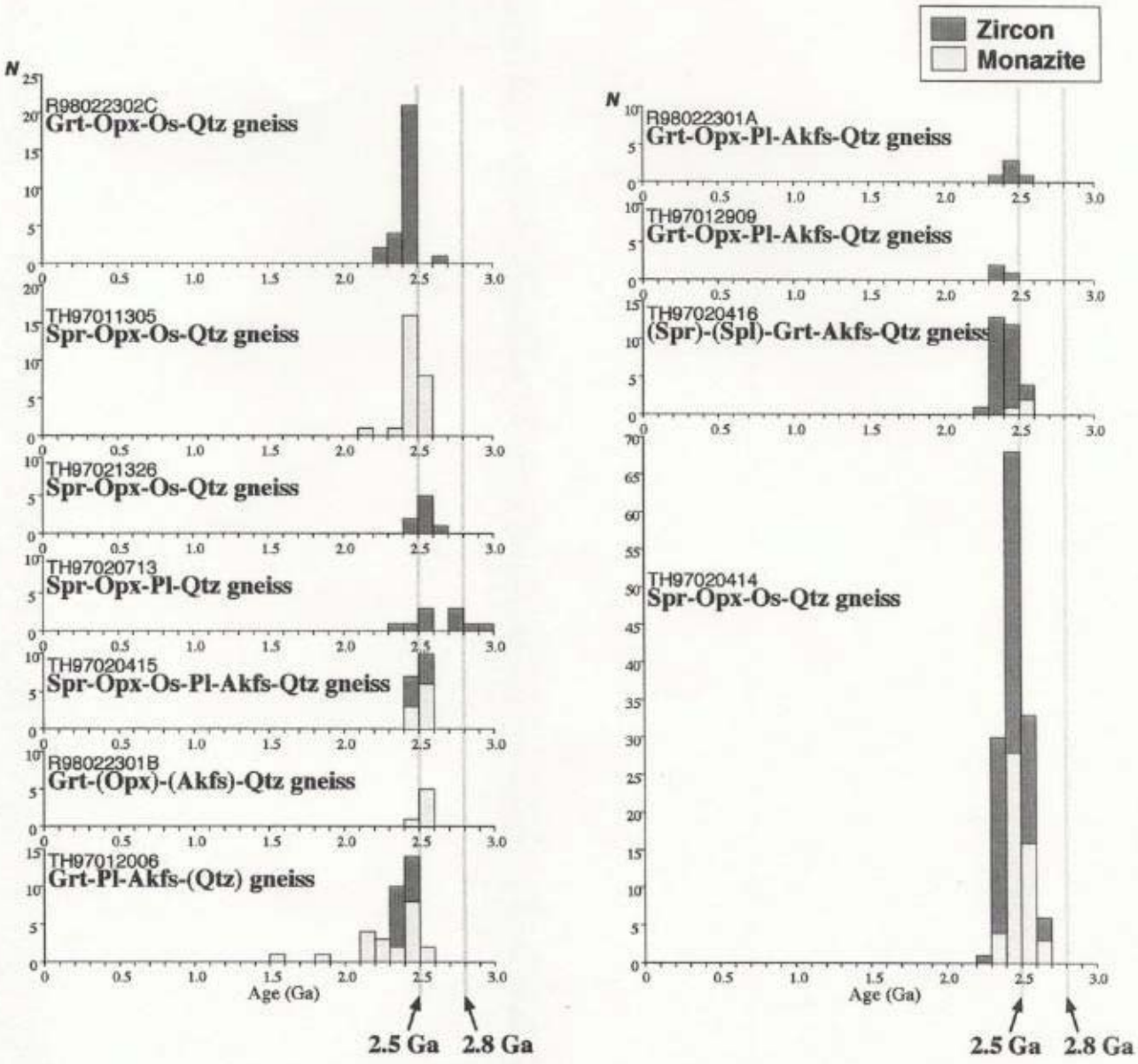

Fig. 6.2 Histograms of apparent ages for analyzed monazite and zircon grains in ultrahigh-temperature gneisses from the Mt. Riiser-Larsen area in the Napier Complex.

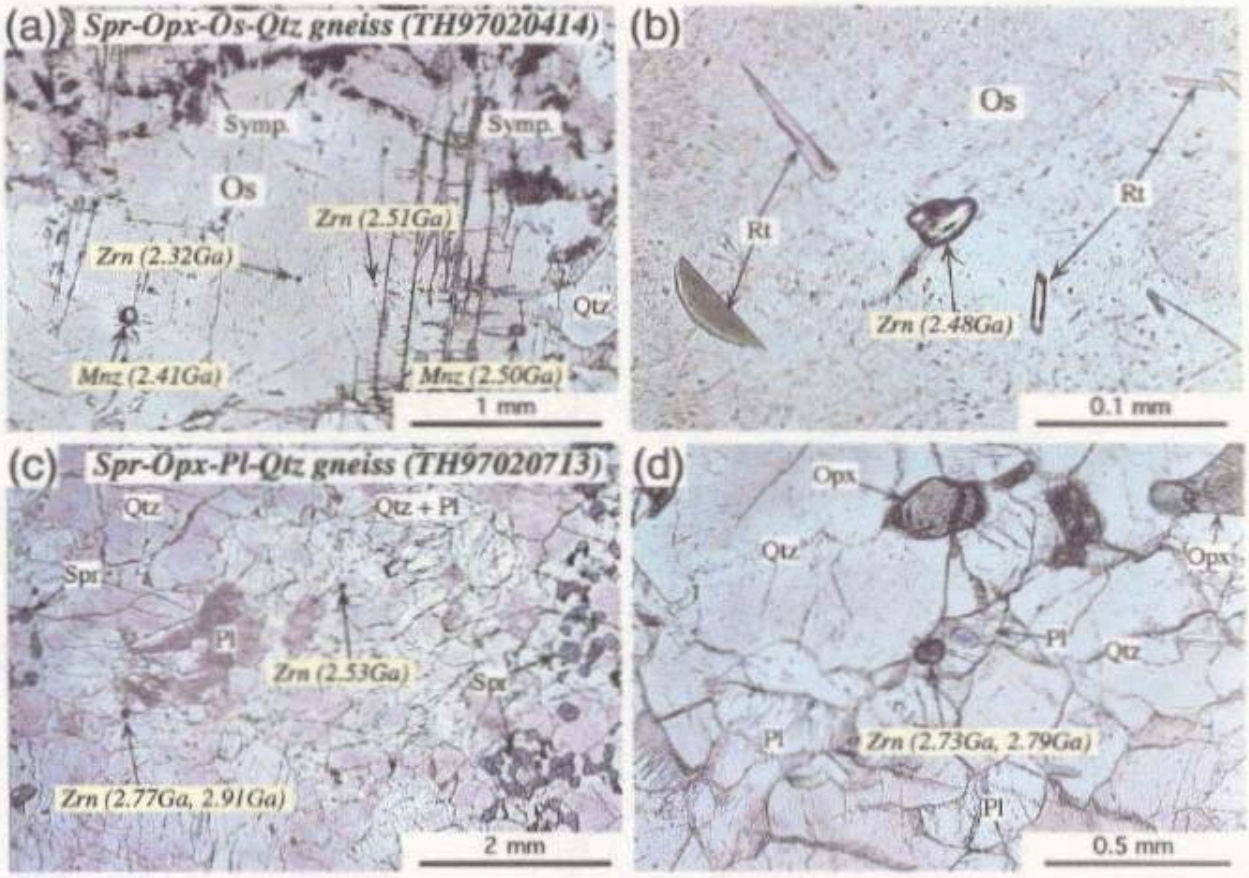

Fig. 6.3 Photomicrograph of the analyzed monazite and zircon grains. Plane-polarized light. (a) Monazite and zircon grains showing 2.3~2.5 Ga which enclosed within osumilite in sapphirine-orthopyroxene-osumilite-quartz gneiss (TH97020414). (b) Close up view of another zircon grain in osumilite representing 2.5 Ga (TH97020414). (c) Zircon grains showing 2.7~2.9 Ga and 2.5 Ga in sapphirine-orthopyroxene-plagioclase-quartz gneiss (TH97020713). (d) Close up view of another zircon grain representing 2.7~2.8 Ga (TH97020713).

orthopyroxene preserve the pre-UHT zircon grains metastably. In addition, SHRIMP dating needs relatively coarse grain due to its coarse probe diameter compared with microprobe analysis. Core of coarse zircon grains possibly preserves the pre-UHT compositions. Harley and Black (1997) interpreted 2.8 Ga as the UHT stage and 2.5 Ga as recrystallization stage promoted by fluid ingress. However, the samples dated here show no evidence of fluid ingress, and preserve the UHT mineral assemblages completely. For this reason, the author insists the 2.5 Ga as the UHT stage. Meaning of the 2.8 Ga and the relationship to the 2.5 Ga in the Napier Complex will be discussed in the next chapter.

Chapter 7 Implications for Tectonic Process of the Napier Complex

7.1. Metamorphic conditions

7.1.1. Prograde metamorphism

Ellis (1987) discussed that the quartzo-feldspathic gneiss of strongly depleted in heavy rare earth elements in the complex requires garnet in the residue from partial melting at 0.8-1.5 GPa, and that these pressures could only be realized in thickened crust. Based on this, he proposed that the Napier Complex could have formed in an orogenic cycle involving thickened crust, analogous to either Himalayan or Andean belts, and that the Napier Complex represents lower part of a doubly thickened crustal segment. Harley (1989; 1991) also suggested that the isobaric cooling obtained for the Napier Complex was resulted from extension of thickened crust.

As described previously, most of the constituent minerals in the UHT metamorphic rocks of the Napier Complex are recrystallized near the peak conditions, and few relict minerals are observed in the gneisses. For this reason, few information on the pre-peak evolutions of the Napier Complex is estimated. Motoyoshi and Hensen (1989) discussed that the sapphirine-quartz-orthopyroxene symplectite from Mt. Riiser-Larsen is a pseudomorph after cordierite, and suggested that compressional counterclockwise P-T path for the prograde metamorphism. This P-T path is contrary to the crustal thickening model proposed by Ellis (1987) and Harley (1989; 1991). Harley and Black (1997) interpreted that the rocks reported by Motoyoshi and Hensen (1989) which had experienced relatively low pressure conditions was interleaved in the main body of the Napier Complex which had experienced clockwise P-T path during crustal thickening.

The author should emphasize here that the essential factor to cause the ultrahigh-temperature metamorphism is the rocks with dry chemical composition. According to the experimental results of Whitney (1975 Fig. 7.1), quartzo-feldspathic rock is considered to be completely molten before attaining the UHT condition, if sufficient amount of H_2O is provided, from 1.5 wt.% (composition R1 in Fig. 7.1) to 4.0 wt.% (composition R6). If not completely molten, significant amounts of partial melt is considered to be produced. For this reason, dehydration prior to the UHT metamorphism is essential.

A few processes can generate the completely anhydrous quartzo-feldspathic rocks, and are summarized in Fig. 7.2. Dehydration melting and

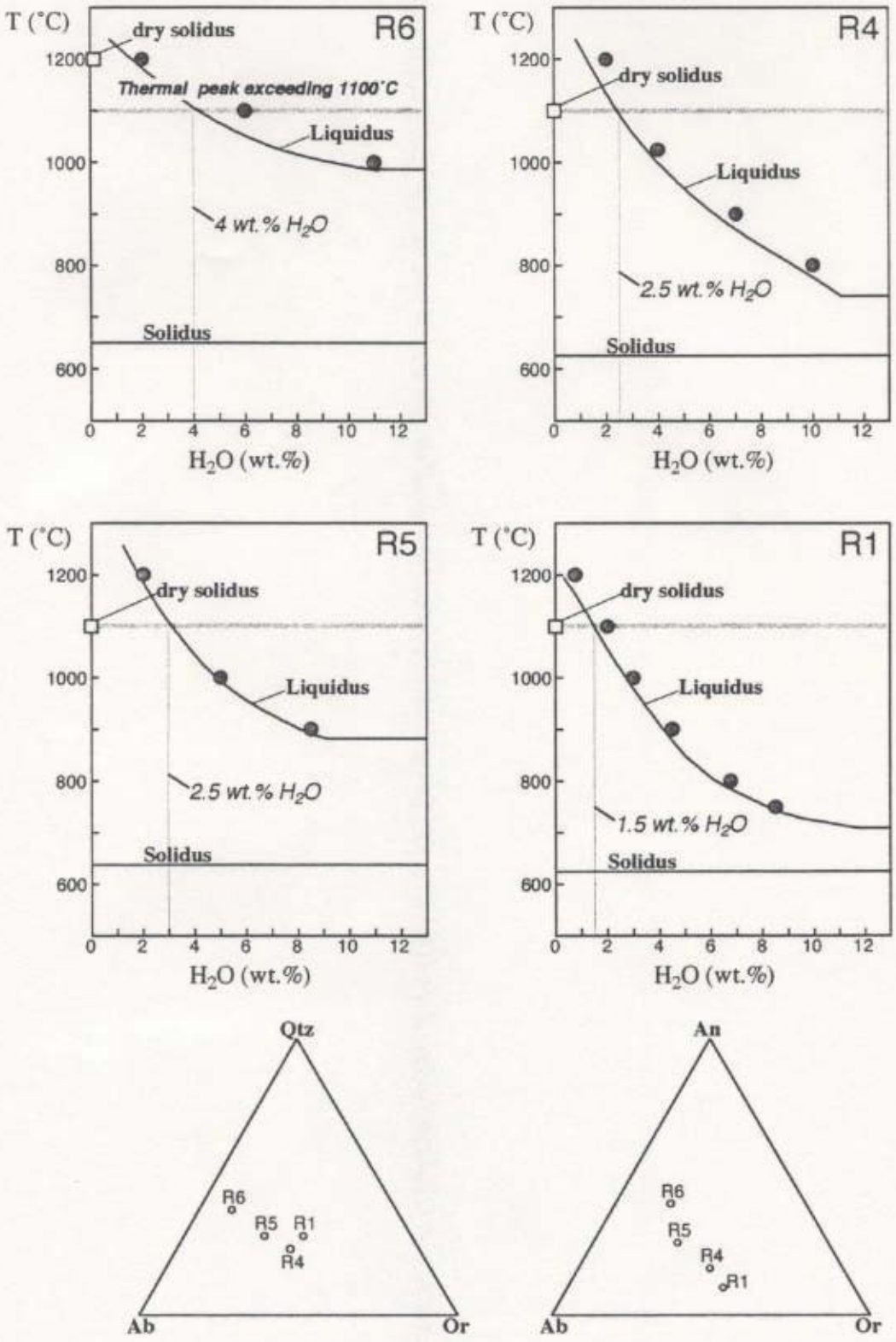

Fig. 7.1 Experimentally determined solidus and liquidus temperatures versus H_2O (wt.%) at 0.8 GPa for various synthetic granite compositions (Whitney, 1975).

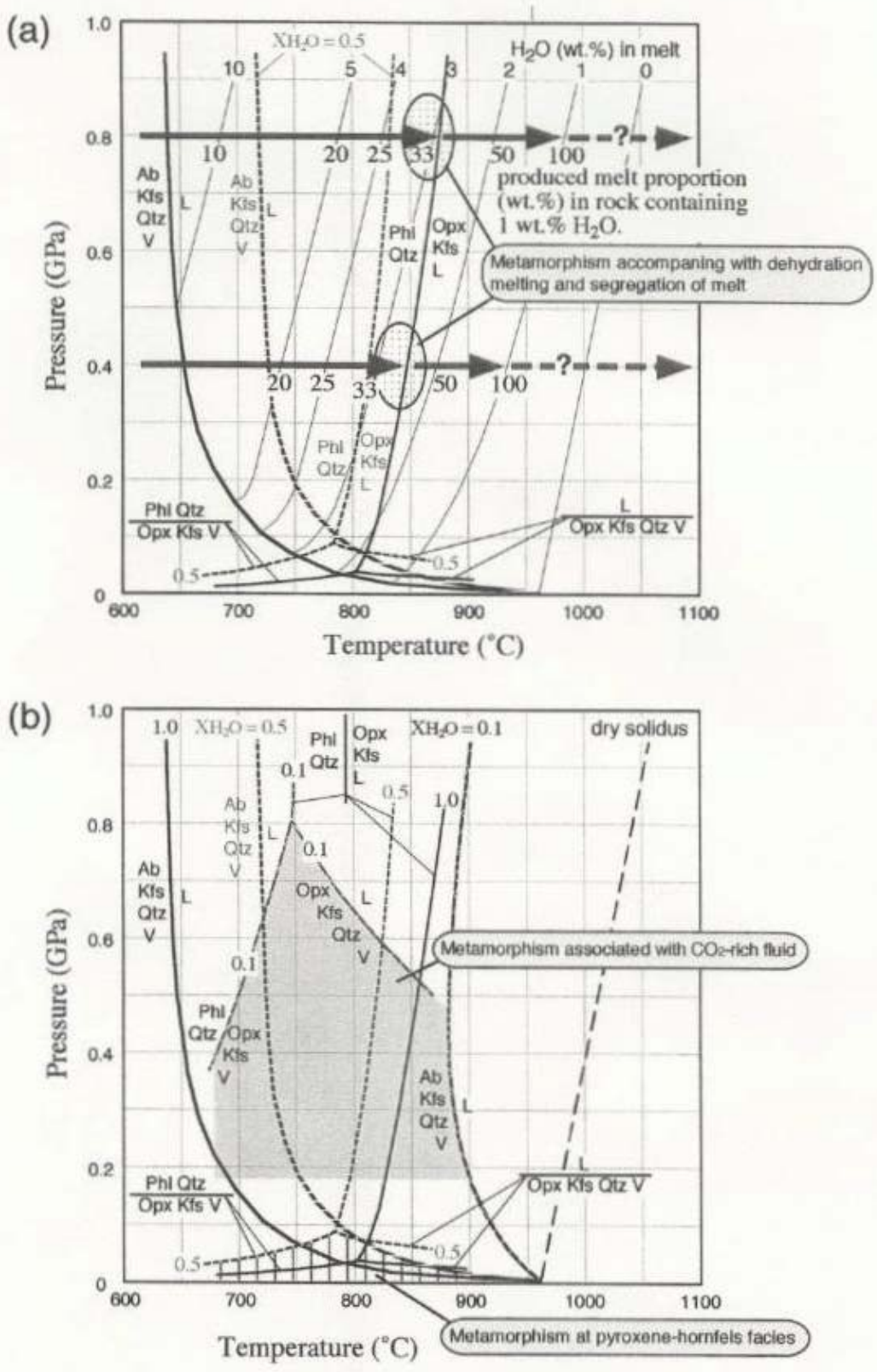

Fig. 7.2 Possible dehydration processes prior to UHT metamorphism. (a) Dehydration melting of biotite, and subsequent melt segregation. (b) Metamorphism associated witj CO_2-rich fluid and that of pyroxene-hornfels. Data sources: Newton, 1990; Ebadi and Johannes, 1991; Holtz and Johannes, 1994; and see references therein.

subsequent segregation of produced melt should be common process under deep crustal process. In Fig. 7.2a, biotite dehydration melting occurs at 800-900°C and 30-40 wt.% of felsic melt is produced from the granitic rock with 1wt.% H_2O (equivalent to 20 wt.% of biotite). If temperature increases without melt segregation, the rock is completely molten. Therefore, melt segregation at 800~900°C is needed. Other processes are dehydration without partial melting at low-pressure condition (metamorphism of pyroxene-hornfels facies) or dehydration accompanied by influx of CO_2-rich fluid (charnockitization) (Fig. 7.2b). It is also difficult to achieve regional pyroxene-hornfels facies conditions. Therefore, the influx of CO_2-rich fluid (charnockitization), for instance, is presumed for the dehydration process.

7.1.2. Peak metamorphic conditions

As discussed in chapters 3, 4 and 5, the peak conditions of Mt. Riiser-Larsen and Tonagh Island are estimated >1100°C, 0.6 ~ 1.1 GPa and fluid-free conditions. Mt. Riiser-Larsen and Tonagh Island are about 50 km away from each other. In the Mt. Riiser-Larsen area, the pressure condition is slightly different (0 ~ 0.3 GPa = 0 ~ 10 km in depth) between the areas divided by shear zone, and the temperature is similar to each other. Harley and Hensen (1990) summarized that high-grade region indicated by the occurrence of sapphirine+quartz suggesting >1030°C exposes 100 x 50 km in extent. These suggest that the high-grade region of at least 100 km x 50 km (= 5000 km^2) area was heated over 1030°C, possibly 1100°C. >1100°C was also suggested by high Al_2O_3 content in orthopyroxene (Harley and Motoyoshi, 1997). Based on these, the heat source of the UHT metamorphism of the Napier Complex must contains enough thermal budget to heat 1100°C over an such areal extent, and in addition, hydrous fluid must not be introduced into the gneiss from the heat source. The possible heat source to cause the UHT metamorphism of the Napier Complex will be discussed in the section 7.2.

7.1.3. Retrograde metamorphism

Retrograde process was discussed by Harley (1985) based on garnet-orthopyroxene geothermobarometry. He concluded the isobaric cooling after the UHT conditions. Retrograde reaction textures observed in the UHT rocks are also consistent with the isobaric cooling. Harley (1985) and Sheraton *et al.* (1987) suggested the slow cooling rate from 1000~900°C to 600~700°C for 300 Ma. However, as will be discussed in the next section 7.2., high temperature

conditions cannot continue for such a long period and rather rapid cooling is deduced.

7.2. Thermal modeling of ultrahigh-temperature metamorphism

7.2.1. Proposed tectonic processes of the Napier Complex

As described above, no direct evidence is obtained for the tectonic process and the heat source of the Napier Complex. Intrusion of anorthosite body, which is occasionally present as thin layers in the complex, is proposed for the heat source of the UHT metamorphism (Sheraton *et al.*, 1980; Grew, 1980), which is analogy to the common association of anorthosites with charnockites and with osumilite-bearing rocks. In contrast, it is interpreted that the Napier Complex is the lower plate of doubly thickened crust implying clockwise P-T trajectory (Ellis, 1987; Harley, 1989; 1991). Motoyoshi and Hensen (1989) and Hensen and Motoyoshi (1992) discussed polymetamorphic events with compressional counterclockwise P-T path based on the textural evidence, and proposed a regional scale intrusion of pluton above the present level of exposure for the heat source of second event. Harley (1998) noted that convective thinning or detachment of the lithospheric thermal boundary layer during or after crustal thickening may play a major role in the formation of UHT metamorphism. In the following, the proposed tectonic processes to cause the ultrahigh-temperature metamorphism of the Napier Complex is assessed by thermal modeling using numerical solutions.

7.2.2. Analytical method

One-dimensional explicit finite-difference method (Peacock, 1989) is applied for the thermal modeling. Finite difference form is written as follows:

$$\Delta T/\Delta t = \mathrm{kappa}\cdot\Delta^2 T/\Delta z^2 - v_z\cdot\Delta T/\Delta z + A/\mathrm{rho}\cdot C \qquad \text{eq. 7.1}$$

where T: temperature [K],
t: time [s],
kappa: thermal diffusivity [m^2/s],
z: depth [m],
v_z: velocity of the medium in the z-direction [m/s],
A: volumetric heat production [W/m^3],

rho: density [kg/m^3], and
C: specific heat [J/kg·K].

Calculations were performed using a grid of the solution domain as shown in Fig. 7.3. Size of the time step (Δt) is constrained by size of the depth step (Δz) as follows:

$$\Delta t \leq (\Delta z)^2/2 \cdot kappa$$

T at point **i** is calculated by the following equation expanded from Peacock (1989):

$$T_{n+1,i} = T_{n,i} + [kappa \cdot \Delta^2 T/\Delta t^2 - v_z \cdot \Delta T/\Delta z + A/rho \cdot C] \cdot \Delta t \qquad \text{eq. 7.2}$$

where,

$$\Delta^2 T/\Delta t^2 = (T_{i+1} - 2 \cdot T_i + T_{i-1})/(\Delta z)^2$$

7.2.3. Models and results

Three models were calculated; (1) crustal thickening associated with continental collision, (2) intrusion of magma as sills at mid crust, and (3) delamination of lower crust with lithospheric mantle. Values of the parameters used for calculations are listed in Table 7.1. Homogeneous distribution model of radioactive elements is assumed for simplification, instead of multi-layer model or exponential distribution model (Spear, 1993). The solution domain comprehends 150 km x 50 Ma with Δz = 2 km (total 75 steps) and Δt = 50000 years (total 1000 steps). In the models (2) and (3), no crustal exhumation is assumed (v_z = 0) and the equation 7.2 is written as follows:

$$T_{n+1,i} = T_{n,i} + [kappa \cdot \Delta^2 T/\Delta t^2 + A/rho \cdot C] \cdot \Delta t \qquad \text{eq. 7.3}$$

Models of crustal thickening, intrusion of magma and underplating of asthenospheric mantle are computed using above method.

(a) Steady state geotherm (Fig. 7.5a)

Steady state geotherms at present and at 2.5 Ga are calculated using the following equations described in Spear (1993).

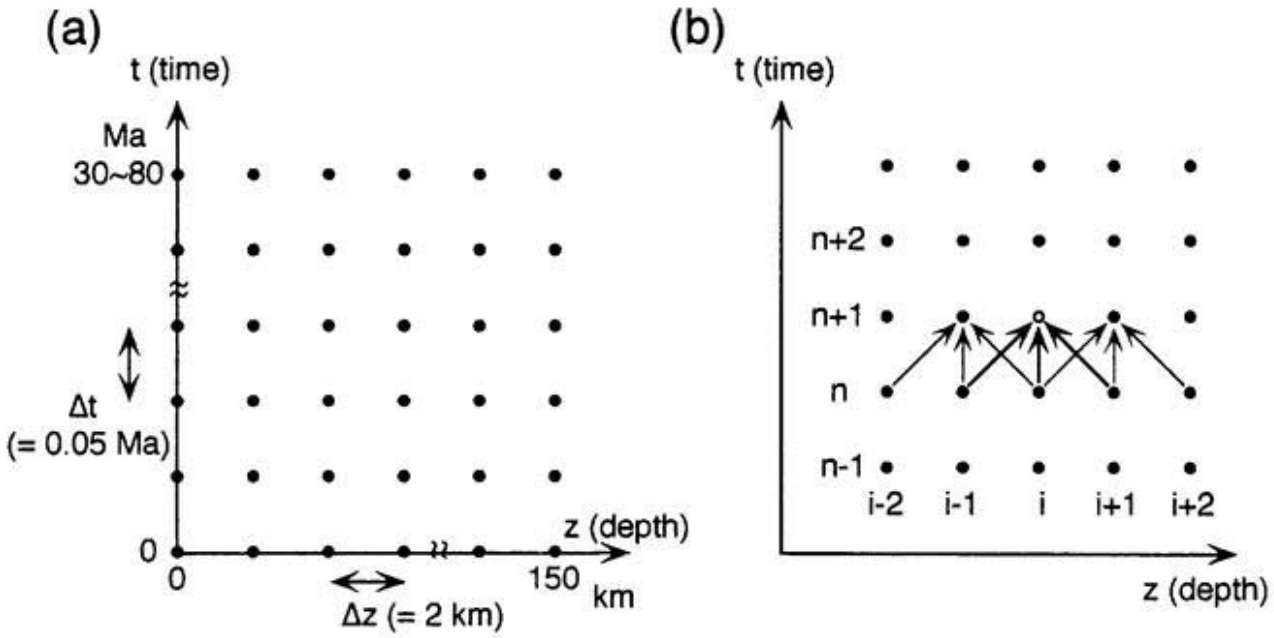

Fig. 7.3 Graphical representation of the grid points used to calculate temperatures as described in Peacock (1989). (a) Graphical representation of the finite difference grid points covering the solution domain. (b) Explicit finite difference method. The temperature for grid point i at the next time level ($T_{n+1,i}$) depends explicitly on temperatures at current time level: $T_{n,i-1}$, $T_{n,i}$, $T_{n,i+1}$.

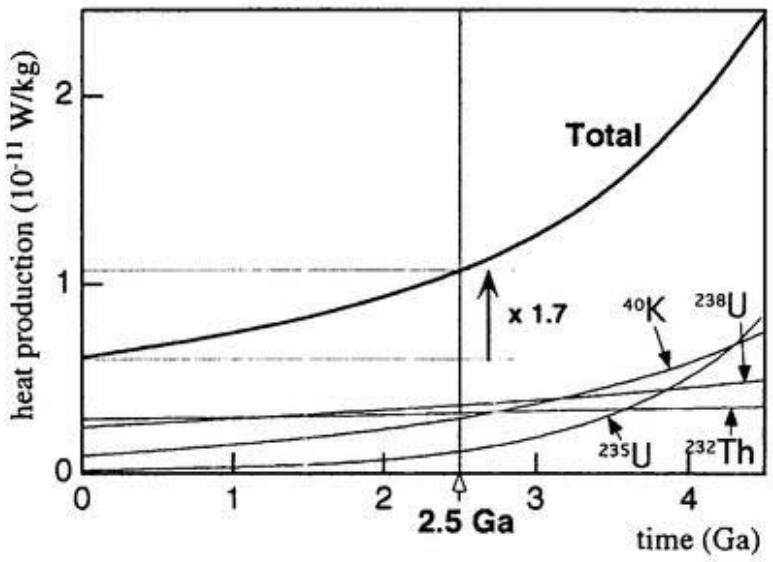

Fig. 7.4 (a) Mean mantle heat production rates due to the decay of the radioactive isotopes as functions of time measured back from the present (Turcotte and Schubert, 1982).

Symbol	Name		Values used for the calculation		typical values in the crust	note
	general					
k	thermal conductivity		2.25	W/m/°C	1.5-3.0	
ρ (rho)	density		2.7	g/cm^3	2.7-3.0	
c	specific heat		1000	J/kg/°C	1000	
A	heat production	present value	0.75	μW/m^3	0.5-1.0	
		value at 2.5 Ga	1.28	μW/m^3		
Q*	mantle heat flux		30	mW/m^2	20-40	
κ (kappa)	thermal diffusivity		(0.83)	mm^2/s	0.6-1.2	= k/ρ/c
D	crust thickness		35	km		
Δt	time interval		0.05	m.y.		(< Δz^2/κ/2)
Δz	position interval		2	km		
	crustal thickening accompanied by continental collision					
	initial crust thickness		70	km		
	time interval before uplift		20	m.y.		
	uplift rate (Vz)		1	mm/y.	0.1-10	
	intrusion of magma into the mid crust					
	crust thickness (including sills)		40	km		
	thickness of sills		6	km		21~27 km depth
	temperature of sills		1500	°C		
	ΔH of crystallization		400	kJ/kg		
	ΔT of crystallization		100	°C		
	removal of lithospheric thermal boundary layer					
	initial crust thickness		40	km		
	thickness of delamination		50	km		35~85 km depth

Table 7.1 Values of the parameters used for the calculations. Typical values for the crust are after Spear (1993). Heat production (from radioactive decay) at 2.5 Ga is estimated from Turcotte and Schubert (1982).

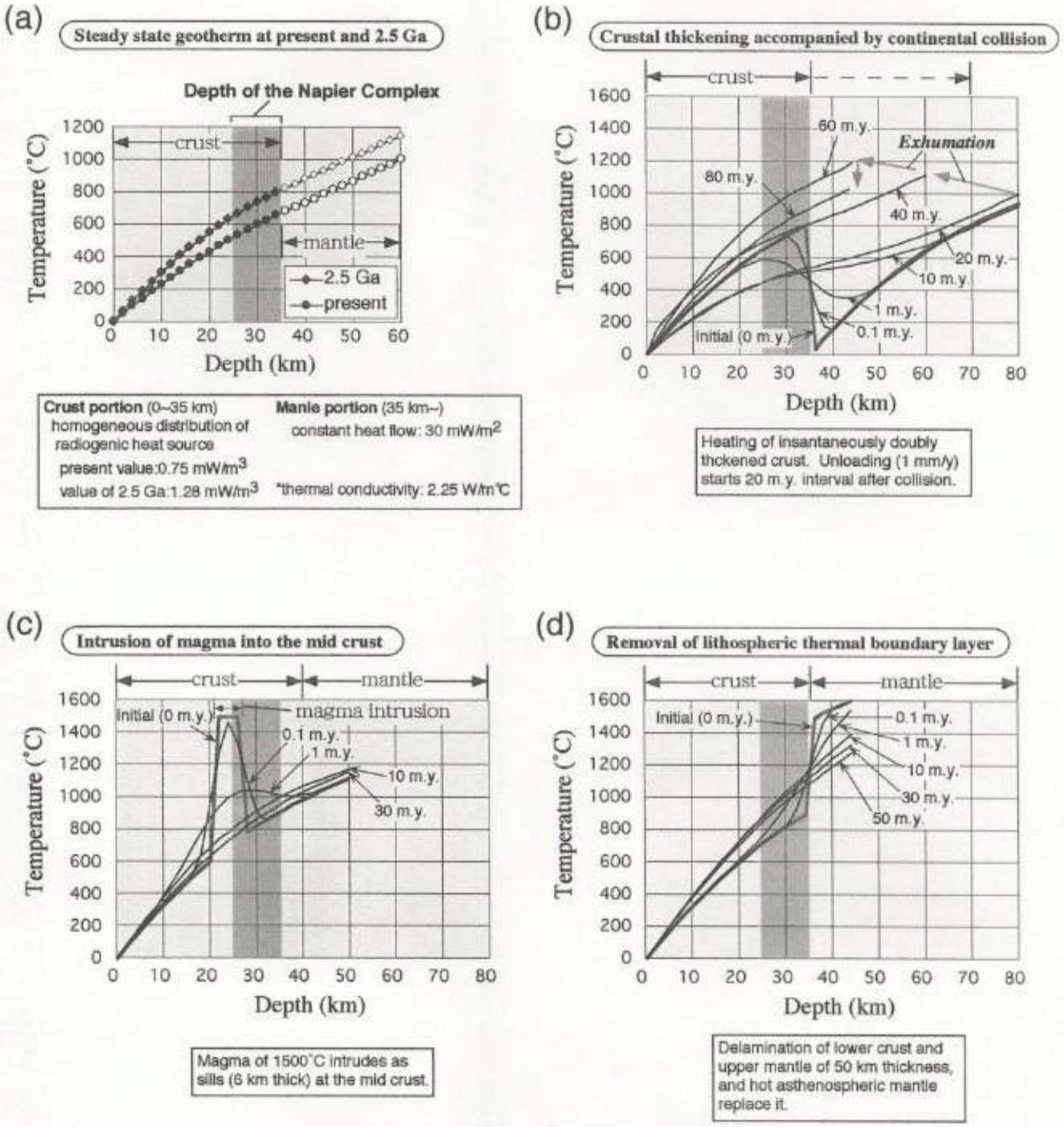

Fig. 7.5 Results of the thermal modeling calculation using the finitie-difference method described in Peacock (1989). See detail in the text. (a) Steady state geotherm calculated for present and 2.5 Ga, using the equation 7.4 for crust and the equation 7.5 for mantle. (b) Thermal evolution of the crustal thickening model. Curves labeled with time in millions of years after instantaneous thickening, (c) Thermal evolution of the magma intrusion model. Curves labeled with time in millions of years after instantaneous intrusion of magma (1500°C) as sills of 6 km thick at 21~27 km depth in the crust. (d) Thermal evolution of the delamination model. Curves labeled with time in millions of years after instantaneous removal of 50 km thick layers including lower crust and upper mantle from 35 km to 85 km depth.

$$T = -A \cdot z^2 / 2k + (Q^* / k + A \cdot D / k) z \qquad 0 \le z \le D \qquad \text{eq. 7.4}$$

and

$$T = A \cdot D^2 / 2k + Q^* \cdot z / k \qquad z > D \qquad \text{eq. 7.5}$$

Crust thickness (D) of 35 km is applied for the calculation. Homogeneous distribution of radiogenic heat production elements in the crust is assumed for simplifications. Heat production rates due to the decay of the radioactive isotopes in the crust at 2.5 Ga are inferred from those in mantle calculated as a function of time before the present (Turcotte and Schubert, 1982; and see Fig. 7.4). The result suggests that the steady state geotherm at 2.5 Ga is about 150°C (at the bottom of the crust) higher temperature than that of the present.

(b) Crustal thickening accompanied by continental collision (Fig. 7.5b)

England and Thompson (1984) and Peacock (1989) have calculated this model using homogeneous distribution and exponential distribution of radioactive elements, respectively. They essentially obtained quite similar results.

This study reassessed the model that instantaneous thickening of two 35 km thick continental crusts along a single thrust. The results is shown in Fig. 7.5b.

The maximum temperatures of about 1050°C at the bottom of the crust are attained at 60 m.y. This suggest that it is difficult to heat the mid to lower crust of 25 ~ 35 km depth 1100°C solely by this process.

(c) Intrusion of magma (Fig. 7.5c)

Intrusion of magma (high temperature and relatively dry anorthosite magma is supposed) into mid crust as sills is modeled. Latent heat of magma crystallization is used that of basaltic magma.

High magma temperature, >1500°C, and quite thick sills layer, >6km, is required to heat the lower crust of 25 ~ 35 km depth >1000°C. In this model, 1100°C is attained only near the sills less than 2 km, and persists short period of less than 0.1 m.y.

(d) Underplating of asthenospheric mantle (Fig. 7.5d)

Another possible process to heat mid to lower crust extremely high temperature condition is the removal (delamination) of lithospheric thermal boundary layer including both lower crust and lithosperic mantle, which is

proposed for common process below the continental crust, especially for thickened crust. Hot asthenospheric mantle replacing relatively cold lower crust and lithospheric mantle could heat the crust.

Underplating of >1500°C asthenospheric mantle, which results from the delamination of 50 km thick (lower crust and lithospheric mantle) could heat the mid to lower crust of 25 ~ 35 km depth 1000~1100°C, depending on the thickness of the removed layer and temperature of asthenospheric mantle.

In summary, the process associated with the removal of lithospheric thermal boundary layer and the heating directly from hot asthenospheric mantle is one of the possible candidate for the heat source of the UHT metamorphism, especially for the regional 1100°C conditions.

Mid to lower crust generally contain a certain amount of hydrous minerals, such as biotite and amphibole, and, hence, the heating promotes dehydration melting of hydrous mineral. If enough quantity of heat is supplied, crustal material should generate quartzo-feldspathic magma and relatively mafic restite. If the heat is not enough, latent heat of melting compensates and prevents the increasing of temperature further above, and the rocks recrystallized at general granulite facies of 700 ~ 800°C, where partial melt and restitic rock could coexist. If already dehydrated dry crust is re-heated, partial melting does not occur and temperature could rise to the UHT conditions. Therefore, not only heat source, but also dehydration process prior to the heating to UHT conditions is considered to be the essential factor for the UHT metamorphism.

7.3. Timing of the ultrahigh-temperature metamorphism

Harley and Black (1997) summarized the geochronology of the Napier Complex that the initial felsic igneous activity started at 3.8 Ga and that the ultrahigh-temperature metamorphism occurred at 2.8 Ga. 3.0 Ga and 2.5 Ga obtained from several dating were interpreted by them to be the local heating accompanied by the intrusion of felsic magma and the retrograde recrystallization perhaps promoted by fluid ingress, respectively.

2.5 Ga is widespreadly obtained from the Napier Complex by several radiometric datings (Grew and Manton, 1979; De Paolo *et al.*, 1982; Owada *et al.*, 1994; Tainosho *et al.*, 1994; Shiraishi *et al.*, 1997; Asami *et al.*, 1998). Sheraton *et al.* (1987) and Harley and Black (1997) interpreted that 2.5 Ga as the age of relatively lower grade granulite ~ amphibolite metamorphism than the UHT

metamorphism of ~2.8 Ga. In chapter 6, age determinations of monazite and zircon from UHT gneisses without any evidence of retrograde recrystallization represent 2.5 Ga. This implies 2.5 Ga as the UHT stage. As discussed above, dehydration process is needed before UHT metamorphism. Therefore, 2.8 Ga event may be igneous activity to form protolith of the UHT gneisses or dehydration event prior to the UHT metamorphism. And then the UHT metamorphism occurred at 2.5 Ga.

Chapter 8 Conclusions

1. Mineral parageneses involving sapphirine, orthopyroxene, garnet, sillimanite, cordierite, osumilite and quartz, and reaction textures after sapphirine + quartz in the quartzo-feldspathic, siliceous and aluminous gneisses from the Mt. Riiser-Larsen area are investigated with respect to the phase equilibrium. Based on the recent progress of experimentally determined phase relations, >1040°C and 0.6~0.8 GPa are estimated for equilibrium P-T conditions of the central area of the Mt. Riiser-Larsen, and >1030°C and 0.8~0.9 GPa for those of the western area. These two areas are divided by the 200 m wide shear zone of mylonite and pseudotachylite representing vertical foliation and sub-vertical lineation. These suggest that the gneisses of two different structural levels have juxtaposed due to the movement along the shear zone after isobaric cooling. The higher-pressure in western area than the central one is oblique to the proposed regional field baric gradient within the Napier Complex of pressure increasing southward, but is consistent with the proposed uplift process of the Napier Complex in relation with the tectonic event of the Rayner Complex at 1.0 Ga.

2. Equilibrium temperatures of >1100°C for the thermal peak are obtained by the re-integration of the mineral compositions of perthite, mesoperthite and antiperthite in gneisses with various chemical compositions, i.e., orthopyroxenefelsic gneiss, garnet felsic gneiss, garnet-sillimanite gneiss, garnet-orthopyroxene-bearing quartzo-feldspathic or siliceous gneisses, sapphirine-bearing aluminous gneisses from the Mt. Riiser-Larsen area and sapphirine-bearing aluminous gneisses from Tonagh Island in the Napier Complex. The areal extent of 1100°C should be at least 50 x 10 km, involving Mt. Riiser-Larsen and Tonagh Island, and maximum 200 x 50 km which is the areal distribution of sapphirine+quartz in the Napier Complex.

3. Garnet-orthopyroxene geobarometry yields the pressure condition of 0.8~1.1 GPa for the thermal peak (~1100°C) of the northern area of Tonagh Island. This implies that the present exposed level of Tonagh Island is similar or possibly deeper structural level than that of the Mt. Riiser-Larsen area. This is consistent with the proposed regional field baric gradient within the complex.

4. The age of the UHT metamorphism of the Napier Complex, either of 2.8-2.9 Ga or 2.5 Ga in dispute, is investigated by the precise quantitative estimations of U, Th and Pb contents of monazite and zircon in situ from the gneisses containing sapphirine+quartz, osumilite or alkali feldspar which indicate UHT conditions in the Mt. Riiser-Larsen area, using electron microprobe with WDS. Most of analyzed grains represent 2.5 Ga or younger ages, except three zircon grains representing 2.7~2.9 Ga from sapphirine-orthopyroxene-plagioclase-quartz gneiss. 2.3~2.5 Ga are obtained from monazite and zircon grains enclosed within osumilite. Based on these age determination and textural observation, it is suggested that the UHT metamorphism occurred at 2.5 Ga. 2.8-2.9 Ga obtained by several datings should be the age of the formation of protolith or that of the preceding high-temperature metamorphism which may promote the dehydration of the Napier Complex prior to the UHT metamorphism.

5. Heat source of the UHT metamorphism of the Napier Complex is preliminary investigated by the thermal modeling using numerical solution with finite deferent method. As the results, the UHT conditions cannot be achieved solely by usual crustal thickening process. The intrusion of high temperature magma (anorthosite ?) above the present exposed structural level of the complex or underplating of hot asthenospheric mantle accompanied by the removal (delamination) of the lower crust and upper mantle (lithospheric thermal boundary layer) could be the heat source of the UHT metamorphism. In addition, it is considered that not only heat source, but also dehydration process prior to the heating to UHT conditions is the essential factor for the UHT metamorphism.

Acknowledgments

This thesis has been carried out at the National Institute of Polar Research (Department of Polar Science, The Graduate University for Advanced Studies) under the supervision of Prof. Kazuyuki Shiraishi and Dr. Yoichi Motoyoshi. They are much appreciated for discussion, support and encouragement throughout this study.

Geological survey in Antarctica was a project of 38th and 39th Japanese Antarctic Research Expeditions (JARE) led by K. Yamanouchi and H. Yamagishi (JARE-38) and by K. Shibuya and K. Moriwaki (JARE-39), respectively. I am grateful to the members of JARE and the crew of the icebreaker SHIRASE for their support during the 1996-1997 and the 1997-1998 field seasons, and to NIPR for enabling me to participate in JARE. Collaborating field work with Prof. H. Ishizuka, Dr. M. Ishikawa and Ms. S. Suzuki in the Mt. Riiser-Larsen and with Drs. Y. Osanai, T. Toyoshima, M. Owada, T. Tsunogae and Mr. W.A. Crowe in Tonagh Island are much valuable and good experience for me, and I appreciate them very much. Drs. H. Miura, M. Takada and D.P. Zwartz, JARE geomorphologists, are also thanked for their co-operation in the Mt. Riiser-Larsen.

Prof. Y. Hiroi and Dr. Y. Osanai gave many valuable comments on this thesis. Valuable discussion with Prof. M. Arima, Prof. H. Ishizuka and Dr. M. Ishikawa also contributed to this study. Comments made by Prof. B.J. Hensen and Prof. S.L. Harley during the Symposium on Antarctic Geosciences, held at NIPR in 1997, were also much valuable. Comments were also made by Prof. K. Shibuya and Prof. K. Moriwaki. Daily discussion with K. Shiraishi, Y. Motoyoshi and S. Suzuki has been undoubtedly most important motive force of the thesis. I acknowledge them very much.

Laboratory work has been conducted at NIPR, and are supported by staffs and students in the institute. Dr. K. Yokoyama of National Science Museum kindly helped and instructed me on microprobe analyses of monazite and zircon and prepared us standard samples for U and Th. Some of thin sections used in this study were made by Mr. S. Ohno. Thanks are also due to them.

S. Banno, Emeritus Professor of Kyoto University, and Dr. T. Hirajima, who were supervisors of my Master's thesis at Kyoto University, were appreciated to recommend me to study at NIPR.

References

Asami, M., Suzuki, K., Grew, E. S. and Adachi, M., 1998. CHIME ages for granulites from the Napier Complex, East Antarctica. *Polar Geoscience*, **11**, 172-199.

Audibert, N., Hensen, B. J. and Bertrand, P., 1995. Experimental study of phase relations involving osumilite in the system K_2O-FeO-MgO-Al_2O_3-SiO_2-H_2O at high pressure and temperature. *Journal of Metamorphic Geology*, **13**, 331-344.

Baba, S., 1998. Ultra-high temperature metamorphism in the Lewisian Complex, South Harris, Scotland. *Memoirs of National Institute of Polar Research Special Issue*, **53**, 93-108.

Bertrand, P., Ellis, D. J. and Green, D. H., 1991. The stability of sapphirine-quartz and hypersthene-sillimanite-quartz assemblages: an experimental investigation in the system FeO-MgO-Al_2O_3-SiO_2 under H_2O and CO_2 conditions. *Contributions to Mineralogy and Petrology*, **108**, 55-71.

Black, L. P., Williams, I. S. and Compston, W., 1986. Four zircon ages from one rock: the history of a 3930 Ma-old granulite from Mount Sones, Antarctica. *Contributions to Mineralogy and Petrology*, **94**, 427-437.

Carrington, D. P. and Harley, S. L., 1995a. Partial melting and phase relations in high-grade metapelites: an experimental petrogenetic grid in the KFMASH system. *Contributions to Mineralogy and Petrology*, **120**, 270-291.

Carrington, D. P. and Harley, S. L., 1995b. The stability of osumilite in metapelitic granulites. *Journal of Metamorphic Geology*, **13**, 613-625.

Coleman, R. G. and Wang, X., 1995. Overview of the geology and tectonics of UHPM. In: *Ultrahigh pressure metamorphism* (eds Coleman, R. G. and Wang, X.), pp. 1-32, Cambridge University Press, Cambridge.

Dallwitz, W. B., 1968. Coexisting sapphirine and quartz in granulites from Enderby Land, Antarctica. *Nature*, **219**, 476-477.

De Paolo, D. J., Manton, W. I., Grew, E. S. and Halpern, M., 1982. Sm-Nd, Rb-Sr and U-Th-Pb systematics of granulite facies rocks from Fyfe Hills, Enderby Land, Antarctica. *Nature*, **298**, 614-618.

Ebadi, A. and Johannes, W., 1991. Beginning of melting and composition of first melts in the system Qz-Ab-Or-H_2O-CO_2. *Contributions to Mineralogy and Petrology*, **106**(286-295).

Elkins, L. T. and Grove, T. L., 1990. Ternary feldspar experiments and thermodynamic models. *American Mineralogist*, **75**, 544-559.

Ellis, D. J., 1987. Origin and evolution of granulites in normal and thickened crusts. *Geology*, **15**, 167-170.

Ellis, D. J. and Green, D. H., 1985. Garnet-forming reactions in mafic granulites from Enderby Land, Antarctica - implications for geothermometry and geobarometry. *Journal of Petrology*, **26**, 633-662.

Ellis, D. J., Sheraton, J. W., England, R. N. and Dallwitz, W. B., 1980. Osumilite-sapphirine-quartz granulites from Enderby Land, Antarctica: mineral assemblages and reactions. *Contributions to Mineralogy and Petrology*, **72**, 123-143.

England, P. C. and Thompson, A. B., 1984. Pressure-temperature-time paths of regional metamorphism I. Heat transfer during the evolution of regions of thickened continental crust. *Journal of Petrology*, **25**, 894-928.

Fitzsimons, I. C. W. and Harley, S. L., 1994. The influence of retrograde cation exchange on granulite P-T estimates and a convergence technique for the recovery of peak metamorphic conditions. *Journal of Petrology*, **35**, 543-576.

Furhman, M. L. and Lindsley, D. H., 1988. Ternary-feldspar modeling and thermometry. *American Mineralogist*, **73**, 201-215.

Ghiorso, M. S., 1984. Activity/composition relations in the ternary feldspars. *Contributions to Mineralogy and Metrology*, **87**, 282-296.

Grew, E. S., 1980. Sapphirine + quartz association from Archaean rocks in Enderby Land, Antarctica. *American Mineralogist*, **65**, 821-836.

Grew, E. S., 1982. Osumilite in the sapphirine-quartz terrane of Enderby Land, Antarctica: implications for osumilite petrogenesis in the granulite facies. *American Mineralogist*, **67**, 762-787.

Grew, E. S. and Manton, W. I., 1979. Archean rocks in Antarctica: 2.5 billion-year uranium-lead ages of pegmatites in Enderby Land. *Science*, **206**, 443-445.

Harley, S. L., 1983. Regional geobarometry-geothermometry and metamorphic evolution of Enderby Land, Antarctica. In: *Antarctic Earth Science* (eds Oliver, R. L., James, P. R. and Jago, J. B.), pp. 25-30, Australian Academy of Science, Canberra.

Harley, S. L., 1984a. An experimental study of the partitioning of Fe and Mg between garnet and orthopyroxene. *Contributions to Mineralogy and Petrology*, **86**, 359-373.

Harley, S. L., 1984b. The solubility of alumina in orthopyroxene coexisting with garnet in FeO-MgO-Al_2O_3-SiO_2 and CaO-FeO-MgO-Al_2O_3-SiO_2. *Journal of Petrology*, **25**, 665-696.

Harley, S. L., 1985. Garnet-orthopyroxene bearing granulites from Enderby Land, Antarctica: metamorphic pressure-temperature-time evolution of the Archaean Napier Complex. *Journal of Petrology*, **26**, 819-856.

Harley, S. L., 1986. A sapphirine-cordierite-garnet-sillimanite granulite from Enderby Land, Antarctica: implications for FMAS petrogenetic grids in the granulite facies. *Contributions to Mineralogy and Petrology*, **94**(452-460).

Harley, S. L., 1987. A pyroxene-bearing metaironstone and other pyroxene-granulites from Tonagh Island, Enderby Land, Antarctica: further evidence for very high temperature (> 980°C) Archaean regional metamorphism in the Napier Complex. *Journal of Metamorphic Geology*, **5**, 341-356.

Harley, S. L., 1989. The origins of granulites: a metamorphic perspective. *Geological Magazine*, **126**, 215-247.

Harley, S. L., 1991. The crustal evolution of some East Antarctic granulites. In: *Geological Evolution of Antarctica* (eds Thomson, M. R. A., Crame, J. A. and Thomson, J. W.), pp. 7-12, Cambridge University Press, Cambridge.

Harley, S. L., 1998. On the occurrence and characterisation of ultrahigh-temperature crustal metamorphism. In: *What Drives Metamorphism and Metamorphic Reactions?* (eds Treloar, P. J. and O'Brien, P.), pp. 75-101.

Harley, S. L. and Black, L. P., 1997. A revised Archaean chronology for the Napier Complex, Enderby Land, from SHRIMP ion-microprobe studies. *Antarctic Science*, **9**, 74-91.

Harley, S. L. and Hensen, B. J., 1990. Archaean and Proterozoic high-grade terranes of East Antarctica (40-80°E): a case study of diversity in granulite facies metamorphism. In: *High-temperature Metamorphism and Crustal Anatexis* (eds Ashworth, J. R. and Brown, M.), pp. 320-370, Unwin Hyman, London.

Harley, S. L. and Motoyoshi, Y., 1997. Evidence for 1120°C UHT metamorphism in the Napier Complex. *Abstract of 17th NIPR symposium on Antarctic geosciences*, 74.

Hensen, B. J., 1971. Theoretical phase relations involving cordierite and garnet in the system MgO-FeO-Al_2O_3-SiO_2. *Contributions to Mineralogy and Petrology*, **33**, 191-214.

Hensen, B. J., 1986. Theoretical phase relations involving cordierite and garnet revisited: the influence of oxygen fugacity on the stability of sapphirine and spinel in the system Mg-Fe-Al-Si-O. *Contributions to Mineralogy and Petrology*, **92**, 362-367.

Hensen, B. J., 1987. P-T grids for silica-undersaturated granulites in the system MAS (n+4) and FMAS (n+3) - tools for the derivation of P-T paths of metamorphism. *Journal of Metamorphic Geology*, **5**, 255-271.

Hensen, B. J. and Green, D. H., 1971. Experimental study of the stability of cordierite and garnet in pelitic compositions at high pressures and temperatures. I. Compositions with excess alumino-silicate. *Contributions to Mineralogy and Petrology*, **33**, 309-330.

Hensen, B. J. and Green, D. H., 1972. Experimental study of the stability of cordierite and garnet in pelitic compositions at high pressures and temperatures. II. Compositions without excess alumino-silicate. *Contributions to Mineralogy and Petrology*, **35**, 331-354.

Hensen, B. J. and Green, D. H., 1973. Experimental study of the stability of cordierite and garnet in pelitic compositions at high pressures and temperatures. III. Synthesis of experimental data and geological applications. *Contributions to Mineralogy and Petrology*, **38**, 151-166.

Hensen, B. J. and Motoyoshi, Y., 1992. Osumilite-producing reactions in high-temperature granulites from the Napier Complex, East Antarctica: tectonic implications. In: *Recent Progress in Antarctic Earth Science* (eds Yoshida, Y., Kaminuma, K. and Shiraishi, K.), pp. 87-92, Terrapub, Tokyo.

Holland, T. J. B., Babu, E. V. S. S. K. and Waters, D. J., 1996. Phase relations of osumilite and dehydration melting in pelitic rocks: a simple thermodynamic model for the KFMASH system. *Contributions to Mineralogy and Petrology*, **124**, 383-394.

Holtz, F. and Johannes, W., 1994. Maximum and minimum water contents of granitic melts: implications for chemical and physical properties of ascending magmas. *Lithos*, **32**, 149-159.

Hovis, G. L., Delbove, F. and Bose, M. R., 1991. Gibbs energies and entropies of K-Na mixing for alkali feldspars from phase equilibrium data: implications for feldspar solvi and short-range order. *American Mineralogist*, **76**, 913-927.

Ishizuka, H., Ishikawa, M., Hokada, T. and Suzuki, S., 1998. Geology of the Mt. Riiser-Larsen area of the Napier Complex, Enderby Land, East Antarctica. *Polar Geoscience*, **11**, 154-171.

Kretz, R., 1983. Symbols for rock-forming minerals. *American Mineralogist*, **68**, 277-279.

Kroll, H., Evangelakakis, C. and Voll, G., 1993. Two-feldspar geothermometry: a review and revision for slowly cooled rocks. *Contributions to Mineralogy and Petrology*, **114**, 510-518.

Lindsley, D. H. and Nekvasil, H., 1989. A ternary feldspar model for all reasons. *EOS*, **70**, 506.

Makimoto, H., Asami, M. and Grew, E. S., 1989. Some geological observations on the Archean Napier Complex at Mt. Riiser-Larsen, Amundsen Bay, Enderby Land. *Proceedings of the NIPR Symposium on Antarctic Geosciences*, **3**, 128-141.

Motoyoshi, Y. and Hensen, B. J., 1989. Sapphirine-quartz-orthopyroxene symplectites after cordierite in the Archaean Napier Complex, Antarctica: evidence for a counterclockwise P-T path? *European Journal of Mineralogy*, **1**, 467-471.

Motoyoshi, Y., Hensen, B. J. and Arima, M., 1993. Experimental study of the high-pressure stability limit of osumilite in the system K_2O-MgO-Al_2O_3-SiO_2: implications for high-temperature granulites. *European Journal of Mineralogy*, **5**, 439-445.

Motoyoshi, Y., Hensen, B. J. and Matsueda, H., 1990. Metastable growth of corundum adjacent to quartz in a spinel-bearing quartzite from the Archaean Napier Complex, Antarctica. *Journal of Metamorphic Geology*, **8**, 125-130.

Motoyoshi, Y. and Matsueda, H., 1984. Archean granulites from Mt. Riiser-Larsen in Enderby Land, East Antarctica. *Memoirs of the National Institute of Polar Research, Special Issue*, **33**, 103-125.

Newton, R. C., 1990. Fluids and melting in the Archaean deep crust of southern India. In: *High-temperature metamorphism and crustal anatexis* (eds Ashworth, J. R. and Brown, M.), pp. 149-179, Unwin Hyman, London.

Osanai, Y., Toyoshima, T., Owada, M., Tsunogae, T., Hokada, T. and Crowe, W. A., 1999. Geology of ultrahigh-temperature metamorphic rocks from the Tonagh Island in the Napier Complex, Enderby Land, East Antarctica. *Polar Geoscience*, **12**, 1-28.

Owada, M., Osanai, Y. and Kagami, H., 1994. Isotopic equilibration age of Sm-Nd whole-rock system in the Napier Complex (Tonagh Island), East Antarctica. *Proceedings of the NIPR Symposium on Antarctic Geosciences*, **7**, 122-132.

Peacock, S. M., 1989. Thermal modeling of metamorphic pressure-temperature-time paths: a forward approach. In: *Metamorphic pressure-temperature-time paths. Short course in geology.* (eds Spear, F. S. and Peacock, S. M.), pp. 57-102, American Geophysical Union, Washington, D.C.

Raase, P., 1998. Feldspar thermometry: a valuable tool for deciphering the thermal history of granulite-facies rocks, as illustrated with metapelites from Sri Lanka. *The Canadian Minearlogist*, **36**, 67-86.

Ravich, M. G. and Kamenev, E. N., 1975. *Crystalline Basement of the Antarctic Platform*. John Wiley, New York.

Sandiford, M., 1985. The metamorphic evolution of granulites at Fyfe Hills: implications for Archaean crustal thickness in Enderby Land, Antarctica. *Journal of Metamorphic Geology*, **3**, 155-178.

Sandiford, M. and Powell, R., 1986. Pyroxene exsolution in granulites from Fyfe Hills, Enderby Land, Antarctica: evidence for 1000°C metamorphic temperatures in Archaean continental crust. *American Mineralogist*, **71**, 946-954.

Sandiford, M. and Powell, R., 1988. Pyroxene exsolution in granulites from Fyfe Hills, Enderby Land, Antarctica: evidence for 1000°C metamorphic temperatures in Archaean continental crust - Reply. *American Mineralogist*, **73**, 434-438.

Sandiford, M. and Wilson, C. J. L., 1986. The origin of Archaean gneisses in the Fyfe Hills region, Enderby Land; field occurrence, petrography and geochemistry. *Precambrian Research*, **31**, 37-68.

Seck, H. A., 1971. Der einfluß des drucks auf die zusammensetzung koexistierender alkalifeldspäte und plagioklase im system $NaAlSi_3O_8$-$KAlSi_3O_8$-$CaAl_2Si_2O_8$-H_2O. *Contributions to Mineralogy and Petrology*, **31**, 67-86.

Sheraton, J. W., Offe, L. A., Tingey, R. J. and Ellis, D. J., 1980. Enderby Land, Antarctica - an unusual Precambrian high-grade metamorphic terrain. *Journal of the Geological Society of Australia*, **27**, 1-18.

Sheraton, J. W., Tingey, R. J., Black, L. P., Offe, L. A. and Ellis, D. J., 1987. *Geology of Enderby Land and western Kemp Land, Antarctica*. Australian Government Publishing Service, Canberra.

Shiraishi, K., Ellis, D. J., Fanning, C. M., Hiroi, Y. and Motoyoshi, Y., 1997. Re-examination of the metamorphic and protolith ages of the Rayner Complex, Antarctica: evidence for the Cambrian (Pan-African) regional metamorphic event. In: *The Antarctic Region: Geological evolution and processes* (ed C.A.Ricci), pp. 79-88, Terra Antarctica Publication, Siena.

Shiraishi, K., Ellis, D. J., Hiroi, Y., Fanning, C. M., Motoyoshi, Y. and Nakai, Y., 1994. Cambrian orogenic belt in East Antarctica and Sri Lanka: implications for Gondwana assembly. *Journal of Geology*, **102**, 47-65.

Spear, F., 1993. *Metamorphic Phase Equilibria and Pressure-Temperature-Time paths*. Mineralogical Society of America, Washington, D.C.

Steiger, R. H. and Jäger, E., 1977. Subcommission on geochronology: convention on the use of decay constants in geo- and cosmochronology. *Earth and Planetary Science Letters*, **36**, 359-362.

Suzuki, K., Adachi, M. and Tanaka, T., 1991. Middle Precambrian provenance of Jurassic sandstone in the Mino Terrane, central Japan: Th-U-total Pb evidence from an electron microprobe monazite study. *Sedimentary Geology*, **75**, 141-147.

Tainosho, Y., Kagami, H., Hamamoto, T. and Takahashi, Y., 1997. Preliminary result for the Nd and Sr isotope characteristics of the Archaean gneisses from Mount Pardoe, Napier Complex, East Antarctica. In: *Proceedings of the NIPR Symposium on Antarctic Geosciences*, pp. 92-101, National Institute of Polar Research, Tokyo.

Tainosho, Y., Kagami, H., Takahashi, Y., Iizumi, S., Osanai, Y. and Tsuchiya, N., 1994. Preliminary result for the Sm-Nd whole-rock age of the metamorphic rocks from Mount Pardoe in the Napier Complex, East Antarctica. In: *Proceedings of the NIPR Symposium on Antarctic Geosciences*, pp. 115-121, National Institute of Polar Research, Tokyo.

Takigami, Y., Ishikawa, N. and Funaki, M., 1998. Preliminary ^{40}Ar-^{39}Ar analyses of igneous and metamorphic rocks from the Napier Complex. *Polar Geoscience*, **11**, 200-207.

Turcotte, D. L. and Schubert, G., 1982. *Geodynamics applications of continuum physics to geological problems*. Wiley & Sons, New York.

Whitney, J. A., 1975. The effects of pressure, temperature, and X_{H_2O} on phase assemblage in four synthetic rock compositions. *Journal of Geology*, **83**, 1-31.

Yokoyama, K. and Saito, Y., 1996. Petrological study of pre-Tertiary sandstones in the South Kitakami Massif, Northeast Japan. *Memoirs of National Science Museum*, **29**, 9-24.